



**ENHANCING GROUND BASED TELESCOPE
PERFORMANCE WITH IMAGE PROCESSING**

DISSERTATION

John C. Zingarelli, Major, USAF

AFIT-ENG-DS-13-D-04

**DEPARTMENT OF THE AIR FORCE
AIR UNIVERSITY**

AIR FORCE INSTITUTE OF TECHNOLOGY

Wright-Patterson Air Force Base, Ohio

DISTRIBUTION STATEMENT A:
APPROVED FOR PUBLIC RELEASE; DISTRIBUTION UNLIMITED

The views expressed in this dissertation are those of the author and do not reflect the official policy or position of the United States Air Force, Department of Defense, or the U.S. Government. This material is declared as work of the U.S. Government and is not subject to copyright protection in the United States.

AFIT-ENG-DS-13-D-04

**ENHANCING GROUND BASED TELESCOPE PERFORMANCE WITH IMAGE
PROCESSING**

DISSERTATION

Presented to the Faculty

Graduate School of Engineering and Management

Air Force Institute of Technology

Air University

Air Education and Training Command

In Partial Fulfillment of the Requirements for the

Degree of Doctor of Philosophy

John C. Zingarelli, BS, MS

Major, USAF

November 2013

DISTRIBUTION STATEMENT A:
APPROVED FOR PUBLIC RELEASE; DISTRIBUTION UNLIMITED

**ENHANCING GROUND BASED TELESCOPE PERFORMANCE WITH IMAGE
PROCESSING**

John C. Zingarelli, BS, MS
Major, USAF

Approved:



Stephen C. Cain, PhD (Chairman)

19 Nov 2013

Date



Christine M. Schubert-Kabban, PhD (Member)

22 Nov 2013

Date



Lt Col Travis F. Blake, PhD (Member)

18 Nov 13

Date



Richard K. Martin, PhD (Member)

21 Nov 2013

Date

Accepted:



ADEDEJI B. BADIRU, PhD
Dean, Graduate School of Engineering
and Management

7 Dec 2013

Date

Abstract

The Space Surveillance Telescope (SST) is a Defense Advanced Research Projects Agency (DARPA) program designed to detect objects in space like Near Earth Asteroids (NEAs) and space debris in the Geosynchronous Earth Orbit (GEO) belt. Binary hypothesis tests (BHTs) have historically been used to facilitate the detection of new objects in space. In this dissertation, a multi-hypothesis test (MHT) detection strategy is introduced to improve the detection performance of the SST. In this context, the MHT determines if an unresolvable point source is in the center, corner or side of a pixel in contrast to a BHT, which only tests whether an object is in the pixel or not. An experiment, recording observations of a known GEO satellite as it enters eclipse, is used to demonstrate improved probability of detection with the MHT by as much as 50% over existing BHT methods.

In order to achieve optimal performance of the SST, alignment of the telescope is conducted by retrieving phase information from defocused point sources to determine the telescope's aberrations and then the mirrors are moved for optical correction. A new direct search phase retrieval technique for determining the optical prescription of an imaging system in terms of Zernike coefficients is described. The technique provides coefficient estimates without the need to defocus point source images to generate phase diversity by using electric field estimates in addition to intensity data. Simulated point source data shows the new phase retrieval algorithm avoids getting trapped in local minima over a wide range of random aberrations. Experimental point source data are used to demonstrate the phase retrieval effectiveness.

Acknowledgments

This material is based upon work sponsored by DARPA. MIT Lincoln Laboratory inputs were instrumental in problem identification and telescope understanding. In addition, MIT also provided the SST sensor subsystem images, PSF charts and engineering support for the eclipse experiment. However, the most important support I received in this effort was from my family, especially my wife. Her support of my endeavors ensured my success.

J. Chris Zingarelli

Table of Contents

	Page
Abstract	v
Acknowledgments	vi
Table of Contents	vii
List of Figures	x
List of Tables	xi
I. Introduction	1
1.1 Motivation	4
1.2 Accomplished Work	6
II. Background	9
2.1 Telescope Model	11
2.1.1 Zernike Polynomial for Defocus	11
2.1.2 Zernike Polynomials and the Generalized Pupil Function	13
2.1.3 Intensity Model and PSF Estimation	14
2.2 Phase Retrieval from Stellar Images	15
2.2.1 CRLB for Zernike Coefficients	17
2.2.2 Least Squares and Gerchberg-Saxton Phase Retrieval	17
2.2.3 Curvature Sensing	20
2.3 Atmospheric Models	21
2.3.1 Long Exposure Atmosphere	21
2.3.2 Short Exposure Atmosphere	22
2.4 Detectors	23
2.4.1 Point Detection	25
2.4.2 Correlation versus Point Detection	26
2.4.3 Undersampling and Correlation Detection	29
2.5 Conclusions	31
III. Phase Retrieval with a Long Exposure Atmosphere	35
3.1 Telescope Model	38

3.2 Cramer-Rao Lower Bounds (CRLB) for Variance	41
3.3 Parameter Estimation	46
3.4 Phase Retrieval Simulations.....	48
3.5 Laboratory Demonstrationnstration	52
3.6 Joint Estimation of Spherical Error, Defocus, and Atmospheric Seeing	54
3.7 Conclusions	55
IV. Improving Detection using Multi-hypothesis Testing.....	57
4.1 Introduction.....	57
4.2 The SST Experimental Description	60
4.2.1 Experimental Setup and Process Overview.....	60
4.2.2 The SST System	65
4.2.3 The SST Detection Process	65
4.3 Binary Hypothesis Testing (BHT)	66
4.4 The SST PSF Modeling	67
4.5 Data Normalization Using Outlier Rejection Techniques	71
4.6 Multi-hypothesis testing (MHT)	72
4.7 Conclusions	85
V. Phase Retrieval with a Short Exposure Atmosphere	86
5.1 Introduction.....	87
5.1.1 Generalized Pupil Function	88
5.1.2 Intensity Model and PSF Estimation.....	89
5.2 Direct Search LS vs. E-Field based Estimation	91
5.2.1 E-Field versus Intensity Pattern Correlation	92
5.2.2 Least Squares Zernike Coefficient Estimation	95
5.2.3 E-Field Zernike Coefficient Estimation	97
5.2.4 New Phase Retrieval Algorithm.....	99
5.2.5 Phase Retrieval Simulation	100
5.3 Laboratory Demonstrationnstrations.....	104
5.3.1 Defocus.....	105
5.3.2 Astigmatism.....	108

5.4 Conclusions	111
VI. Conclusions.....	113
6.1 Long Exposure Phase Retrieval Improvements	114
6.2 Telescope Detection Improvements	115
6.3 Short Exposure Phase Retrieval Improvements.....	116
6.4 Future Work	117
6.5 Final Observations	118
VII. Appendices	119
A.1 The SST's CCD Noise Statistics.....	119
A.2 The SST's CCD Pixel Independence	122
A.3 Aberration Calculations for a Single Lens	123
Bibliography	126

List of Figures

Figure	Page
1. A NASA produced image depicting the number of satellites and debris tracked	3
2. A 3-D layout and scale picture of the SST.	4
3. The SST detection block diagram.....	9
4. 2-D wavefront phase error parameterized by the Zernike polynomial for defocus.	12
5. Images of Zernike polynomials numbers 2-11	14
6. Gerchberg-Saxton phase retrieval block diagram.....	20
7. Comparison of aliased and unaliased detector performance.....	31
8. The SST's 6 deg wide field-of-view camera and high speed mechanical shutter	36
9. Variations of the SST's Point Spread Function (PSF).....	37
10. Telescope Model.....	39
11. System model transfer function examples	44
12. A plot of the CRLB for the standard deviation of the Zernike coefficient	46
13. Simulated stars.....	49
14. Estimated defocus parameter determined from simulated star data	50
15. The joint parameter estimates from the simulated stars with shot noise.	51
16. The sample standard deviation of the joint parameter estimates	52
17. Phase retrieval demonstration setup and results	53
18. Defocus and spherical error estimation results.	55
19. Eclipse experiment overview.	61
20. Images of stars used for correlator.....	63
21. The SST's phase retrieved PSF on 2012 March 14.	69
22. Correlation between two different irradiance models.....	71
23. Hypotheses.....	73
24. Illustration depicting the overlap in the corners and sides of the pixels	78
25. Comparison of the baseline detector, the correlator, and M-ary test.	82
26. Composite plot of the probability of detecting ANIK-F1	83
27. Comparison of the baseline detector and the M-ary test.....	84
28. Image of the aperture function, $A(u_1)$, on a 128 by 128 grid.....	93
29. The pairwise correlations.....	95
30. Block diagram new electric field based phase retrieval algorithm	100
31. Phase retrieval simulation examples.....	102
32. Difference between the Zernike coefficients	104
33. Focus demonstration setup.....	106
34. Results of defocus demonstration.	108
35. Astigmatism demonstration setup.....	109
36. Astigmatism demonstration results.....	110
37. Q-Q Plot of star data from the SST images versus a Poisson distribution	122
38. Correlation between a star's center pixel and adjacent pixels	123

List of Tables

Table	Page
1. Telescope Model Parameters	38
2. Alternative Hypothesis Sub-pixel Shifts (corresponding to Figure 23).....	76
3. Summary of the Flops required for Each Detector	79
4. Defocus Demonstration Parameters.....	106
5. Astigmatism Demonstration Zernike Coefficient Estimates	111

ENHANCING GROUND BASED TELESCOPE PERFORMANCE WITH IMAGE PROCESSING

I. Introduction

The Department of Defense recently fielded an f/1 Mersenne-Schmidt telescope called the Space Surveillance Telescope (SST), which saw first light on 15 February 2011 [1]. The SST has significantly advanced the United State's ability to maintain space situational awareness (SSA) beyond that provided by the operationally employed Ground-based Electro-Optical Deep Space Surveillance (GEODSS) telescopes [2]. The main advantages of the SST are that it has a 3.5 m primary mirror and a 6 deg wide field-of-view (FOV) [3]. In contrast, the GEODSS f/2.15 Ritchey-Chretien designed telescopes only have a 1 m primary mirror and a 1.68 deg FOV [2]. The larger primary mirror and increased FOV allow the SST to scan a larger portion of the sky in a shorter period of time with improved detection performance over GEODSS.

SSA is a critical military mission and it directly supports the US National Space Policy to "(p)reserve the Space Environment...the United States shall develop, maintain, and use space situational awareness information from commercial, civil, and national security sources to detect, identify, and attribute actions in space that are contrary to responsible use and the long-term sustainability of the space environment [4]." The SST fills an important niche in the nation's space surveillance network by providing timely and accurate updates to the Joint Space Operations Center's (JSpOC's) space catalogue [5, 6, 7]. Through synoptic search of deep space (i.e. GEosynchronous Orbit (GEO) and Highly Elliptical Orbit (HEO)) on a regular basis, the SST can detect and determine the

orbits of previously unknown space objects. These previously unknown space objects are commonly called uncorrelated targets (UCTs). Timely updates of these UCTs to the JSpOC's space catalogue support vital decision making by US Strategic Command's Joint Functional Component Command for Space in support of the US National Space Policy.

Three major threats from space to both our satellite networks and the earth have been identified. These threats include: space debris, micro-satellites, and near earth asteroids (NEAs) [8, 9, 10]. The detection and characterization of these threats can provide the early warning necessary to take any responsive actions. While the SST was designed for the military mission of detecting debris and microsatellites in deep space, it is also being used for the detection of other astronomical objects like NEAs. The SST's NEA detection work is being done in partnerships with the US Naval Observatory (USNO) and the National Air and Space Administration (NASA). However, the US Air Force's primary concern is the protection of critical national space assets in earth orbit from space debris and micro-satellites [11].

Figure 1 illustrates the known objects (both satellites and debris) that are cataloged by NASA and highlights the sheer number of objects currently being tracked. The SSA functions that are critical to avoiding collisions of these objects in space consist of the detection of UCTs, accurately determining their orbits, and maintaining an up-to-date space catalogue. The SST's main roles in SSA are the detection and orbit determination of UCTs in deep space. GEO can be distinguished in Figure 1 as the dense ring of objects near the equatorial plane. In contrast, radar system like the space fence

are better suited for finding objects in Low Earth Orbit (LEO), which is the dense cloud of objects near the earth in Figure 1 [12].

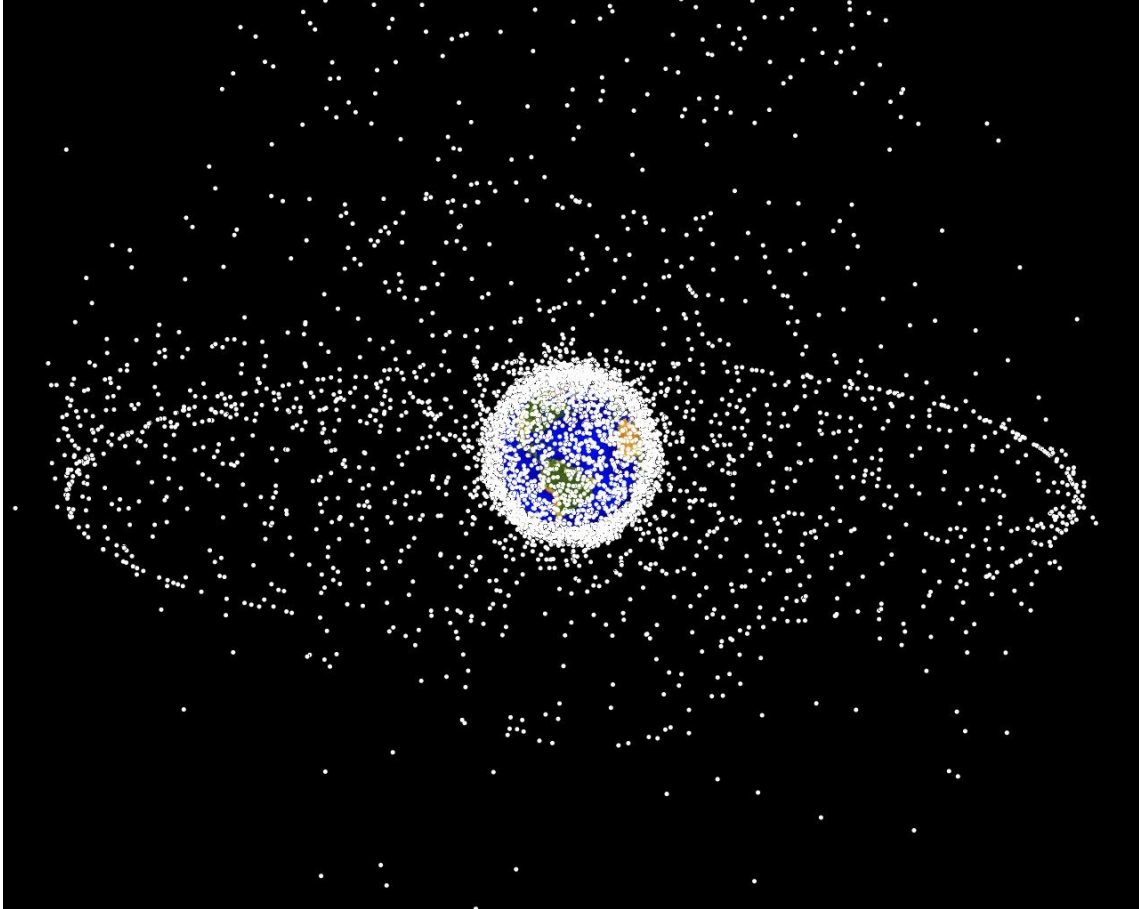


Figure 1. A NASA produced image depicting the number of satellites and debris tracked in earth's orbit. (Note that the objects are not to scale) [12]

A 3-D optical design layout and scale image of SST is shown in Figure 2. The driving design requirements for the telescope differ from more typical astronomical telescopes. The main difference is that SST needs to be able to scan deep space on a regular basis to detect and track UCTs versus maintaining accurate orbits of known objects. In order to accomplish that SSA mission, the Mersenne-Schmidt design was

selected for both its wide FOV and compact design [13]. The size of the primary mirror was driven by the need to detect small faint objects with relatively short integration times to avoid streaking of the satellite image across multiple charged coupled device (CCD) pixels. One drawback to the design is that the optical wavefront is curved in the image plane due to telescope aberrations. To alleviate those optical aberrations, a unique curved detector array was fabricated and implemented in the SST camera [14].

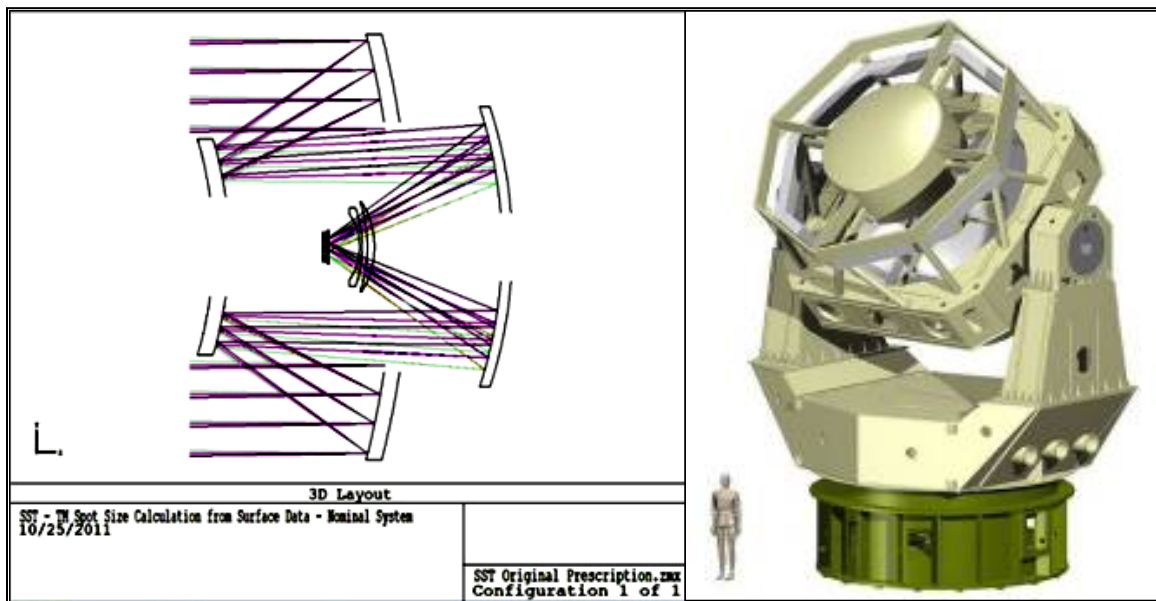


Figure 2. An optical design schematic and scale picture of the SST.

1.1 Motivation

This dissertation investigates how image processing can improve the SST's detection capabilities without requiring physical design changes to the telescope. The two objectives that were introduced in the prospectus for this work have been met and are listed below.

Objective 1. Characterize the SST using a novel aberration estimator

Objective 2. Enhance the SST's performance using detection and estimation theory

The SST was designed and built by Defense Advanced Research Projects Agency's (DARPA) and has completed its system test and demonstration (T&D). For that phase, a set of metrics were defined to evaluate the telescope's ability to perform the SSA mission. According to the SST Phase I System T&D Procedure, "(e)ach system performance metric (SPM) is traceable to component and subsystem specifications of the underlying technology development...(t)hey are the core metrics that constitute the crux of the SST's performance, those that will enable the efficiencies of synoptic search [15]." Therefore, improvements to these SPMs will provide more overall system capability. The metrics are:

- I. Search rate: Ω [deg²/hr] vs. m_{ccd} (instrument magnitude)
- II. Metric accuracy: $\Delta\theta$ [arc sec] at nominal m_{ccd}
- III. Photometric accuracy: Δm_{ccd} at nominal m_{ccd}
- IV. Sensitivity: m_{ccd} vs. t (integration time) in various tracking modes

Metric I measures the search rate, Ω , with different integration times (i.e. target instrument magnitude (m_{ccd})) to quantify the performance traded off between sensitivity and search rate. Metric II measures the telescope's metric accuracy, $\Delta\theta$, as a function of m_{ccd} . Metric accuracy represents error in the estimates of an object's azimuth and elevation in units of arc seconds. Metric III evaluates the variance of m_{ccd} and is produced by comparing the object of interest brightness (i.e. digital counts) to the known brightness of stars in the FOV. Metric IV, the system sensitivity, is measured in terms of m_{ccd} and is evaluated as a function of integration time, t .

The remote sensing research accomplished and discussed in this dissertation can improve the SST's performance on three of the four SPMs. In particular, the multi-

hypothesis test (MHT) that is introduced in Chapter IV has new properties that could be used as the kernel of an entirely new image processing scheme. This algorithm has the potential to significantly outperform the baseline algorithm. Metric accuracy can be improved with the sub-pixel position information inherent to the MHT. Photometric accuracy should also be improved because the output of the MHT can be used to estimate photons in both the pixel in which the object is detected and the neighboring pixels. Finally and most importantly, the sensitivity gains provided by the MHT are demonstrated using experimental data from the SST.

1.2 Accomplished Work

Improving the detection performance of the SST through image processing enhances the detection of dim objects and the rejection of false alarms without requiring significant changes to the telescope's design or operations [16]. The following three concepts were identified in the prospectus and investigated in the research for improving the detection sensitivity of the SST.

1. Determine a better way to retrieve phase information from the SST data.
2. Investigate multi-hypothesis testing (MHT) to improve detection performance.
3. Mitigate star crossings from affecting the detection of an object.

This document is divided into six chapters that provide background, details on the work accomplished, and final conclusions that are intended to show how these concepts were investigated. In Chapter II, the background information provided includes a literature review, an introduction to the fundamental image processing concepts used in this work, and the foundation for this research. There are two chapters on phase retrieval. Chapter III describes a phase retrieval technique with a long exposure atmospheric model

useful for the current SST shutter camera, while in Chapter V, phase retrieval with a short exposure model is investigated for a future frame transfer camera. Phase information is important because it is used to quantify the presence of optical aberrations in the telescope [17]. More accurate information about the phase should help improve the process of focus and alignment resulting in sharper images. Focusing reduces the point spread function (PSF) and increases the signal-to-noise ratio (SNR) so that the SST's detection performance will be improved using its existing and future detection algorithms. The Cramer-Rao Lower Bound (CRLB) calculations demonstrate that improved aberration estimates are possible in certain coefficient ranges. New algorithms are then derived to accomplish improved optical aberration estimates [18, 19].

Both long and short exposure atmospheric models are used in the different phase retrieval techniques investigated [20]. The long exposure model is necessary for the current camera and physical shutter on the SST system. However, future variants of the SST or other ground-based three mirror telescopes like the Large Synoptic Survey Telescope (LSST) may benefit from phase retrieval with a short exposure atmospheric model [21]. For the SST, if a new frame transfer camera is procured it would enable the telescope to take short exposure images. Both long and short exposure phase retrieval techniques have performance advantages and limitations that are discussed in Chapter VI.

Phase retrieval is also critical to achieving the potential detection and false alarm improvements afforded by the new detection algorithm described in Chapter IV. The new detection algorithm leverages the long exposure phase retrieval outputs to form the PSF estimate used in a new multi-hypothesis test (MHT) for the detection of dim objects. Choosing the best available detection algorithm is critical to maximizing detection

sensitivity of the telescope. A thorough comparison of the current and proposed detection algorithms using satellite eclipse experiment data provides a side-by-side comparison of techniques. Algorithm performance assessment is based on detection improvement, computational burden and implementation complexity. The MHT algorithm mitigates the effects of aliasing caused by undersampling of the image and employs a new method of background noise calculations that reduces the noise degradation associated with star crossings. The MHT significantly improves the probability of detecting uncorrelated targets (UCTs) over the algorithm currently used by the SST. The Chapter VI conclusions highlight the significant improvement in the SST's detection sensitivity and the phase retrieval findings discovered in this research effort. Suggestions for future areas of investigation to further enhance the performance of the telescope are also discussed.

II. Background

The act of finding space objects with ground based telescopes has been performed by astronomers since the 17th century [22]. The incorporation of CCD arrays in place of film or the human eye has enabled modern image processing techniques to be used for detection of space objects [23, 24, 25]. The SST's current detection method is based on an algorithm used for the Lincoln Near Earth Asteroid Research (LINEAR) mission conducted at the Experimental Test Site near Socorro, NM. Viggh *et al.* described the LINEAR detection algorithm using a similar block diagram to the one shown in Figure 3.

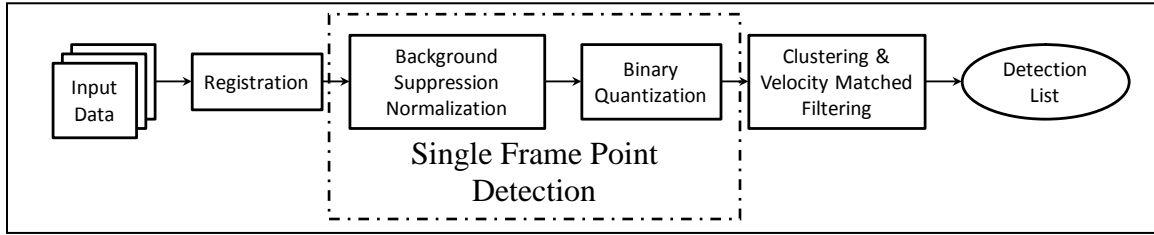


Figure 3. The SST detection block diagram [25]

The SST's current demonstration software uses input data that is comprised of three to five image frames of the sky in either a sidereal or a satellite track mode. Each frame is exposed over a user defined integration time period optimized to find UCTs. Image registration corrects for telescope pointing errors by using stars with known coordinates in each of the image frames. The single frame point detection of an object is performed in a two step process of background suppression normalization followed by binary quantization, which is described mathematically in Section 2.4. In each frame, adjacent pixels that have objects above the detection threshold are clustered together and classified as a single object. The algorithm then determines the centroid and extent of each

clustered object. The data is then filtered using a velocity matched filter to remove any objects not moving at the rate of the object(s) of interest. This is possible because in rate track mode the object in Earth's orbit will be stationary and the stars will be moving in the image between frames at the sidereal rate. The opposite is true when the telescope is in sidereal track mode. In addition, in order to reduce false alarms without changing the single frame detection threshold, objects that are not detected in three to five consecutive frames are also removed. Once the UTC is identified, the visual magnitude of that object is determined with a plate model that uses calibration stars in the FOV [3, 26]. Finally, the orbit determination of the UCT is determined by revisiting the object's initial coordinates at a later time.

The critical step in the existing software described above is the single frame point detection step because only objects that exceed the detection threshold have the potential for being discovered by the detection algorithm. Therefore, improvements in single frame point detection will improve the overall performance of the system. Two possible methods for improving the single frame detection are reducing the spot size to increase the pixel SNR or to use a matched filtering operation based on a model of the PSF. The phase retrieval methods discussed in this dissertation have the potential to improve the understanding of the telescope's aberrations for focus and alignment. These methods could be used to decrease spot size and the detection methods are proven to provide enhanced single-frame probability of detection.

The background provided in this section is intended to cover the fundamental concepts reviewed in literature pertinent to the completed research. The telescope model, Zernike polynomials and atmospheric models described are well accepted in the field of

applied optics and form the underlying principles for the new techniques developed in the phase retrieval and detection chapters.

2.1 Telescope Model

For both phase retrieval and the MHT, a wave model of the telescope is used to describe the optical aberrations and resulting PSF model. The aberrations are parameterized using Zernike polynomials because they are directly related to the wavefront errors associated with the optical prescription of the telescope [17]. In addition, the Zernike polynomials can be used to model the atmosphere for short exposure imagery [27, 28]. The polynomials are defined on the unit circle and form an orthonormal basis set for polynomial decomposition of wavefront error [29].

2.1.1 Zernike Polynomial for Defocus

One of the easiest ways to understand how wavefront errors are introduced into an optical system is by studying the aberration known as defocus. In an ideal single lens optical system, the rays of light associated with a plane wave produced by an object infinitely far from the lens (effectively a point source) are focused to a diffraction-limited spot at the focal point of the lens as illustrated in Figure 4 [30, 31]. Moving the image plane before or after the focal plane causes defocus to occur, this introduces a wavefront error in the pupil plane that can be quantified using the Zernike polynomial for defocus. The farther the image plane is from the focal plane, the more the Zernike polynomial for defocus has to be scaled using the Zernike coefficient for defocus to accurately model the additional wavefront error of the optical system.

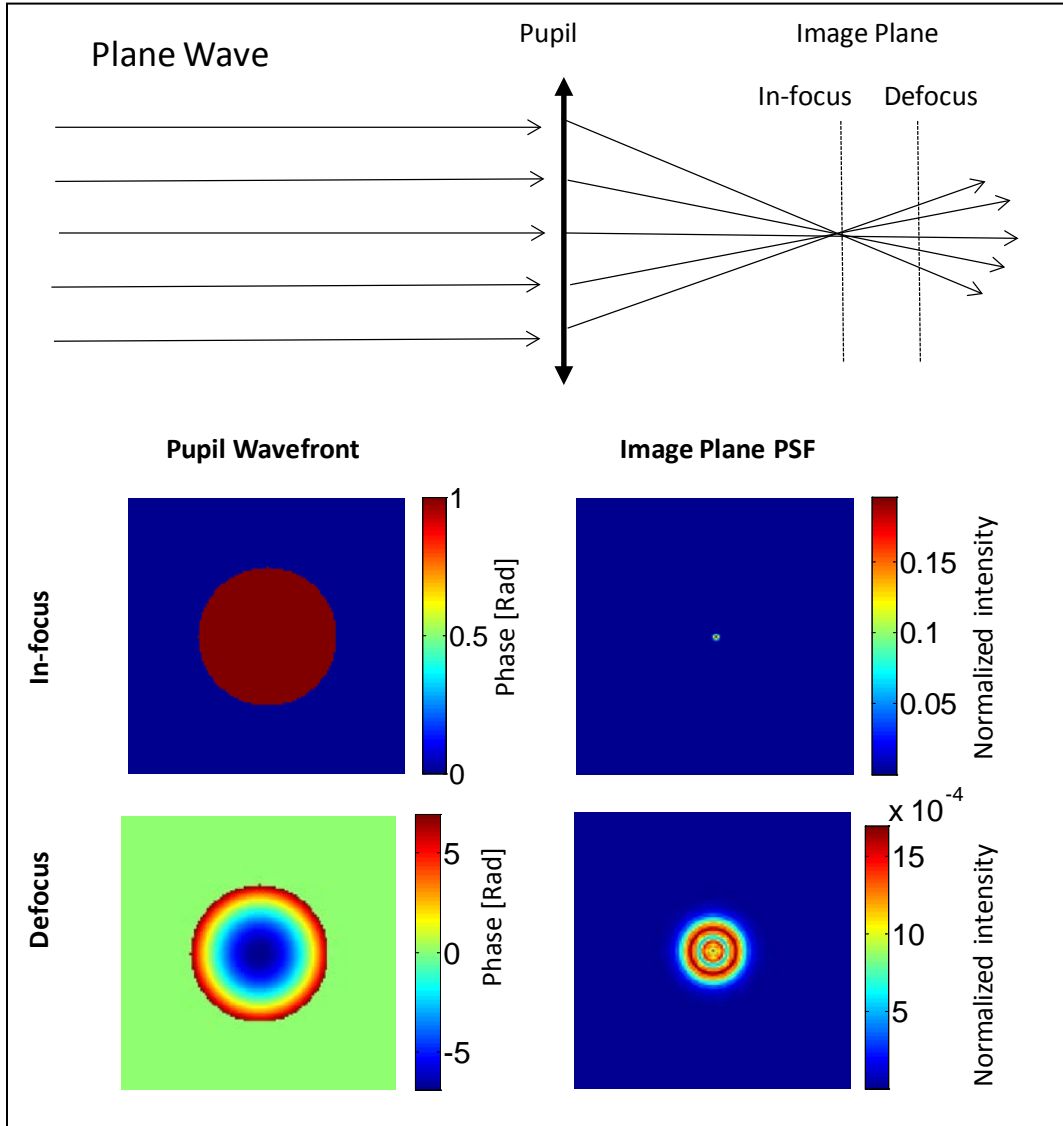


Figure 4. Illustration depicting how moving the image plane away from the focal plane of a single lens system introduces a 2-D wavefront phase error that can be parameterized by the Zernike polynomial for defocus.

To produce the wave model of a telescope, the aberrations are summed together in its exit pupil, where the aberration free pupil transmittance function, $A(u,v)$, has the coordinates u and v in the pupil plane. Wavefront error, $W(u,v)$, caused by defocus is

introduced into the pupil function using the Zernike polynomial for defocus, $\phi_4(u, v)$, which is [31]

$$\phi_4(u, v) = 3.464(u^2 + v^2) - 1.732. \quad (2.1)$$

The amount of focus error is captured by scaling $\phi_4(u, v)$ with a Zernike coefficient for defocus, Z_4 , such that

$$W(u, v) = Z_4 \cdot \phi_4(u, v). \quad (2.2)$$

An image of the unscaled $\phi_4(u, v)$ is shown at the bottom of Figure 4.

2.1.2 Zernike Polynomials and the Generalized Pupil Function

Compressing the notation from two dimensions (2-D) to one (1-D) for simplified presentation, the wavefront error, $W(u_1)$, in an optical system can be decomposed into N -number of Zernike polynomials, $\phi_1(u_1) - \phi_N(u_1)$, represented as

$$W(u_1) = Z_1 \cdot \phi_1(u_1) + \dots + Z_N \cdot \phi_N(u_1), \quad (2.3)$$

where u_1 is a coordinate in the pupil plane and $Z_1 - Z_N$ are the Zernike coefficients [31].

Images of the first eleven lower order Zernike polynomials, ϕ_2 to ϕ_{11} , except piston, ϕ_1 , are shown in Figure 5. Each of these lower order polynomials can be associated with aberrations that arise from imperfection in the optical design or optical alignment and are used in the SST's current alignment process [17].

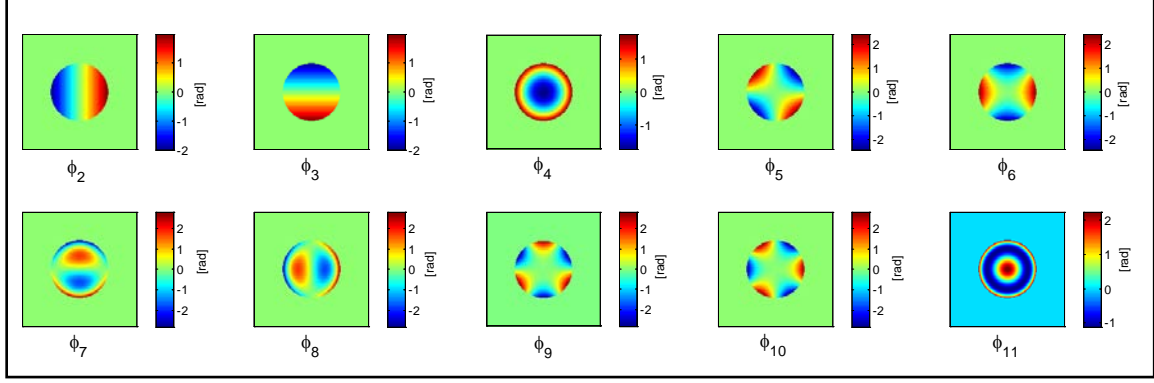


Figure 5. Images of Zernike polynomials numbers 2-11

The aberrated wavefront error is represented in the generalized pupil function,

$\mathcal{P}(u_1)$, as

$$\mathcal{P}(u_1) = A(u_1) \exp[j \cdot W(u_1)], \quad (2.4)$$

where $A(u_1)$ is the pupil transmittance function [31]. From the generalized pupil function, a model of the electric field, $H(m)$ in the image plane as a function of image plane pixel coordinates, m , is computed using a discrete Fourier transform,

$$\begin{aligned} H(m) &= \sum_{u_1} P(u_1) \exp(j2\pi m u_1) \\ &= \mathcal{F}[P(u_1)] \end{aligned} \quad (2.5)$$

and the corresponding optical PSF, $h(m)$ is

$$h(m) = |H(m)|^2 = H(m) \cdot H(m)^*. \quad (2.6)$$

2.1.3 Intensity Model and PSF Estimation

The images of stars that are recorded by a telescope can be modeled using its PSF.

The intensity model for the star irradiance centered on the optical axis is

$$i(m) = \theta_1 \cdot h(m) + B. \quad (2.7)$$

It includes additional terms to account for the background light, B , and the total number of photons emitted from the star per integration time, θ_1 [32]. Having an accurate PSF and intensity model for the stars is critical for both the phase retrieval and detection algorithms that are explored in this work.

2.2 Phase Retrieval from Stellar Images

Phase retrieval is a set of techniques used to determine the phase aberrations of an optical system using point source image intensity data (i.e. system impulse response). The SST phase aberrations must be recovered using post processing because the focal surface array cannot measure the phase directly. The existing phase retrieval methods identified from literature include curvature sensing, least squares fitting and the Gerchberg-Saxton algorithm [33, 34, 35]. The predominate limitation of curvature sensing and least squares fits is that they require the point source image to be defocused to generate enough phase diversity to distinguish the contribution of each of the polynomial to the total wavefront error and corresponding intensity in the image plane [17, 35]. The Gerchberg-Saxton (GS) algorithm on the other hand is limited because it produces a wrapped 2-D phase for larger aberrations. Attempts have been made to produce reliable 2-D phase unwrapping algorithms, but their performance is ultimately limited by branch cuts and noise [36, 37].

All the aforementioned phase retrieval techniques require short exposure images to work in the presence of an atmosphere. When long exposure imagery is used for phase retrieval these methods prove unreliable [18]. A method that works to some extent with the long exposure imagery and has been used to estimate the SST's optical prescription is

the Donut software. However, the phase retrieval with Donut was only conducted on nights with excellent seeing, which minimized the effects of the atmosphere [17].

The current process for alignment of the SST's optics is critically reliant on the Donut software. The Donut software's dependence on curvature sensing for its initial estimates of the lower order Zernike aberration coefficients (Z_2 - Z_6) is a problematic point because the SST alignment process requires Zernike coefficients up to at least Z_{11} . A second weakness in the method is that curvature sensing does not account for the atmospheric blurring, so poor seeing conditions will cause error in the initial Zernike estimates. To mitigate this known limitation, the site engineers monitor the seeing conditions and only align the optics on nights with good atmospheric conditions ($r_0 \geq 10$ cm). The third weak point in the algorithm is that the telescope must be out of focus to work, but in the process of refocusing the telescope the aberrations are likely to change.

With future SST sites planned in places with less ideal atmospheric seeing conditions than New Mexico, there will be a need to correctly estimate the Zernike coefficients in poor atmospheric conditions. For instance, sites surveyed in Australia have seeing parameter estimated as poor as an r_0 of 6 cm on average. Therefore, finding a better phase retrieval method that can more reliably estimate higher order Zernike coefficients, account for long exposure atmospheric effects, and work in-focus should help to better align the SST and produce a more accurate PSF model.

In this dissertation, two new phase retrieval approaches that can improve the performance of the SST are described. Both techniques achieve joint estimation of the static telescope aberrations without requiring defocusing of the telescope. This is more

useful because moving the SST's secondary and tertiary mirrors for defocusing is not practical on a regular basis. In addition, changes to the phase errors over time are not measurable with the current phase retrieval techniques from focused star images so the phase errors cannot be continuously monitored or removed. The estimation of the telescope's PSF model from a focused spot is used for the MHT. Also, a more accurate PSF could improve the SST's detection performance.

2.2.1 CRLB for Zernike Coefficients

In order to explore the theoretical performance of jointly estimating Zernike coefficients for unbiased estimators, the Cramer-Rao lower bound (CRLB) is used to provide the statistical lower limit for variance of estimated Zernike coefficients [38]. Fienup *et al.* derived the CRLB for estimates of Zernike coefficients to characterize the aberrations in the Hubble Space Telescope (HST) using phase retrieval [32]. The CRLB derived for the HST Zernike estimates did not include a parameter for the atmosphere because the HST is above the atmosphere. A derivation for the CRLB for Zernike coefficient estimates that includes the seeing parameter in Chapter III provides a tool for comparing the theoretical performance of the long exposure atmospheric phase retrieval method with phase retrieval when no atmosphere is present [19].

2.2.2 Least Squares and Gerchberg-Saxton Phase Retrieval

In their paper, Krist *et al.* describe a Levenberg-Marquardt least-squares (LS) method to estimate the low order Zernike coefficients from imagery data for the aberrations in the HST before and after correction [34, 35]. In order for the LS technique

to work, it required them to decouple the aberrations by defocusing the telescope to introduce phase diversity. In Krist's paper, the lower order aberrations are determined and the remaining phase errors are retrieved using *Gerchberg-Saxton* (GS) phase retrieval [34]. The decomposition of the remaining phase into Zernike polynomials is possible because the phase errors were small enough that they remained unwrapped. Using the orthonormality of the Zernike polynomials, they determine the magnitude of the Zernike coefficients from the GS phase.

The process for GS phase retrieval is illustrated in Figure 6 [34]. The algorithm begins with initialized wavefront error, $W(u_1)$, by multiplying reasonable initial conditions for the Zernike coefficients, (Z_1, Z_2, \dots, Z_N) , with their respective Zernike polynomials, $(\phi_1, \phi_2, \dots, \phi_N)$, represented as

$$W(u_1) = Z_1 \cdot \phi_1(u_1) + \dots + Z_N \cdot \phi_N(u_1), \quad (2.8)$$

where u_1 is a coordinate in the pupil plane and N is the total number of Zernike coefficients to be estimated. The aberrations are represented in the generalized pupil function as

$$\mathcal{P}(u_1) = A(u_1) \exp[j \cdot W(u_1)], \quad (2.9)$$

where, $A(u_1)$ is the pupil function. From the generalized pupil function a model of the electric field, $H(m, W)$, in the detector plane as a function of CCD pixel coordinates, m , and pupil plane wavefront, W , is computed using a discrete Fourier transform,

$$H(m, W) = \sum_{u_1} P(u_1) \exp(j2\pi m u_1) = \sqrt{h(m)} \exp[j \cdot \varpi(m)] \quad (2.10)$$

where $\varpi(m)$ is the phase of the electric field in the image plane. The square root of the measured PSF estimated from the image intensity data, $\sqrt{\hat{h}(m)}$, replaces the square root of the predicted PSF, $\sqrt{h(m)}$, which is output from the fast Fourier transform (FFT). Then the new field is inversely Fourier transformed to obtain a new estimate for the phase in the pupil plane. Next, the estimated pupil function, $A'(u_1)$, is replaced by the known pupil and the process is repeated for a fixed number of iterations (300 iterations for the GS phase retrieval algorithms used in this dissertation) to estimate the phase, $\hat{W}(u_1)$ [31]. While the technique provides a wrapped phase that is difficult to unwrap for Zernike decomposition, it also provides estimates of the electric field in the focal plane. The estimated electric field, $\hat{H}(m)$, proves useful in estimating the Zernike coefficients with the short exposure atmospheric technique described in Chapter V.

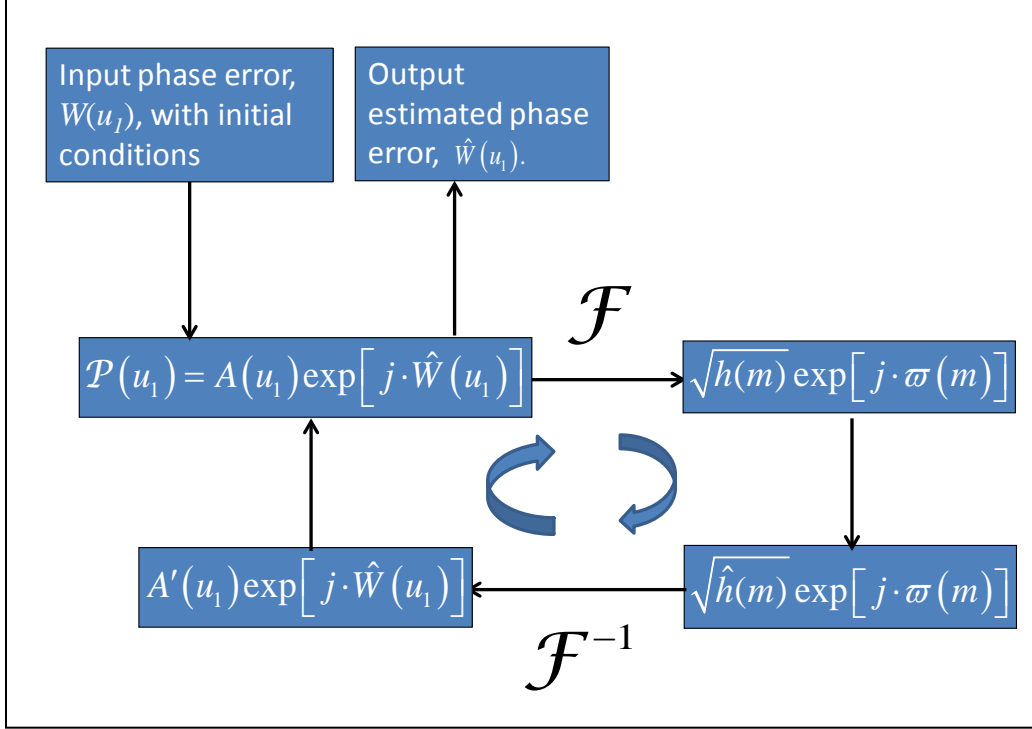


Figure 6. Gerchberg-Saxton phase retrieval block diagram

2.2.3 Curvature Sensing

Roddier developed the curvature sensing method to determine the low order aberrations in a telescope by defocusing the image [33]. The presence of aberrations causes the intensity of the edge of the defocus spot to curve in a way that can be used to determine the Zernike coefficients. Later, a single plane technique for curvature sensing was developed by Hickson [39]. Single plane curvature sensing gives the initial estimates used by the Donut algorithm [17]. Those estimates are then locally adjusted to refine the estimate using the Zemax® optical ray tracing software and tested on the telescope to see if the aberration estimates become better or worse in an iterative alignment process.

2.3 Atmospheric Models

Two different models for the atmosphere can be used to determine the atmospheric effects on the total phase and PSF of the optical system. The long exposure atmospheric model applies when exposure times of images viewed through the Earth's atmosphere are much greater than 10 ms [20]. Whereas, the short exposure atmospheric model holds for exposure times that are much less than 10 ms. The two different models affect the total phase and PSF in different ways, and therefore change the method of phase retrieval techniques required to determine an accurate model of the telescope's phase errors and PSF.

2.3.1 Long Exposure Atmosphere

Because SST uses a shutter with an integration time greater than 25 ms, an accepted model for that atmosphere is a long-exposure atmospheric transfer function, which is defined by Goodman as [20]

$$\mathcal{H}_{atm}(u_2) = \exp \left\{ -3.44 \left(\frac{\bar{\lambda} \cdot f \cdot u_2}{r_0} \right)^{5/3} \right\}. \quad (2.11)$$

In Eq. (2.11), $\bar{\lambda}$ is the mean wavelength, f is the telescope focal length, u_2 is spatial frequency, and r_0 is the atmospheric seeing parameter. The transfer function of the optical system, $\mathcal{H}_{opt}(u_2)$, can be determined from by taking the Fourier transform, \mathcal{F} , of the modeled optical PSF, $h_{opt}(m)$, as

$$\mathcal{H}_{opt}(u_2) = \mathcal{F}[h_{opt}(m)]. \quad (2.12)$$

The long exposure PSF, $h_L(m)$, is then computed using the inverse Fourier transform, \mathcal{F}^{-1} , of the combined atmospheric and optics transfer functions. The effect of the finite square pixel width, a , is determined using a rectangle function with the following transfer function

$$\mathcal{H}_{pixel}(u_2) = \mathcal{F}[rect(a \cdot m)]. \quad (2.13)$$

The modeled PSF centered on a pixel is then computed as

$$h_L(m) = \mathcal{F}^{-1}[\mathcal{H}_{opt}(u_2) \cdot \mathcal{H}_{pixel}(u_2) \cdot \mathcal{H}_{atm}(u_2)]. \quad (2.14)$$

By including the effects of the long exposure atmosphere in the PSF, the point source image intensity model, $i_L(m)$, becomes

$$i_L(m) = \theta_1 \cdot h_L(m) + B. \quad (2.15)$$

2.3.2 Short Exposure Atmosphere

For ground based telescopes with frame transfer cameras, such as potential future variants of the SST, the exposure time can be limited to a period where the short exposure model applies. The short exposure atmosphere can be described by a set of Zernike polynomials, which have coefficients that are zero mean Gaussian random variables [27, 28, 40]. Therefore, the wavefront error for a telescope with a short exposure atmosphere, W_{total_s} , can be represented by expanding Eq. (2.3) to include the atmospheric contribution to the Zernike coefficients, Z_{2_atm} to Z_{N_atm} , along with the static telescope optical aberrations Zernike coefficient, Z_{2_opt} to Z_{N_opt} . The total short exposure wavefront error, W_s , from both the static optical aberrations and the

atmospheric aberrations can be describe using the linear combination of the scaled polynomials

$$W_S = (Z_{2_opt} + Z_{2_atm}) \cdot \phi_2 + \dots + (Z_{N_opt} + Z_{N_atm}) \cdot \phi_N. \quad (2.16)$$

By using the combined atmosphere and telescope wavefront error from Eq. (2.16) and then inserting it into Eqs. (2.4), (2.5) and (2.6) the combined PSF of the short exposure atmosphere and the telescope, $h_s(m)$, and is found as,

$$h_s(m) = \left| \sum_{u_1} A(u_1) \cdot e^{jW_S(u_1)} \cdot e^{j2\pi mu_1} \right|^2. \quad (2.17)$$

To include the pixel effect the short exposure OTF, $\mathcal{H}_s(u_2)$, is

$$\mathcal{H}_s(u_2) = \mathcal{F}[h_s(m)], \quad (2.18)$$

and the pixilated short exposure PSF, $h_{s_pix}(m)$, is

$$h_{s_pix}(m) = \mathcal{F}^{-1}[\mathcal{H}_s(u_2) \cdot \mathcal{H}_{pixel}(u_2)]. \quad (2.19)$$

Then the short exposure intensity model, $i_s(m)$, is computed as

$$i_s(m) = \theta_1 \cdot h_{s_pix}(m) + B. \quad (2.20)$$

Accurate modeling of the long and short exposure PSF and corresponding intensity models is critical for both long and short exposure phase retrieval. In addition, a MHT is not possible without an accurate long exposure image intensity model, $i_L(m)$.

2.4 Detectors

Two types of optical detection processes of unknown space objects with ground based telescopes are discussed in the literature. The first type of detection algorithm is based on images with a limited exposure time such that objects in the field of view can be

treated as point sources [25, 41, 42]. In the other type of detection algorithm, the integration time is longer and the system is not tracking the object causing each of the moving objects to streak over multiple pixels within the frame [23, 24]. The image processing technique for the detection of space objects used by the SST limits the exposure time such that the objects can be treated as point sources. Therefore, the detection algorithms covered in the comparative analysis in this body of work are designed to detect point sources not streaks.

The three single frame detection schemes based on point sources images identified to date are background suppression normalization & binary quantization, linear threshold correlation, and non-linear threshold correlation [25, 41, 42]. All three detectors can be derived from a binary hypothesis test expressed as the following likelihood ratio tests (LRT) for uniform cost and equal priors [1]

$$\Lambda = \frac{P(d(w, z) \forall (w, z) \in [1, M_d] | H_1)}{P(d(w, z) \forall (w, z) \in [1, M_d] | H_0)} \underset{H_0}{\overset{H_1}{>}} 1, \quad (2.21)$$

where $d(w, z)$ is the image data, w and z are integer pixel coordinates and M_d is the number of pixels in one dimension of a chosen square window in detector plane. In this case, H_1 is the hypothesis that an object is present in the pixel of interest and H_0 is the hypothesis that an object is not present in the pixel of interest. The joint conditional probability of the data given hypothesis $H_i, i \in \{0, 1\}$ is true, is

$$P(d(w, z) \forall (w, z) \in [1, M_d] | H_i).$$

2.4.1 Point Detection

The detector currently used by the SST is based on background suppression normalization and binary quantization, which is a process of detecting an object in a single CCD pixel. It will be also referred to as either a point detector or the baseline detector. As stated at the beginning of the chapter, the detection algorithm currently used in the SST is adopted from the algorithm developed for LINEAR [25]. Mathematically, the single frame point detection of an object from the SST imagery data, $d(c_x, c_y)$, in a pixel with coordinates (c_x, c_y) is performed as

$$SNR(c_x, c_y) = \frac{(d(c_x, c_y) - B)}{\sigma} \underset{H_0}{\overset{H_1}{>}} \gamma, \quad (2.22)$$

where B is the local background, σ is the standard deviation of the noise, and γ is the detection threshold. The background, B , can be computed as the local sample median of the data,

$$B = \text{median}[d(w, z) \forall (w, z) \in [1, M_d]], \quad (2.23)$$

and the local standard deviation is

$$\sigma \approx \sqrt{\frac{\sum_{w=1}^{M_d} \sum_{z=1}^{M_d} d^2(w, z)}{M_d^2} - B^2}, \quad (2.24)$$

where M_d is the number of pixels in one dimension of a chosen window in the detector plane centered on the pixel of interest, (c_x, c_y) . Pixels with a SNR greater than the detection threshold are classified as containing a target and passed on for further processing.

For this method of single frame point detection, the SNR is degraded significantly because the SST's PSF is much larger than the size of a single pixel, therefore the SST data is binned into 2 by 2 pixels. While this method is relatively effective, its performance is still inhibited by two key physical limitations. The first issue with this detector is that the telescope cannot focus the light from a star into a binned pixel causing a decrease in SNR output of the point detector. The second is that the objects are not always centered on a single binned pixel so that when an object falls in the corner or side of a pixel the SNR is greatly reduced.

2.4.2 Correlation versus Point Detection

The correlator is designed to achieve a chosen probability of false alarm, P_{FA} , under the H_0 case and the image noise is modeled as Gaussian, which matches the SST noise distribution. A Poisson distribution for noise would also be equally valid, however Pohlig's derivation using that assumption led to a detector that was dependent on target irradiance [42]. To remove the detector's dependence on target irradiance a log approximation is made assuming that the target irradiance is low. Then the paper concedes that the distribution of the noise for these dim objects would not be Poisson, but have a similar distribution.

By choosing to use a Gaussian noise distribution the LRT becomes

$$\Lambda_G = \frac{P[d | H_1]}{P[d | H_0]} = \frac{\prod_{w=1}^{M_d} \prod_{z=1}^{M_d} \frac{1}{\sqrt{2\pi}\sigma} e^{\left\{ \frac{-1}{2\sigma^2} [d(w,z) - B - \theta h_L(w,z)]^2 \right\}}_{H_1}}{\prod_{w=1}^{M_d} \prod_{z=1}^{M_d} \frac{1}{\sqrt{2\pi}\sigma} e^{\left\{ \frac{-1}{2\sigma^2} [d(w,z) - B]^2 \right\}}_{H_0}} > 1, \quad (2.25)$$

where w and z are pixel locations in the window, and the long exposure PSF is $h_L(w, z)$.

The value M_d is the total number of pixels in the window, B is the background photon count in the image, θ is the space object's irradiance, and σ is the standard deviation of the noise. The sufficient statistic for the LRT is designed to maintain the same false alarm rate as the baseline detector, which is determined by the H_0 case. Taking the natural log, Eq. (2.25) reduces to the following form

$$\log(\Lambda_G) = \sum_{w=1}^{M_d} \sum_{z=1}^{M_d} \frac{1}{2\sigma^2} \left[-2B \cdot \theta h_L(w, z) + 2d(w, z) \cdot \theta h_L(w, z) - (\theta h_L(w, z))^2 \right] \begin{matrix} > \\ < \end{matrix} \begin{matrix} H_1 \\ H_0 \end{matrix} 0. \quad (2.26)$$

Since the PSF can be estimated independently from auxiliary processes, Eq. (2.26) can be rearranged as

$$\sum_{w=1}^{M_d} \sum_{z=1}^{M_d} (d(w, z) - B) h_L(w, z) \begin{matrix} > \\ < \end{matrix} \begin{matrix} H_1 \\ H_0 \end{matrix} \frac{\theta}{2} \sum_{w=1}^{M_d} \sum_{z=1}^{M_d} \left[(h_L(w, z))^2 \right]. \quad (2.27)$$

The selection of θ will be chosen to achieve the desired threshold. To convert Eq. (2.27) into a sufficient statistic in terms of signal-to-noise ratio (SNR), the background suppressed data is a new random variable, d_2 , with zero mean in the H_0 case [2],

$$d_2(w, z) = d(w, z) - B. \quad (2.28)$$

The correlation of the PSF with the background suppressed data then becomes

$$\sum_{w=1}^{M_d} \sum_{z=1}^{M_d} d_2(w, z) h_L(w - c_x, z - c_y), \quad (2.29)$$

where c_x and c_y are the coordinates of the pixel being tested. The resulting quantity also has a mean, μ_2 , where

$$\begin{aligned}
\mu_2 &= E \left[\sum_{w=1}^{M_d} \sum_{z=1}^{M_d} d_2(w, z) h_L(w - c_x, z - c_y) \right] \\
&= \sum_{w=1}^{M_d} \sum_{z=1}^{M_d} E[d_2(w, z)] E[h_L(w - c_x, z - c_y)] = 0,
\end{aligned} \tag{2.30}$$

and a variance, σ_2^2 , of

$$\begin{aligned}
\sigma_2^2 &= E \left[\left(\sum_{w=1}^{M_d} \sum_{z=1}^{M_d} d_2(w, z) h_L(w - c_x, z - c_y) \right)^2 \right] \\
&= E \left[\sum_{w=1}^{M_d} \sum_{z=1}^{M_d} d_2(w, z) h_L(w - c_x, z - c_y) \sum_{m=1}^{M_d} \sum_{n=1}^{M_d} d_2(m, n) h_L(m - c_x, n - c_y) \right] \\
&= \sum_{w=1}^{M_d} \sum_{z=1}^{M_d} \sum_{m=1}^{M_d} \sum_{n=1}^{M_d} E[d_2(w, z)] E[d_2(m, n)] h_L(w - c_x, z - c_y) h_L(m - c_x, n - c_y).
\end{aligned} \tag{2.31}$$

Eq. (2.31) can be simplified using two cases, one when $w \neq m$ and/or $z \neq n$ and the other when $w = m$ and $z = n$. Using the Kronecker delta function, $\delta(w - m, z - n)$,

$$\begin{aligned}
\sigma_2^2 &= \sum_{w=1}^{M_d} \sum_{z=1}^{M_d} \sum_{m=1}^{M_d} \sum_{n=1}^{M_d} E[d_2(w, z)] E[d_2(m, n)] \\
&\quad \times h_L(w - c_x, z - c_y) h_L(m - c_x, n - c_y) (1 - \delta(w - m, z - n)) \\
&\quad + \sum_{w=1}^{M_d} \sum_{z=1}^{M_d} E[d_2^2(w, z)] h_L^2(w - c_x, z - c_y) \delta(w - m, z - n) \\
&= \sigma^2 \sum_{w=1}^{M_d} \sum_{z=1}^{M_d} h_L^2(w, z).
\end{aligned} \tag{2.32}$$

Therefore, the standard deviation of the normalized data convolved with the total system PSF is

$$\sigma_2 = \sigma \sqrt{\sum_{w=1}^{M_d} \sum_{z=1}^{M_d} h_L^2(w, z)}. \tag{2.33}$$

The sufficient statistic for the correlator is then found by dividing Eq. (2.27) by Eq.

(2.33). Then the LRT reduces to the following correlation operation normalized in terms

of the correlator's signal-to-noise ratio, SNR_{corr} ,

$$SNR_{corr} = \frac{\sum_{w=1}^{M_d} \sum_{z=1}^{M_d} (d(w, z) - B) h_L(w - c_x, z - c_y)}{\sigma \sqrt{\sum_{w=1}^{M_d} \sum_{z=1}^{M_d} h_L^2(w, z)}} \underset{H_0}{\overset{H_1}{>}} \frac{\frac{\theta}{2} \sum_{w=1}^{M_d} \sum_{z=1}^{M_d} [(h_L(w, z))^2]}{\sigma \sqrt{\sum_{w=1}^{M_d} \sum_{z=1}^{M_d} h_L^2(w, z)}} = \gamma. \quad (2.34)$$

The results of the sufficient statistic are then compared against the selected SNR threshold, γ , which is set to achieve a desired P_{FA} .

In the case of the baseline point detector, the PSF is one pixel represented as a delta function, $\delta(w - c_x, z - c_y)$. The sufficient statistic for the baseline detector in terms of the point detector's signal-to-noise ratio, $SNR_{Baseline}$, is

$$SNR_{Baseline} = \frac{\sum_{w=1}^{M_d} \sum_{z=1}^{M_d} (d(w, z) - B) \delta(w - c_x, z - c_y)}{\sigma \sqrt{\sum_{w=1}^{M_d} \sum_{z=1}^{M_d} \delta^2(w, z)}} = \frac{(d(c_x, c_y) - B)}{\sigma} \underset{H_0}{\overset{H_1}{>}} \gamma \quad (2.35)$$

and can be compared against the same threshold as the correlator. The fact that both detectors are expressed in terms of SNR and use the same threshold makes the comparison of the two detectors possible. This is because for each pixel being tested the detectors will produce a SNR value. When comparing the two detectors, the detector that produces the higher SNR value will have the high performance.

2.4.3 Undersampling and Correlation Detection

While correlation detectors have better single frame detection performance than the point detectors currently used in the SST, adequate PSF spatial sampling can affect the probability of detection, P_d , for the correlator [25, 43]. O'Dell *et al.*'s paper shows the effects of undersampling images on the performance of correlation detectors for the optical detection of space objects. What O'Dell doesn't describe is how to improve

detection performance other than by increasing physical spatial sample rates. In other words, if the image can't be sampled at its Nyquist frequency, can the aliasing effect be mitigated using a modeled PSF?

To understand the Nyquist sampling in O'Dell's work, objects are treated as incoherent point sources of light and are propagated through an atmosphere causing the light to spread. For the simulations presented, the cutoff frequency,

$$f_c = \frac{2 \cdot r_0}{\lambda \cdot z_i}, \quad (2.36)$$

is limited by the atmospheric seeing parameter, r_0 , at a given focal length, z_i and wavelength, λ [31]. The difference between sampling to meet the Rayleigh criteria is that a pixel angle, Δ_R , is

$$\Delta_R = \frac{1.22\lambda}{r_0}, \quad (2.37)$$

and the Nyquist criteria has pixel angle, Δ_N , of

$$\Delta_N = \frac{\lambda}{2 \cdot r_0}. \quad (2.38)$$

The curves in Figure 7 (a) and (b) show the key finding of O'Dell's paper - the correlator has a higher P_d when the PSF is properly sampled [43]. When the object intensity is centered on a pixel the Rayleigh sampled correlator performance is not as drastically degraded as compared to the Nyquist case in Figure 7 (a). However, when the PSF is in the corner of a pixel, the Rayleigh sampled correlator has a significant reduction in detection performance as shown in Figure 7 (b).

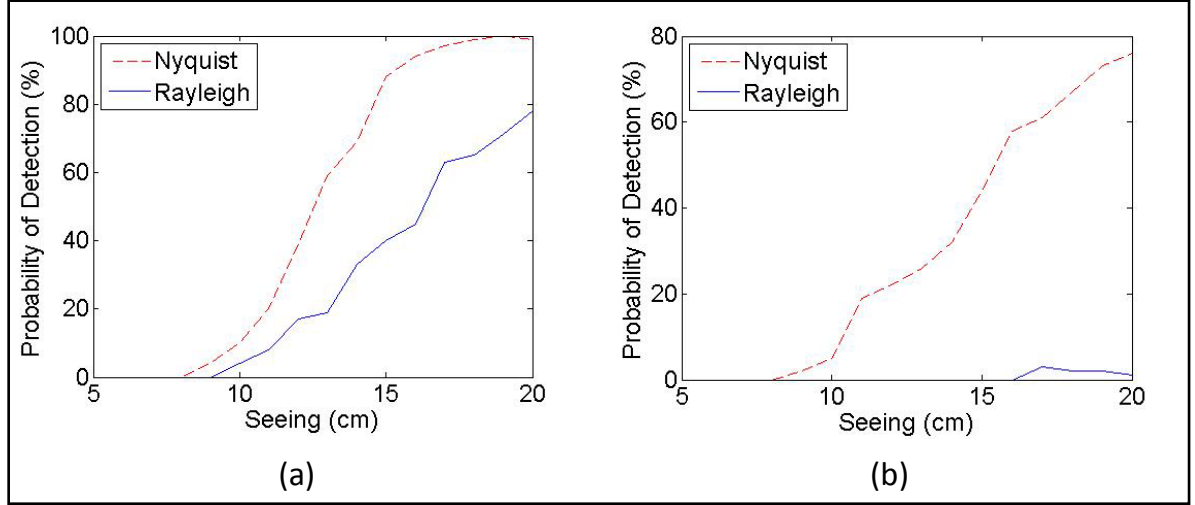


Figure 7. Comparison of aliased and unaliased detector performance for a fixed probability of false alarm (a) Nyquist and Rayleigh sampled correlator detection performance with PSF centered on a pixel. (b) Nyquist and Rayleigh correlator detection performance with PSF centered on the corner of a pixel [43].

2.5 Conclusions

The mission of synoptically searching deep space for unknown space objects has driven the requirements for wide FOV three mirror telescopes such as the SST and the Large Synoptic Survey Telescope (LSST) [1, 21]. The tertiary mirror makes these complex telescopes considerably more difficult to align and focus than traditional two mirror telescopes driving the need of better phase retrieval methods [21, 44]. To compensate for the unavoidable blurring of images from the atmosphere and telescope aberrations, larger pixels (or binned pixels) are used to increase SNR with the unavoidable consequence of causing undersampling of the data [18, 43]. Detection can be improved by binning pixels to add together the spread signal with the SST's current detection algorithm. However, this approach is not ideal because it includes the addition of read noise from each pixel. Also, the PSF may not be centered on a pixel so that the irradiance will be detected across multiple binned pixels. Therefore, a detection

algorithm is needed that accounts for the PSF that spans more than one pixel and spatially filters the image with a model of the PSF to perform detection. Review of current literature, summarized in the remainder of this section, has revealed that existing phase retrieval algorithms and detectors have limitations that ultimately limit the optical detection of space objects.

Phase retrieval of Zernike coefficients has been successfully used to align the SST in good atmospheric conditions ($r_0 \geq 10$ cm) by defocusing the telescope, but techniques that work in less ideal conditions and in-focus are needed to maximize telescope performance [17]. A phase retrieval technique that works in-focus with any atmospheric conditions will provide the necessary aberration information from the SST's standard imagery data for focus and alignment. This can be accomplished without going through the complex procedure of moving the secondary and tertiary mirrors to defocus the telescope [18]. This would enable diagnostic monitoring of the telescope in order to maintain focus and alignment with standard imagery data. However, the current documented phase retrieval methods of curvature sensing, the Gerchberg-Saxton algorithm and least squares fitting are limited in their ability to accurately estimate Zernike coefficients with focused data [33, 34, 35, 45]. Thus, the new phase retrieval methods (discussed in Chapters III and V) that work in-focus with poor atmospheric conditions are desirable. In addition, the phase retrieval algorithm described in Chapter III has already proven useful in estimating PSFs for inclusion in a new detection strategy for the SST covered in Chapter IV.

The development of a phase retrieval algorithm that works in-focus would be useful not only for the focus and alignment of ground based telescopes, but also for space

based telescopes like the James Webb Space Telescope (JWST) projected to launch in 2018 [46]. Currently, NASA plans to use a phase retrieval algorithm called the hybrid diversity algorithm (HDA) that is based on the Gerchberg-Saxton algorithm with another process to perform phase-unwrapping [36, 45, 47]. The HDA requires phase diversity similar to the LM least squares method used for characterizing the HST [32]. The problem of generating phase diversity with defocus was overcome in the HST by moving the focal plane [32], however due to JWST three mirror design and segmented primary mirror, defocusing is not as simple [44]. To overcome that challenge, the JWST has additional optics on two separate wheels that can be rotated into the optical path to generate defocus [47, 48]. The JWST could potentially remove the requirements for these additional optical elements and reduce overall program risk by using the phase retrieval algorithm discussed in Chapter V.

In addition to sub-optimal phase retrieval methods, the SST's current detection performance is limited due to the design of its baseline detector [25]. A correlator, similar to the one developed for pan-STARRS, could improve the performance of the SST over the baseline detector, but it is ultimately limited by the SST's undersampled data [16, 41, 43]. Other correlation methods for the detection of space objects have been developed as discussed previously in this chapter. Those methods work with objects that move across multiple pixels during a single exposure causing streaks, whereas deep space objects imaged by the SST are effectively point sources due to short integration times [23, 24]. Each of the aforementioned detectors are based on a Gaussian parametric model for the noise; however, one other detector discussed in literature was based on a Poisson distribution of the noise [33]. The MHT is derived from a Gaussian LRT in Chapter IV

and works with point source data to improve the detection performance of the SST over both the correlator and its baseline detector by compensating for both blurring and undersampled data. The following three chapters cover the research accomplished to improve both phase retrieval and detection performance of the SST, but should also be extensible to other astronomical telescopes.

III. Phase Retrieval with a Long Exposure Atmosphere

One key image processing technique that improves the SST's detection is modeling the telescope's wavefront error with Zernike polynomials. Estimates of the Zernike polynomial coefficients produced by phase retrieval are used to better focus and align the telescope immediately improving SNR and thus the detection performance [17]. In addition, the same coefficients are used to model the telescope's point spread function (PSF), which can be used to improve the SST's detection sensitivity using the multi-hypothesis test discussed in Chapter IV.

The critical technology that enables the SST's 6 deg wide field-of-view (FOV) camera (shown in Figure 8) is the unique set of curved charged coupled device (CCD) arrays. The set of 12 separate curved CCD arrays are tiled together in a 6 by 2 mosaic that form a surface with a 5 m radius of curvature that alleviates some of the aberrations inherent to the optical design. During the design process, a choice was made to maintain the wide FOV of the telescope with the larger format (12288 by 8192) mosaic detector and a mechanical shutter rather than a smaller format mosaic detector in a frame transfer camera. Since the current camera does not have a frame transfer capability, a high speed shutter was developed for the camera with a minimum exposure time, τ , of 25 ms. This is still considerably longer than the $\tau < 10$ ms typically associated with a short exposure image [20].



Figure 8. The SST's 6 deg wide field-of-view camera and high speed mechanical shutter

One of the main challenges in optimizing the SST's performance is to reduce the point spread function (PSF) through focus and alignment. The pixels in the CCD are 15 μm . However, the pixels can be two by two binned to mitigate the degradation in detection sensitivity of the point detector that occurs due to atmospheric blurring and telescope aberrations. Figure 9 shows the variations of full width half maximum (FWHM) blur spot in terms of 30 μm binned pixels over three months leading up to the final alignment of the telescope. The FWHM is a measurement of the width across the irradiance pattern produced by the telescope's image of a point source at half the maximum value.

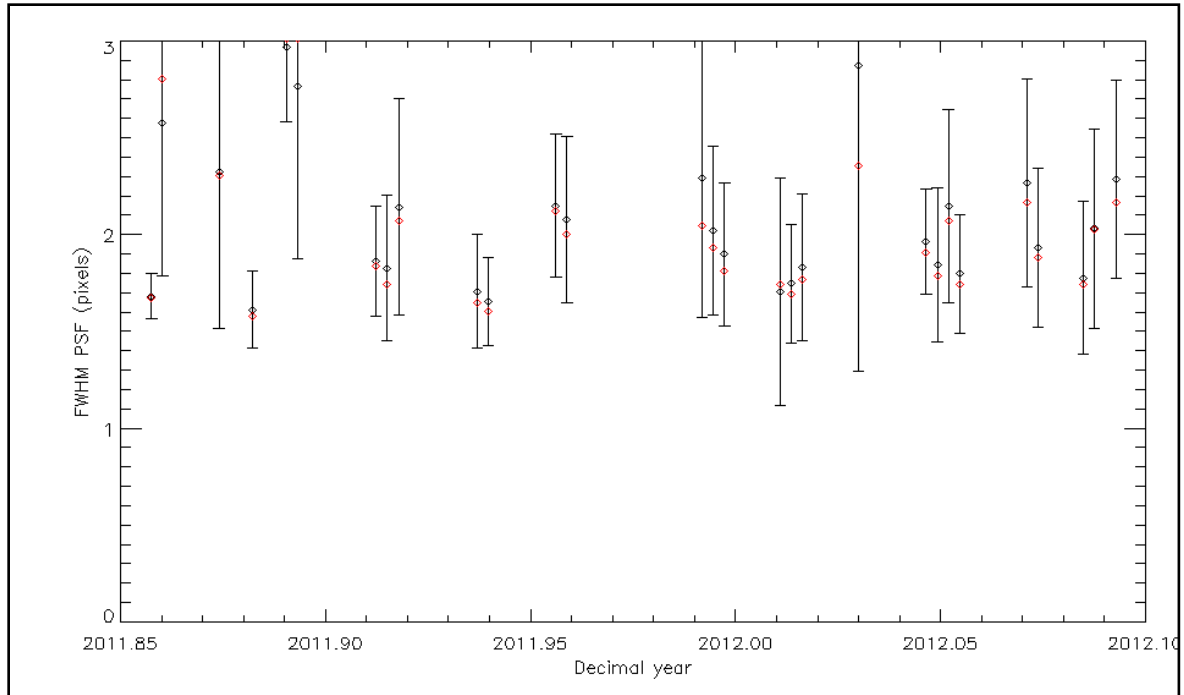


Figure 9. Variations in the Full Width Half Maximum (FWHM) of the SST's Point Spread Function (PSF) measured by 2 by 2 binned 15 μ m pixels. (provided by MIT/LL)

Ideally, the PSF FWHM would be within one 30 μ m binned pixel. Reducing the PSF size is possible by accurately determining the amount of focus error and other aberrations in the image of a calibration star, then adjusting the focus and alignment to reduce the blur spot size. However, to find unbiased estimates of the telescope aberrations from the star image, the atmospheric effects must be accounted for in the phase retrieval technique. As mentioned in Chapter II, the engineers only aligned the optics on nights with seeing greater than 10 cm. With future SST sites being surveyed in Australia, where there is less ideal atmospheric seeing conditions than in New Mexico, there will be a need to correctly estimate the Zernike coefficients in poor seeing conditions. This is one of the reasons that there is a need for improved phase retrieval techniques.

3.1 Telescope Model

The telescope model introduced in the background chapter and used for this analysis follows a similar model employed for phase retrieval of the HST aberrations before and after correction [32]. The SST is considered a linear shift invariant system with the impulse response of the system being the PSF. The light propagating from the distance point source, $\delta(x)$, is assumed to be temporally incoherent in the image plane with coordinates, x . The parameters used in the telescope model are listed in Table 1.

Table 1. Telescope Model Parameters

Parameter	Value
Center Wavelength	500 nm
Telescope Pupil/Obscuration Diameter	3.5 m / 1.8 m
Telescope Effective Focal Length	3.5 m
CCD Pixel Pitch	15 μ m
Star Irradiance per Frame	$\sim 10^4$ photons
Background Irradiance per Frame	300 photons

The SST's pupil transmittance function, $A(u, v)$, is defined by its annular aperture shown in Figure 10 (a), where u and v are coordinates in the pupil plane. Wavefront error caused by defocus is introduced into the pupil function using the Zernike polynomial for defocus, $\phi_4(u, v)$, [31],

$$\phi_4(u, v) = 3.464 \cdot (u^2 + v^2) - 1.732. \quad (3.1)$$

The amount of focus error is captured by scaling $\phi_4(u, v)$ with a Zernike coefficient for defocus, Z_4 . This product is used to express the wavefront error, $W(u, v)$, as

$$W(u, v) = Z_4 \cdot \phi_4(u, v). \quad (3.2)$$

An image of $\phi_4(u, v)$ scaled by a 25 wave coefficient is shown in Figure 10 (b).

Compressing the notation from two dimensions (2-D) to one (1-D) for simplified presentation, the aberrations are then represented with the pupil plane coordinates, u_1 , by the generalized pupil function, $\mathcal{P}(u_1)$, as

$$\mathcal{P}(u_1) = A(u_1) \exp[j \cdot W(u_1)]. \quad (3.3)$$

Then the telescope's PSF, $h_{opt}(m)$, is computed as [3]

$$h_{opt}(m) = \left| \sum_{u_1} \mathcal{P}(u_1) e^{j2\pi m u_1} \right|^2, \quad (3.4)$$

where m is a pixel coordinate in the detector plane. An image of $h_{opt}(m)$ with 25 waves of defocus is shown in Figure 10 (c). The large amount of defocus causes the PSF to have an annular shape.

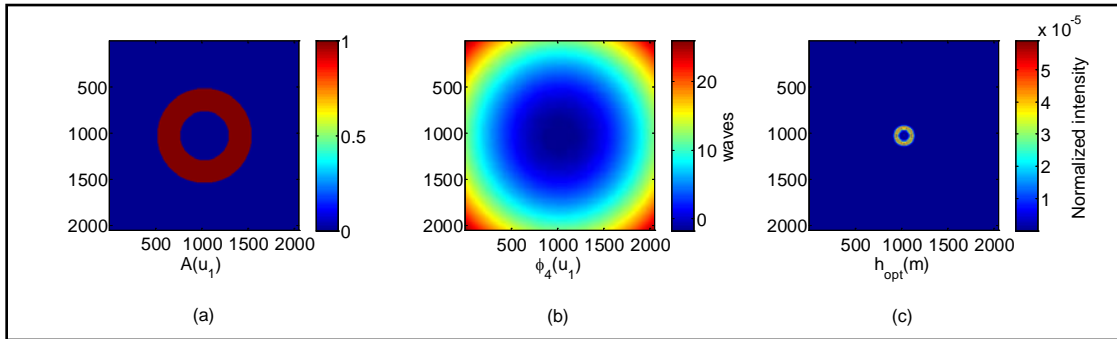


Figure 10. Telescope Model (a) Pupil function used to model the SST (b) Zernike polynomial for defocus with $Z_4 = 25$ waves (c) Telescopes PSF with $Z_4 = 25$ waves of focus error.

For a more complete model of the telescope, the effect of the finite square pixels, $a = 15 \text{ } \mu\text{m}$, is included in the PSF where the transfer function for the pixels, $\mathcal{H}_{pixel}(u_2)$, and telescope, $\mathcal{H}_{opt}(u_2)$, respectively are represented as the following discrete Fourier transforms, \mathcal{F} ,

$$\mathcal{H}_{pixel}(u_2) = \mathcal{F}[rect(a \cdot m)], \text{ and} \quad (3.5)$$

$$\mathcal{H}_{opt}(u_2) = \mathcal{F}[h_{opt}(m)], \quad (3.6)$$

where u_2 is the spatial frequency. Then the PSF for the telescope, $h_{telescope}(m)$, can be computed via the transfer functions as

$$h_{telescope}(m) = \mathcal{F}^{-1}[\mathcal{H}_{opt}(u_2) \cdot \mathcal{H}_{pixel}(u_2)]. \quad (3.7)$$

Bright star images observed by the SST have been measured to be shot noise dominated (see Appendix), so the image data, $d(m)$, is considered to be Poisson and has a mean value that is equal to the irradiance of light in that pixel [32]

$$E[d(m)] = i(m). \quad (3.8)$$

The model for the star irradiance centered on the optical axis is

$$\begin{aligned} i_{telescope}(m) &= \sum_x \theta_1 \cdot \delta(x) \cdot h_{telescope}(m - x) + B \\ &= \theta_1 \cdot h_{telescope}(m) + B. \end{aligned} \quad (3.9)$$

It includes additional terms to account for the background light, B , and the total photons emitted from the star per integration time, θ_1 . Assuming statistical independence between pixels, the joint distribution of the image data is represented by the Poisson probability mass function and details of the choice of this PMF can be found in the Appendix,

$$\prod_m P[d(m)] = \prod_m \frac{e^{-i_{telescope}(m)} \cdot i_{telescope}(m)^{d(m)}}{d(m)!}. \quad (3.10)$$

The associated log likelihood, $L(Z_4)$, equation is

$$\begin{aligned} L(Z_4) &= \ln \left(\prod_m P[d(m)] \right) \\ &= \sum_m \left\{ -i_{telescope}(m) + d(m) \cdot \ln i_{telescope}(m) - \ln d(m)! \right\}. \end{aligned} \quad (3.11)$$

3.2 Cramer-Rao Lower Bounds (CRLB) for Variance

The CRLB for variance presented in this section was derived in order to evaluate the performance of the joint estimator (i.e. phase retrieval) for the Zernike coefficients and the atmospheric seeing parameter. The CRLB for estimates of Zernike coefficients was previously derived for evaluating the phase retrieval performance on the HST [32]. The difference between the SST and the HST is that the HST does not have to image through the earth's atmosphere. The CRLB herein provides a theoretical lower limit of variance for unbiased estimates of the Zernike coefficient for defocus, \hat{Z}_4 , and the atmospheric seeing parameter, r_0 . Simulations presented in this chapter demonstrate that phase retrieval using a least squares estimator produces unbiased estimates of those two parameters [32].

The bounds in Figure 12 illustrate that standard deviations of \hat{Z}_4 on the order of 10^{-1} waves are possible at practical light levels even in the presence of long exposure atmosphere. To determine the CRLB for estimates of the Zernike coefficient for defocus the Fisher information, $J(Z_4)$, is computed via the following calculation [38],

$$J(Z_4) = -E \left[\frac{\partial^2 L(Z_4)}{\partial Z_4^2} \right]. \quad (3.12)$$

In this equation the CRLB for the variance of \hat{Z}_4 is defined as

$$\text{var}(\hat{Z}_4) \geq J(Z_4)^{-1}. \quad (3.13)$$

The first and second derivative of the log likelihood function, Eq. (3.11), respectively are

$$\frac{\partial L(Z_4)}{\partial Z_4} = \sum_m \left[\frac{d(m) \cdot \theta_1}{i_{\text{telescope}}(m)} - \theta_1 \right] \frac{\partial h_{\text{telescope}}(m)}{\partial Z_4}, \text{ and} \quad (3.14)$$

$$\frac{\partial^2 L(Z_4)}{\partial Z_4^2} = \sum_m \left[\frac{d(m) \theta_1}{i_{\text{telescope}}(m)} - \theta_1 \right] \frac{\partial^2 h_{\text{telescope}}(m)}{\partial Z_4^2} - \frac{d(m) \cdot \theta_1}{i_{\text{telescope}}^2(m)} \left[\frac{\partial h_{\text{telescope}}(m)}{\partial Z_4} \right]^2. \quad (3.15)$$

The resulting Fisher information is

$$J(Z_4) = -E \left[\frac{\partial^2 L(Z_4)}{\partial Z_4^2} \right] = \sum_m \left[\frac{\theta_1}{i_{\text{telescope}}(m)} \right] \left[\frac{\partial h_{\text{telescope}}(m)}{\partial Z_4} \right]^2. \quad (3.16)$$

The derivative of the PSF with respect defocus is

$$\frac{\partial h_{\text{telescope}}(m)}{\partial Z_4} = \mathcal{F}^{-1} \left\{ \mathcal{F} \left[\frac{\partial H(m)^*}{\partial Z_4} \cdot H(m) + \frac{\partial H(m)}{\partial Z_4} \cdot H(m)^* \right] \cdot \mathcal{H}_{\text{pixel}}(u_2) \right\}. \quad (3.17)$$

The derivative of the wavefront in the detector plane with respect to (w.r.t) Z_4 is

$$\begin{aligned} \frac{\partial H(m)}{\partial Z_4} &= j \cdot \sum_{u_1} \phi_4(u_1) A(u_1) e^{jZ_4 \phi_4(u_1)} e^{j2\pi m u_1} \\ &= j \cdot \mathcal{F} \left\{ \phi_4(u_1) A(u_1) e^{jZ_4 \phi_4(u_1)} \right\}. \end{aligned} \quad (3.18)$$

Thus, recalling that for arbitrary variables a and b ;

$$j[(a + jb) - (a - jb)] = -2 \cdot b = -2 \cdot \text{Im}(a + jb)$$

leading to the first derivative of the PSF to be

$$\frac{\partial h_{telescope}(m)}{\partial Z_4} = -2 \text{Im} \cdot \mathcal{F}^{-1} \left(\mathcal{F} \left\{ \mathcal{F} \left[\phi_4(u_3) A(u_3) e^{jZ_4 \phi_4(u_3)} \right] \cdot H(m)^* \right\} \cdot \mathcal{H}_{pixel}(u_2) \right), \quad (3.19)$$

where u_3 represents the pupil coordinates. The resulting Fisher information for the optical system containing focus error is

$$J(Z_4) = 4 \sum_m \left(\frac{\theta_1}{i_{Z_4}} \right) \left\{ \mathcal{F}^{-1} \left[\mathcal{F} \left(\text{Im} \left\{ \mathcal{F} \left[\phi_4(u_3) \cdot A(u_3) \cdot e^{jZ_4 \phi_4(u_3)} \right] \cdot H(m)^* \right\} \right) \cdot \mathcal{H}_{pixel}(u_2) \right] \right\}^2. \quad (3.20)$$

As discussed in the background chapter, because the SST uses a shutter with an integration time greater than 25 ms, an accepted model for that atmosphere is a long-exposure atmospheric transfer function, which is given by Goodman as [20],

$$\mathcal{H}_{atm}(u_2) = \exp \left\{ -3.44 \left(\frac{\bar{\lambda} \cdot f \cdot u_2}{r_0} \right)^{5/3} \right\}. \quad (3.21)$$

In Eq. (3.21) $\bar{\lambda}$ is the mean wavelength, f is the telescope focal length, and r_0 is the atmospheric seeing parameter. The long exposure PSF is then computed as,

$$h_{long}(m) = \mathcal{F}^{-1} \left[\mathcal{H}_{opt}(u_2) \cdot \mathcal{H}_{pixel}(u_2) \cdot \mathcal{H}_{atm}(u_2) \right]. \quad (3.22)$$

Samples of the three transfer functions are shown in Figure 11 (a-c) to illustrate how the pixels and atmosphere reduce spatial frequency content of the diffraction limited telescope's optical transfer function. The horizontal axis is shown in terms of the spatial frequency, u_2 , divided by the cutoff frequency, u_0 , for the annular telescope pupil function. Reducing the spatial frequency of the optical system causes the PSF to broaden due to the Fourier transform relationship. As the focus error increases, $\mathcal{H}_{opt}(u_2)$ begins to increasingly limit the spatial resolution of the telescope.

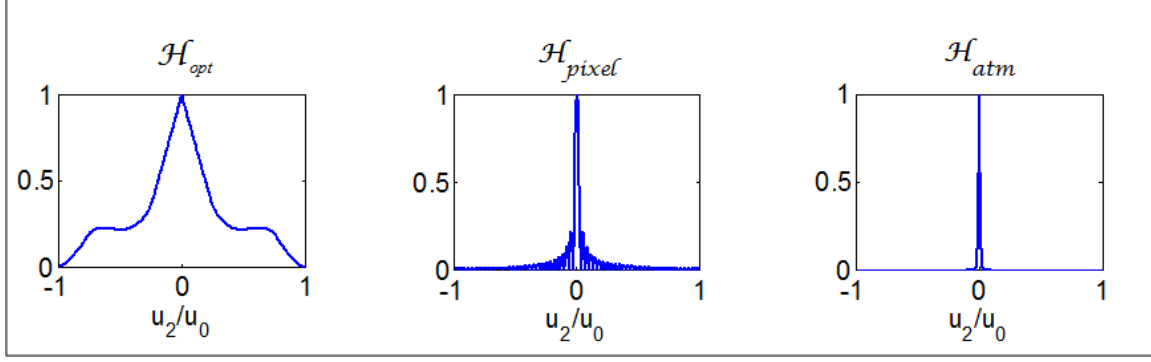


Figure 11. System model transfer function examples. (a) Telescope models optical transfer function (OTF) with $Z_4 = 0$. (b) 15 μm pixels transfer function. (c) Atmospheric transfer function with $r_0 = 8$ cm.

By including the effects of the atmosphere in the PSF, the image intensity model in Eq. (3.9) becomes

$$i_{long}(m) = \sum_x \theta_1 \delta(x) h_{long}(m-x) + B. \quad (3.23)$$

The elements of the Fisher information matrix, I ,

$$I = \begin{bmatrix} J(Z_4) & J(Z_4, r_0) \\ J(Z_4, r_0) & J(r_0) \end{bmatrix} \quad (3.24)$$

are calculated in order to determine the CRLB for variance of \hat{Z}_4 in the presence of an average atmosphere. Using the log likelihood function in Eq. (3.11) and taking the second derivative of Eq. (3.14) w.r.t. r_0 & Z_4 ,

$$\frac{\partial^2 L(Z_4, r_0)}{\partial Z_4 \partial r_0} = \sum_m \left[\frac{d(m) \cdot \theta_1}{i_{long}(m)} - \theta_1 \right] \frac{\partial^2 h_{long}(m)}{\partial Z_4 \partial r_0} - \frac{d(m) \cdot \theta_1}{i_{long}^2(m)} \left[\frac{\partial h_{long}(m)}{\partial Z_4} \right] \left[\frac{\partial h_{long}(m)}{\partial r_0} \right], \quad (3.25)$$

$$\frac{\partial^2 L(Z_4, r_0)}{\partial r_0^2} = \sum_m \left[\frac{d(m) \cdot \theta_1}{i_{long}(m)} - \theta_1 \right] \frac{\partial^2 h_{long}(m)}{\partial r_0^2} - \frac{d(m) \cdot \theta_1}{i_{long}^2(m)} \left[\frac{\partial h_{long}(m)}{\partial r_0} \right]^2, \text{ and} \quad (3.26)$$

$$\frac{\partial^2 L(Z_4, r_0)}{\partial Z_4^2} = \sum_m \left[\frac{d(m) \cdot \theta_1}{i_{long}(m)} - \theta_1 \right] \frac{\partial^2 h_{long}(m)}{\partial Z_4^2} - \frac{d(m) \cdot \theta_1}{i_{long}^2(m)} \left[\frac{\partial h_{long}(m)}{\partial Z_4^2} \right]. \quad (3.27)$$

Because $E[d(m)] = i_{long}(m)$ the elements of the Fisher information matrix are

$$J(Z_4, r_0) = -E \left[\frac{\partial^2 L(Z_4, r_0)}{\partial Z_4 \partial r_0} \right] = \sum_m \left(\frac{\theta_1}{i_{long}} \right) \left[\frac{\partial h_{long}(m)}{\partial Z_4} \right] \left[\frac{\partial h_{long}(m)}{\partial r_0} \right], \quad (3.28)$$

$$J(r_0) = -E \left[\frac{\partial^2 L(Z_4)}{\partial r_0^2} \right] = \sum_m \left(\frac{\theta_1}{i_{long}} \right) \left[\frac{\partial h_{long}(m)}{\partial r_0} \right]^2, \text{ and} \quad (3.29)$$

$$J(Z_4) = -E \left[\frac{\partial^2 L(Z_4)}{\partial Z_4^2} \right] = \sum_m \left(\frac{\theta_1}{i_{long}} \right) \left[\frac{\partial h_{long}(m)}{\partial Z_4} \right]^2. \quad (3.30)$$

Then the derivatives of the PSF are

$$\begin{aligned} \frac{\partial h_{long}(m)}{\partial Z_4} &= \mathcal{F}^{-1} \left\{ \mathcal{F} \left[\frac{\partial H(m)^*}{\partial Z_4} \cdot H(m) + \frac{\partial H(m)}{\partial Z_4} \cdot H(m)^* \right] \cdot \mathcal{H}_{atm}(u_2) \cdot \mathcal{H}_{pixel}(u_2) \right\} \\ &= \mathcal{F}^{-1} \left[\mathcal{F} \left(-2 \text{Im} \left\{ \mathcal{F} \left[\phi_4(u_3) A(u_3) e^{jZ_4 \phi_4(u_3)} \right] H(m)^* \right\} \right) \cdot \mathcal{H}_{atm}(u_2) \cdot \mathcal{H}_{pixel}(u_2) \right], \text{ and} \quad (3.31) \\ \frac{\partial h_{long}(m)}{\partial r_0} &= \frac{5.73}{r_0^{8/3}} \cdot \mathcal{F}^{-1} \left\{ \mathcal{H}_{opt}(u_2) \cdot u_2^{5/3} \cdot \mathcal{H}_{pixel}(u_2) \cdot \mathcal{H}_{atm}(u_2) \right\}. \end{aligned}$$

The CRLB is computed by inverting the Fisher information matrix

$$\begin{bmatrix} \text{var}(\hat{Z}_4) & \text{cov}(\hat{Z}_4, r_0) \\ \text{cov}(\hat{Z}_4, r_0) & \text{var}(r_0) \end{bmatrix} \geq I^{-1}. \quad (3.32)$$

The resulting bound of the standard deviation for estimates of the Zernike coefficient for defocus, $\sigma_{LB}(Z_4, r_0)$ are plotted in Figure 12 for cases with and without an average atmosphere present. Atmospheric turbulence increases the bound and as r_0 decreases, the effect of the atmosphere on the bound increases because a decreasing r_0 represents a more turbulent atmosphere. In addition, as Z_4 decreases the lower bound

increases. Therefore, estimation of Z_4 should become more inaccurate as the amount of defocus decreases.

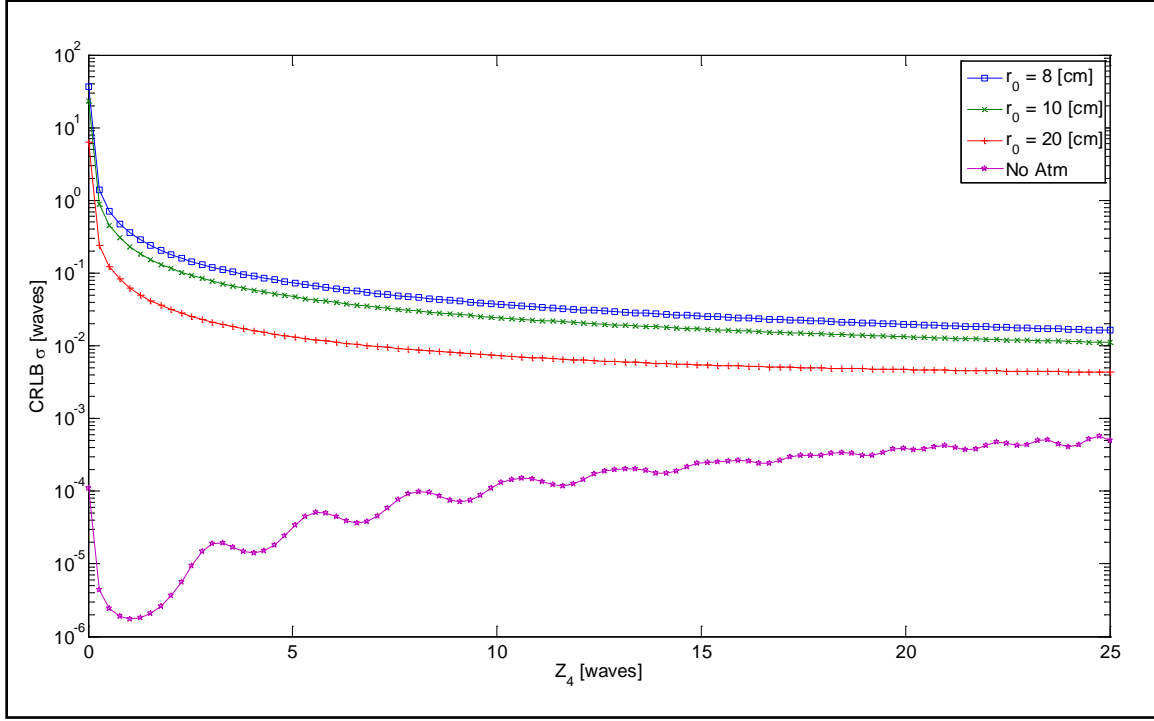


Figure 12. A plot of the CRLB for the standard deviation of the Zernike coefficient for defocus, $\sigma_{LB}(Z_4, r_0)$, for a range of Z_4 values. The standard deviations are shown for cases with no atmosphere in the model and increasing atmospheric seeing by changing r_0 .

3.3 Parameter Estimation

The method of least squares (LS) estimation was used to estimate the Zernike coefficient for defocus, \hat{Z}_4 , from simulated star data. The LS method is used because of computer precision challenges encountered in the maximum likelihood estimation approach, particularly in evaluating the natural logarithm. The primary contribution comes from the large background levels inside the log-likelihood function. To accurately estimate the defocus parameter from the simulated star data, an estimate of the

object's irradiance, $\hat{\theta}_1$, must be calculated from the data by taking the derivative of Eqs.

(3.34) and (3.35) then setting them equal to zero to get the generalized function

$$\hat{\theta}_1 = \frac{\sum_m [d(m) - B] \cdot h(m)}{\sum_m h^2(m)}. \quad (3.33)$$

The intensity models from Eqs. (3.9) and (3.23) are used to define the elements of the sum of squares matrices for the telescope model without an atmosphere,

$Q_{telescope}(Z_4)$, and with an atmosphere, $Q_{long}(Z_4, r_0)$. The elements of each matrix are calculated respectively as

$$Q_{telescope}(Z_4) = \sum_m \left[d_{telescope}(m, Z_4) - \sum_x \hat{\theta}_1 \delta(x) h_{telescope}(x - m) - B \right]^2 \text{ and} \quad (3.34)$$

$$Q_{long}(Z_4, r_0) = \sum_m \left[d_{long}(m, Z_4, r_0) - \sum_x \hat{\theta}_1 \delta(x) h_{long}(x - m) - B \right]^2, \quad (3.35)$$

where, $d_{telescope}(m, Z_4)$ and $d_{long}(m, Z_4, r_0)$ are data from a simulated star and correspond to

a grid formed of possible Z_4 & r_0 values. For the single parameter estimate of Z_4 , a

vector of values of $Q_{telescope}$ are formed with each element in the vector corresponding to

the following range of defocus parameters, $Z_4 = 0, .25, \dots, 29.75, 30$ waves. For the joint

estimation Z_4 and r_0 , a matrix of values of Q_{long} are computed with input parameters

from the sets $Z_4 = 0, .25, \dots, 29.75, 30$ waves and $r_0 = 2, 2.1, \dots, 9.9, 10$ cm. Then \hat{Z}_4 is

determined without accounting for the atmosphere by the single parameter estimate,

$$\hat{Z}_4 = \arg \min_{Z_4} \left(\underline{\underline{Q_{telescope}}} \right), \quad (3.36)$$

or by accounting for the atmosphere with the joint estimator

$$\begin{bmatrix} \hat{Z}_4 \\ \hat{r}_0 \end{bmatrix} = \arg \min_{Z_4, r_0} \left(\underline{\underline{Q_{Long}}} \right). \quad (3.37)$$

By finding \hat{Z}_4 for multiple image frames of simulated star data, the results are then used to determine the sample mean and variance for the LS estimator.

3.4 Phase Retrieval Simulations

Simulated star data, $d_{long}(m)$, viewed through a long exposure atmosphere and defocused telescope are modeled in order to evaluate the performance of the LS phase retrieval technique. Stars are simulated as system impulses, $\delta(x)$, and then the effects of the atmosphere, telescope, defocus, pixilation, background light and star intensity are introduced using Eq. (3.23). The Nyquist sampled images of a star with and without atmospheric effects are shown in Figure 13. (a) & (b) respectively. The pixilated images of those same stars are picture in Figure 13. (c) & (d). Shot noise is simulated in the star data using a Poisson random number generator.

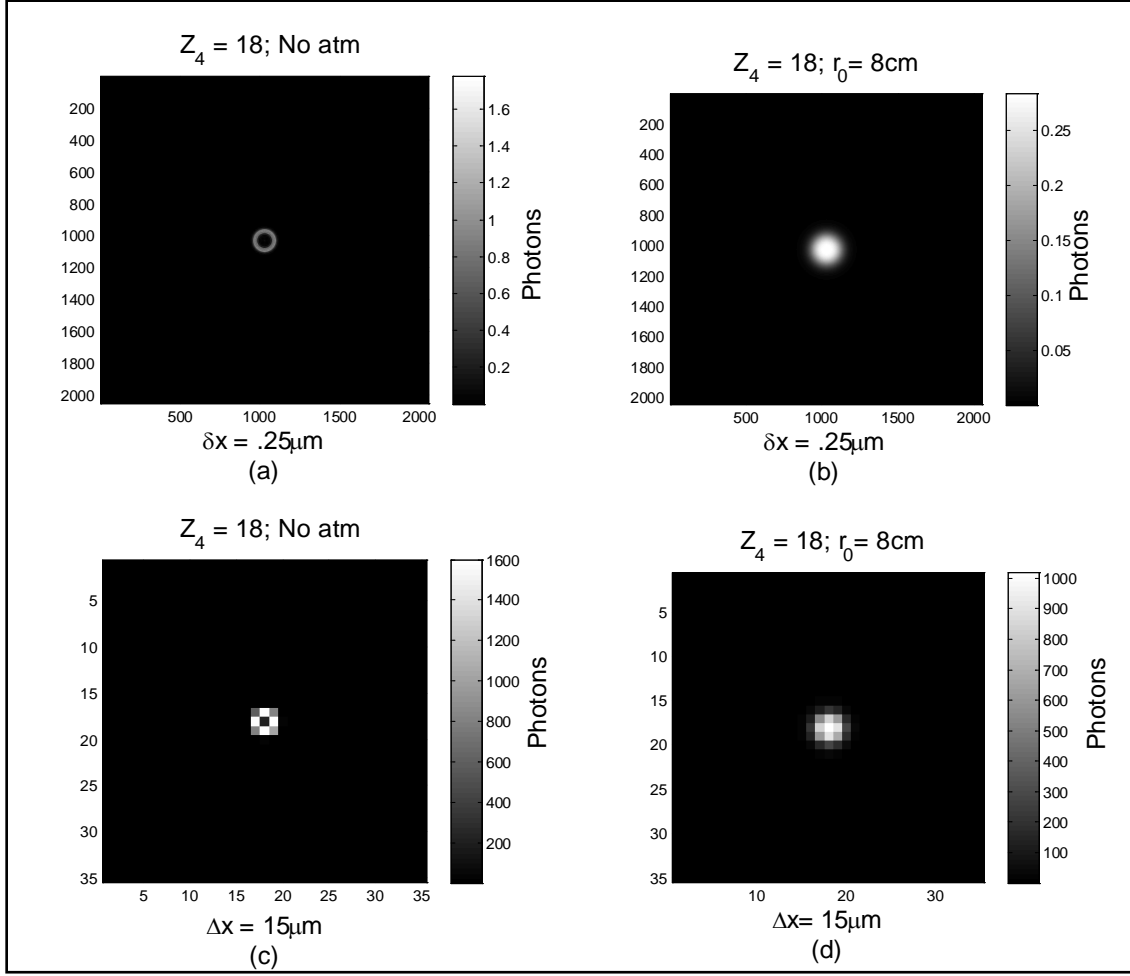


Figure 13. Simulated stars (a) simulated analog image of a star with $Z_4 = 18$ waves and no atmosphere. (b) Simulated analog image of a star with $Z_4 = 18$ waves and an average atmosphere where $r_0 = 8\text{ cm}$ (c) Simulated digital image of a star with $Z_4 = 18$ waves and no atmosphere. (d) Simulated digital image of a star with $Z_4 = 18$ waves and an average atmosphere where $r_0 = 8\text{ cm}$.

To produce the plot in Figure 14, $d_{\text{long}}(m)$ is generated without shot noise and with focus errors ranging from 3-24 waves in order to evaluate the LS estimators biases. Estimates of defocus using Eq. (3.36) are made on simulated stars with and without an average atmosphere present. The graph shows that when the simulated star data does not have an average atmosphere, the single parameter estimator is unbiased. Also, when the average atmosphere is introduced to the data the single parameter estimator has a defocus dependent bias. In contrast, the results of the joint estimator, Eq. (3.37), determined from

the same simulated star data with an average atmosphere present does not have a significant bias.

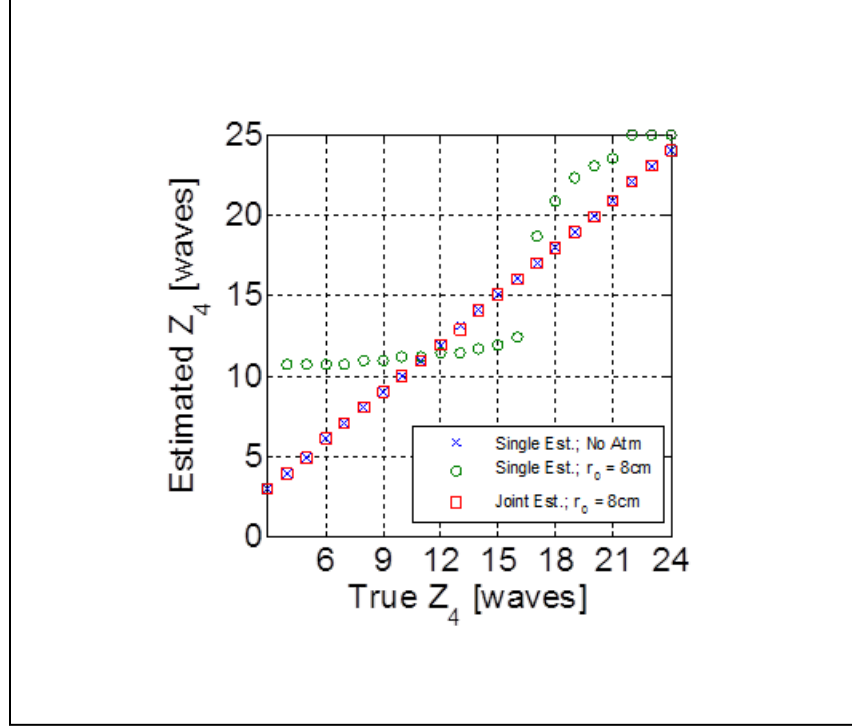


Figure 14. Estimated defocus parameter determined from simulated star data with no noise present to investigate phase retrieval biases. The blue X marks the single parameter estimate for defocus without an atmosphere present in the simulated star data. The green circles are the single parameter estimates of Z_4 where $r_0 = 8$ cm in the simulated star data. The red boxes are the joint parameter estimate of Z_4 where $r_0 = 8$ cm in the simulated star data.

To further evaluate the phase retrieval performance of the LS joint estimator, shot noise is added $d_{long}(m)$ to form multiple frames of simulated star data. Then the estimator's results mean, $E[\hat{Z}_4]$, and standard deviation, σ_s , for each defocus value are plotted in Figure 15. As the amount of defocus in the simulated stars decreases the standard deviation of the estimates increases significantly due to the narrowing of the PSF, measured as the FWHM on the right hand side of the plot. As the PSF narrows, less

of the shape of the PSF can be discerned from the star images increasing the standard deviation of estimates of the defocus parameter.

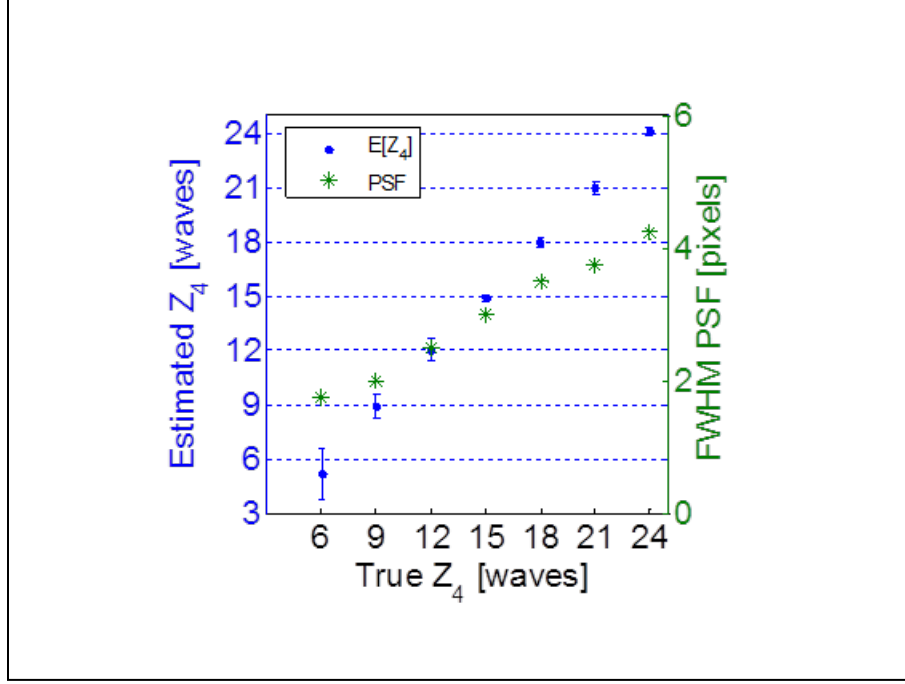


Figure 15. The joint parameter estimates from the simulated stars with shot noise. $E[\hat{Z}_4]$ and σ_s are represented as blue dots and error bars then plotted as a function of the simulated defocus. The FWHM of the PSFs are plotted with the green asterisks as a function of the same simulated defocus.

In Figure 16, the same sample standard deviation, σ_s , from the joint parameter estimates in Figure 15 are plotted along with their associated CRLB, $\sigma_{LB}(Z_4, r_0)$. The $\sigma_{LB}(Z_4, r_0)$ is not achieved by σ_s , but the standard deviation is below a wavelength until the blur spot becomes too small. Overall the joint estimator performs well for phase retrieval of the defocus and seeing parameters because the estimator is unbiased and its variance is manageable since many frames of data can be recorded to reduce the variance to the desired range.

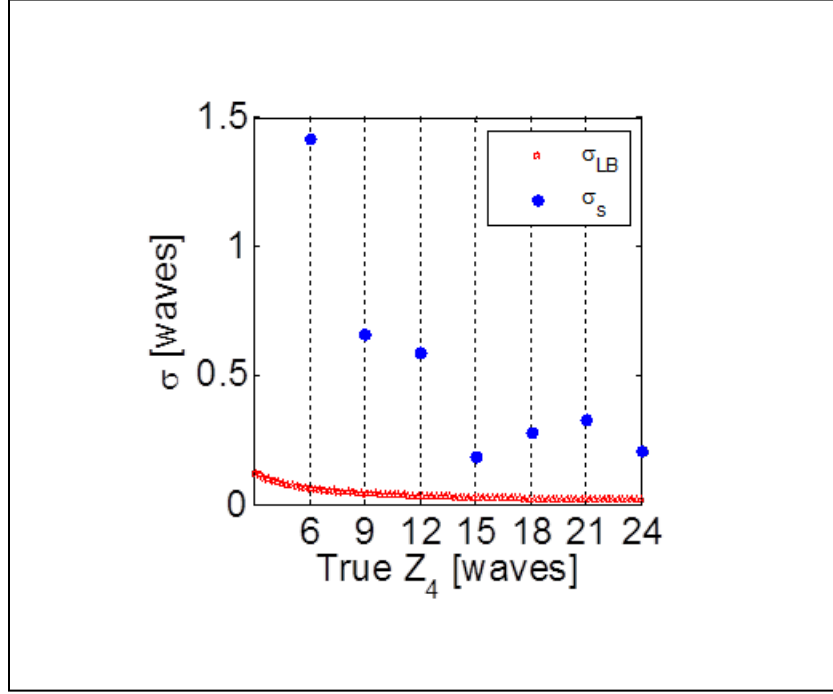


Figure 16. Both the sample standard deviation, σ_s , of the joint parameter estimates (blue dots) and the CRLB, $\sigma_{LB}(Z_4, r_0)$, (red stars) are plotted as a function of simulated star defocus.

3.5 Laboratory Demonstration

A demonstration, illustrated in Figure 17, was conducted to show that the LS estimator for Z_4 and r_0 works beyond the pristine conditions of simulation. The setup includes a point source created with a red LED and a pin hole to create a point source. The light emanating from the pin hole can be considered a spherical wave. The light then propagates to the 2 mm aperture of an intentionally defocused camera. From the single lens forming the aperture, the light is imaged onto a CCD array with a pixel pitch of 16 μm . The data is recorded and the joint estimate of Z_4 and r_0 is made using the LS estimator. The same setup is used for the second half of the demonstration, only this time a thermal source is placed in front of the aperture to simulate a turbulent atmosphere.

The data is recorded and again the joint estimate of Z_4 and r_0 is made using the LS estimator.

The demonstration results are shown at the bottom of Figure 17. On the lower left is the image of the point source without the thermal source. The LS estimate of that blur spot has a $\hat{Z}_4 = .7895$ waves and an $r_0 = 2.27$ cm. Then the blur spot on the lower right is recorded with the thermal source on and the estimates changed to a $\hat{Z}_4 = .4737$ waves and a $r_0 = .018$ cm. While truth data for the defocus and the seeing parameters was not available for this demonstration, the values are consistent with the observed blurring of the point source image. The results from laboratory data are an indication that the LS estimator is working. With the heat source on, r_0 drops below the diameter of the aperture causing a measurable blur in the image of the point source as anticipated.

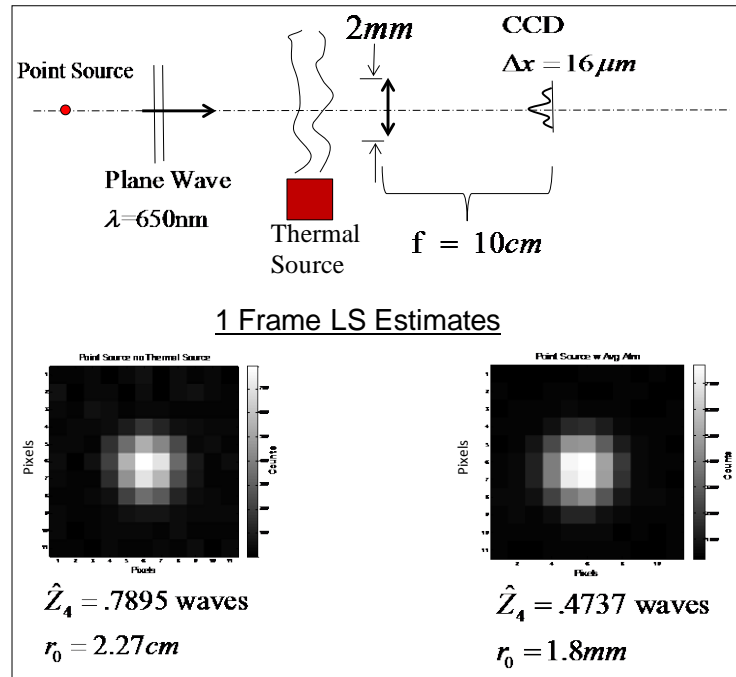


Figure 17. Phase retrieval demonstration setup and results

3.6 Joint Estimation of Spherical Error, Defocus, and Atmospheric Seeing

Ray tracing analysis of the SST optical design predicts it to have spherical error. Therefore, it is important to investigate the effects of the presence of spherical error when estimating the Zernike coefficient for defocus. Once again stars were simulated, however this time the Zernike coefficient for spherical error, Z_{11} , was included in the simulated star data. Then estimates for Z_{11} were made by extending the joint estimator to

$$\begin{bmatrix} \hat{r}_0 \\ \hat{Z}_4 \\ \hat{Z}_{11} \end{bmatrix} = \arg \min_{Z_{11}, Z_4, r_0} \left[\underline{\underline{Q_{long}}} \right]. \quad (3.38)$$

The plot in Figure 18 shows that jointly estimating the atmospheric seeing parameter plus the Zernike coefficients for spherical and defocus produces an unbiased estimate when those aberrations are present in the optical system. However, the omission of either spherical or defocus parameters from the estimate produces a bias estimate for the parameter of interest.

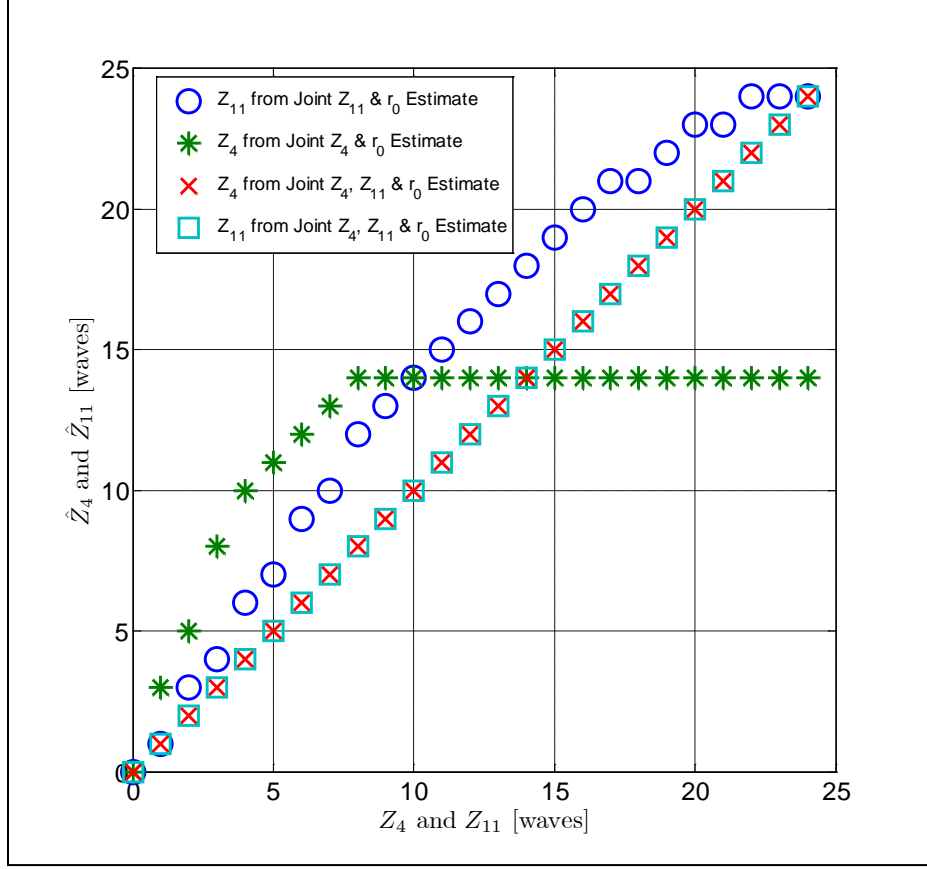


Figure 18. Defocus and spherical error estimation results. Estimated defocus and spherical error parameters determined from simulated star data that has both defocus and spherical aberrations through an average atmosphere with no noise present. The red X marks the joint Z_4 , Z_{11} , r_0 parameter estimate for defocus. The green asterisk are the estimates of Z_4 using only the joint Z_4 , r_0 estimator. The light blue box marks the joint Z_4 , Z_{11} , r_0 parameter estimate for spherical error. The blue circles are the estimates of Z_{11} using only the joint Z_4 , r_0 estimator. The estimator achieves the correct value when all three parameters are jointly estimated.

3.7 Conclusions

Based on the simulations discussed in this chapter, phase retrieval of the atmospheric seeing parameter and Zernike coefficient for defocus can be accurately determined as long as they are jointly estimated. The long exposure atmosphere can affect estimation of Z_4 and Z_{11} thus demonstrating the need to account for r_0 when estimating the SST's aberrations. That being said, ideally an estimator that includes

more Zernike terms would be preferable, so that the optical system can be better optimized and the PSF better characterized. To that end, Chapter V on short exposure imagery demonstrates a phase retrieval method of more Zernike coefficients with a short exposure atmosphere. Unfortunately, the grid search method is too computationally burdensome for the estimation of more coefficients and so a direct search method is used.

In the next chapter, the grid search method presented in this chapter is used for phase retrieval of the defocus and seeing parameters. This method was possible because the SST's other aberrations have been previously estimated using the Donut software, so that they could be included in the PSF model to avoid biasing of the seeing and defocus parameter estimates. The SST's aberrations were phase retrieved with Donut within days of the collection of experimental data so that the PSF was relatively current. By including the other parameters in the PSF model and phase retrieving the atmospheric seeing parameter and defocus parameter that change on a temporal basis, an up-to-date model of the PSF is formed. The PSF model retrieved using this combined parameter estimation technique is used in the MHT and has an advantage over using a star in the FOV for the PSF because the modeled PSF can be shifted without aliasing. However, since the PSF may change over time it would be preferable if all the Zernike coefficients used in the PSF model could be characterized from focused SST data as demonstrated in Chapter V.

IV. Improving Detection using Multi-hypothesis Testing

The mission requirements for the SST differ from typical astronomical telescopes. The SST is designed to scan deep space to detect unknown space objects and correlate their orbits rather than dwell on stellar objects over relatively long periods of time in order to characterize them [3]. In this sense, the SST is a precursor to other wide field of view synoptic search programs like the LSST. Two trajectory matched filter approaches for asteroid detection are described in [23] and [24]; however, these particular approaches are not further investigated in this work. This chapter discusses match filtering the spatial shape of the object in a single observation similar to a correlator or the multi-hypothesis test (MHT).

4.1 Introduction

Currently the SST uses an algorithm developed from a binary hypothesis test (BHT) to detect space objects in a single image [25]. The two hypotheses are 1) the null hypothesis that a space object's image is not in a pixel (H_0) and 2) the alternative hypothesis that the image is in a pixel (H_1). In contrast, a MHT is proposed for single frame detection that selects from the hypotheses that the image is in the center, a corner, or a side of a pixel (H_1 - H_9) in addition to H_0 . Although the use of more hypotheses might increase the detection performance of this scheme, a finite number of hypotheses must be chosen in order to make the use of the test numerically tractable. The results demonstrated using nine alternative positional hypotheses serve to demonstrate the utility of the MHT over a BHT, but do not necessarily represent the optimal performance achievable by a MHT. Since the SST sensor is dominated by readout noise rather than

shot noise at low light levels these tests consider the noise to be Gaussian; however, another method of BHT developed by Pohlig has been derived using a Poisson noise distribution, which is not used for comparison in this study [42].

The experiment conducted as part of this research is designed to determine which type of algorithm is best at detecting dim, unresolvable objects in space on a single frame basis. Since single frame detection decisions are typically used as input to multi-frame detection and tracking algorithms, a superior single frame detector will enhance the performance of any synoptic search telescope looking for NEAs or space debris using this three frame coincidence approach [25]. In order to perform this study, we chose to observe a satellite in GEO that is gradually going into eclipse behind the earth. In this scenario, the unresolvable satellite body experiences an ever decreasing amount of solar illumination, providing a range of intensity values over which to test the performance of different algorithms. Since the presence and location of the satellite is simple to establish when it is brightly lit, all detection algorithms will successfully detect the object before it begins to go into eclipse. The telescope is pointed directly at the satellite and then observes it as it goes into the shadow of the earth. Because the presence of the object is known (and further verified when it emerges from the eclipse) the performance of the different detection algorithms can be ascertained in a controlled environment. Also, because the object is in geosynchronous orbit, it stays relatively stationary in the sky, thus the object requires practically no tracking motion from the telescope motors. With the object location relatively fixed, different detection algorithms are tested using the observations of the dimming satellite. The detection algorithm that successfully reports the presence most consistently through the eclipse period represents the superior

algorithm. This method of testing detection algorithms is far superior to performing algorithm tests against unknown objects that may or may not actually exist, which precludes the possibility of making a firm conclusion as to which algorithm is actually detecting an object with a higher success rate versus a detector that produces more false detections.

Two types of BHTs are compared with the MHT, one is the baseline point detector used by the SST and the other is a matched filter technique (i.e. correlation detector) similar to that used by the Pan-STARRS program [41]. The advantage of a MHT is gained in part by mitigating the aliasing caused by the undersampled SST images [43]. The sufficient statistics for both the BHT and MHT are derived in terms of signal-to-noise ratio (SNR) [25, 38]. The hypothesis that maximizes SNR while simultaneously increasing the probability of detection (P_d) is chosen, thereby providing sub-pixel position information on the image location and increasing P_d over the BHTs.

The comparison of the different hypothesis testing methods on the basis of probability of detection and processing requirements is made using data collected from the experiment described in the next section. A modeled PSF is generated using a phase retrieval technique presented in Section 4.4 and then it is dithered to create the MHT. This PSF model is utilized because it has been proven and documented to work with the SST in the past [17]. In Section 4.6 a comparison of a MHT to the BHTs is conducted to illustrate the advantages of the MHT as well as its additional computational burden. Then at the end of Section 4.6, a derivation shows that the SNR results of the MHT are linearly related to the LS estimates of point source irradiance which improves photometry.

4.2 The SST Experimental Description

As stated in the introduction, the purpose of this experiment is not to find a new object in space using the SST, but to instead run different detection algorithms on data containing a very dim, but known object so that the relative performance of different detection algorithms can be compared in a controlled environment. The experimental method provides a data set that is used to form a clearly supportable conclusion as to what algorithm should be used to help detect dim objects in space. In essence, you cannot measure the probability of detection for a system without knowing with certainty that an object is present to detect. In addition to the experimental description, a basic overview of the SST's design and current detection strategy are covered.

4.2.1 Experimental Setup and Process Overview

The experiment was conducted by imaging a GEO communications satellite, ANIK-F1, with the SST in a test mode as the satellite went into and out of eclipse during the 2012 vernal equinox as illustrated in Figure 19. It was important to conduct the experiment near the equinox because GEO satellites only eclipse during that period of the solar cycle.

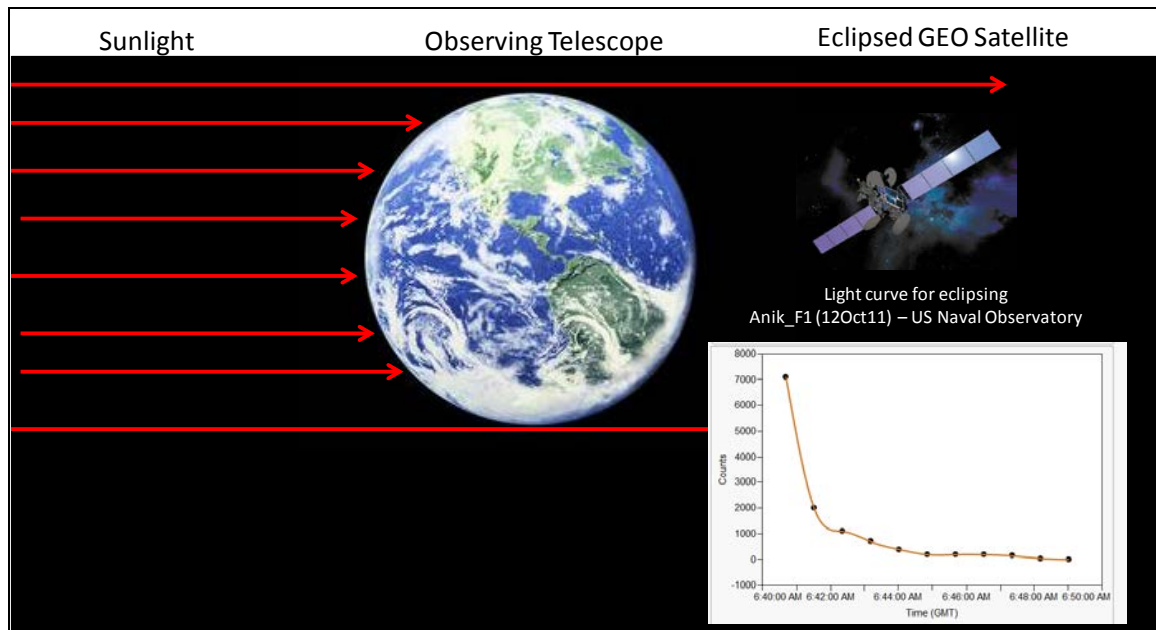


Figure 19. Eclipse experiment overview [41, 42].

There are many cataloged dim astronomical objects which could be used to compare detection algorithm performance, but by imaging eclipsing GEO satellites, the experimental observations capture both the effect of the irradiance division across pixels that arises from objects moving across the FOV of the telescope and the decreasing irradiance levels of the satellites as they enter into eclipse. The irradiance levels decrease as the satellites move through the penumbra and into the umbra as illustrated by the light curve produced from data on ANIK-F1 using the U.S Naval Observatory's (USNO) 1 m telescope and plotted in the lower right hand corner of Figure 19. The roll off of ANIK-F1's irradiance during eclipse was first documented in a series of experiments conducted by USNO to record the glint of GEO satellites shortly before eclipse [50].

The first stage in the experiment is the collection of the raw data. On each night of the experiment, images of the night sky containing ANIK-F1 were collected using 100ms exposures at a rate of 8 frames per second. The telescope was pointed so that

ANIK-F1 was centered in the field-of-view near the time right before the eclipse. The orbital elements of the satellite were entered into the SST's tracking system, so that the SST could be programmed to follow the satellite through the eclipse. This required very little tracking movement from the motors as the object being in GEO orbit appears to be stationary in the sky at approximately the same position throughout the data collection. As predicted on many nights of the eclipse, the satellite became too dim to detect with the SST's existing detection software (described in the next section). Once the data was collected it was recorded and provided to the algorithm test team at AFIT for post-processing.

The next step in the experiment was the pre-processing phase. The raw 6144 by 4096 pixel SST image data was reduced to a more manageable data set involving only 200 by 200 pixels around ANIK-F1. This allowed for more efficient use of memory resources within the computer, while providing a sufficiently large field of view to be certain the satellite was fully contained in the reduced frame as well as capturing nearby stars for use in determining the system PSF. At the beginning of the test ANIK-F1 is bright (roughly a magnitude 9 object) and clearly visible in the center of the field of view of the telescope. Efforts to manually identify its position are further aided by the fact that it doesn't change position appreciably throughout the test. Also, the satellite is readily identifiable when it emerges from the eclipse (again returning to its pre-eclipse magnitude), thus a linear trajectory of the object can be predicted through the eclipse and its exact position (to within a pixel) can be predicted for every frame, thus no other image registration algorithm is required. *A priori* sub-pixel location information is not required

to perform the experiment as all existing tests are designed to make a simple binary decision of whether the object is within the pixel or not.

The next step in the experiment is to extract the point spread function from the images for use by the different detectors. Three different detectors are used to process the data from this test for comparison. The first is the point detector (described in the next section), which is currently used by the SST, LINEAR, Pan-STARRS and other deep space object detection programs [26, 41]. This detector does not utilize a point spread function since it analyzes the data just within a single pixel to make detection decisions. The second detector is the correlator or matched filter detector. This detector is used optionally by the Pan-STARRS program to make detection decisions and requires the use of a PSF [41]. As shown in Figure 20, a star is selected to provide the PSF shape for the correlator on each night. The selected star is chosen to match the shape of the satellite observed near the start of the test in order to help maximize the performance of the correlator. The correlator as implemented by the Pan-STARRS program is not designed to consider undersampling or sub-pixel motion, so a single empirically measured PSF is used each night to implement this particular detector.

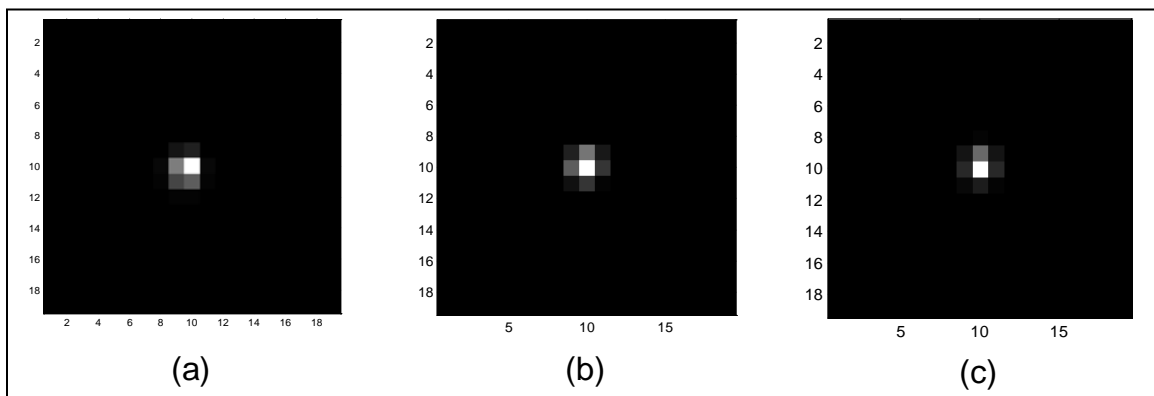


Figure 20. Images of stars used for correlator on (a) 2012 March 13, (b) 2012 March 14, (c) 2012 March 15.

The PSF model used for the MHT requires a properly sampled PSF that can be used to generate the PSF shape for the nine different hypotheses used in the test corresponding to the nine different sub-pixel locations. This was done using a model-based approach. This same optical model was used by the MIT Lincoln labs team to measure the PSF in order to achieve focus and alignment of the telescope in March of 2012 just preceding the eclipse event. The same optical model is used for characterizing the PSF in hopes of leveraging their experience with the telescope to compute the PSF [4]. Although other methods for computing a properly sampled PSF from undersampled imagery exist, performing a comparison study between these methods was not the purpose of this paper [51, 52, 53, 54, 55]. Clearly, a better PSF estimate would lead to even better performance for the MHT method since it is the only detector tested in this study that utilized of a properly sampled PSF. The detailed steps on how the modeled PSF used to construct the MHT is computed are described in Section 4.6.

The final step in the test is to provide each detector with the raw image data in a 19 by 19 window centered on the pixel containing the satellite for all frames of data gathered by the SST of the satellite. Each detector reports an SNR for the satellite for each frame of data. The SNR values over 10 frames are locally averaged to reduce the effect of noise. The averaged SNR is then converted to a probability of detection for the point detector, the correlator and the MHT via the Eqs. (2.34), (2.35), and (4.20) respectively. Although a detection decision could be made based on the reported SNR for each detector in each frame, the computed probability of detection reflects the statistical chance of making a correct detection decision for the object based on the average SNR and the estimated noise level present in the data. The computed probability

of detection is a superior performance metric to SNR or empirical detection frequency because it conveys the improvement of one detector over another in terms that can be more readily understood. Results of the reported probability of detection for each detector on each night are reported in Section 4.7 of this chapter.

4.2.2 The SST System

The SST has a Mersenne-Schmidt design selected for both its wide FOV and compactness [13]. The 3.5 m diameter primary mirror was built to meet the requirement of detecting small faint objects with relatively short integration times, thereby avoiding streaking of the satellite image across multiple CCD pixels so that the objects are suitably modeled as point sources. Another characteristic of the Mersenne-Schmidt design is a curved focal surface, which allows the SST to better optimize spot size across the field of view and spectral response of the CCD. Consequently, the curved CCD imager and mosaic camera were developed specifically for the telescope [3].

4.2.3 The SST Detection Process

As discussed in the Section 2.4, the SST's baseline detection method is based on the point detection BHT used for Lincoln Near Earth Asteroid Research (LINEAR) conducted at the Experimental Test Site near Socorro, NM. In normal operating mode the CCD's 15 μm pixels are 2 by 2 binned and the array has a 6144 by 4096 binned format. While binning the data increases the SNR and improves detection performance, it also increases the amount of undersampling of the data [43].

4.3 Binary Hypothesis Testing (BHT)

Replacing the baseline BHT with a correlation based BHT improves the SST's detection performance. This method for improving the SST's detection performance is explored by [16] in which a comparison of the SNR of two different binary hypothesis tests, a correlator and a point detector, is made using the ANIK-F1 experimental data. In this comparison, stars in the FOV are used to estimate the total system PSF. Figure 20 (a-c) shows irradiance maps of each star within a 19 by 19 window cropped from the SST images on three consecutive nights and used in the correlation detector. One item to note is that in Figure 20 (b & c) the star appears to have a different shape than the star in Figure 20 (a). The change in apparent shape of the star is due to the images being centered at different sub-pixel locations. If the shape of the object of interest is not the same as the total system PSF used in the correlator, the detection performance will be degraded.

The SST's threshold used for detection during the technical demonstration period is $\gamma = 6$, which inherently sets the probability of false alarm. The probability of false alarm is defined as the chance that a pixel that contains only background light (no object) will produce a detector output that exceeds the threshold value of 6. When objects are not present in the pixel the operations described in Eq. (2.34) and Eq. (2.35) are designed to produce unit variance zero mean Gaussian random variables. Therefore, the probability of false alarms, P_{FA} , per pixel is

$$\begin{aligned}
 P_{FA} &= P(SNR_{Baseline} \geq 6 | H_0) \\
 &= P(SNR_{corr} \geq 6 | H_0) \\
 &= \int_6^{\infty} \frac{1}{\sqrt{2\pi}} e^{-\frac{t^2}{2}} dt = 9.87e-010,
 \end{aligned} \tag{4.1}$$

where $SNR_{Baseline}$ is the output of the point detector, SNR_{corr} is the output of the correlator, and H_0 is the hypothesis that no object is present in the pixel.

4.4 The SST PSF Modeling

The long exposure modeled PSF, $h_L(x)$ centered on a pixel is then computed from Eq. (2.14) where x is the Nyquist pixel coordinates. One important property of the Nyquist sampled PSF is that a sub-pixel shift, Δx , of the model does not significantly change its shape. Modeling the effects of Δx on the image irradiance pattern is necessary because the point source is not always in the center of a pixel. To reproduce the change in irradiance pattern measured by each of the $30\text{ }\mu\text{m}$ pixels in the CCD as a function of Δx , the modeled PSF is down-sampled using the ratio, ς , between the $30\text{ }\mu\text{m}$ pixels and the Nyquist pixels size from Eq. (2.38). The shifted and down-sampled PSF is

$$h_{samp}(m, \Delta x) = \int_{-\infty}^{\infty} h_L(x) \cdot \delta(\varsigma m - x - \varsigma \Delta x) dx, \quad (4.2)$$

thus the sampled irradiance is

$$i_{samp}(m, \Delta x) = \theta \cdot h_{samp}(m, \Delta x) + B, \quad (4.3)$$

where B is the background light, and θ is the total number photons emitted from the object per integration, and m is a integer valued pixel location in the CCD array. To build the PSF model, estimates of the coefficients $Z_5 - Z_{11}$ were made using the Donut algorithm and inserted into the PSF model using Eqs. # (2.3)-(2.6) [17].

The method of LS, described in Chapter III using Eq. (3.37), is used to jointly find \hat{Z}_4 and \hat{r}_0 from a star selected the first frame in the ANIK-F1 experimental data (see Figure 20). A color map of the PSF model generated using a the SST star image on

2012 March 14 with both Nyquist and 30 μm sampling are shown respectively in Figure 21 (a) and (b). In the SST data, $d(m)$, the star image can be centered at any sub-pixel location and the corresponding irradiance pattern changes. By shifting the modeled PSF the changes in the irradiance pattern in the star data can be captured. If the PSF is undersampled spatially, as is the case with the 30 μm detected PSF, the shifted PSF will have aliasing artifacts [43]. Figure 21 (c) depicts the aliasing artifacts produced when the undersampled PSF is shifted using the Fourier transform shift method

$$\nu(m) = \cos(m \cdot \Delta x) + i \sin(m \cdot \Delta x), \text{ and} \quad (4.4)$$

$$h_{\text{shift}}(m, \Delta x) = RE \left[\mathcal{F}^{-1} \left\{ \mathcal{F} \{ h_{\text{samp}}(m) \} \cdot \nu(m) \right\} \right], \quad (4.5)$$

where Δx magnitude of sub-pixel PSF shift such that the modeled irradiance is

$$i_{\text{shift}}(m, \Delta x) = \theta \cdot h_{\text{shift}}(m, \Delta x) + B. \quad (4.6)$$

However, if the Nyquist sampled model is shifted before down sampling to 30 μm using Eq. (4.2) as shown in Figure 21 (d) and (e) the irradiance pattern does not have the same aliasing artifacts as seen in Figure 21 (c).

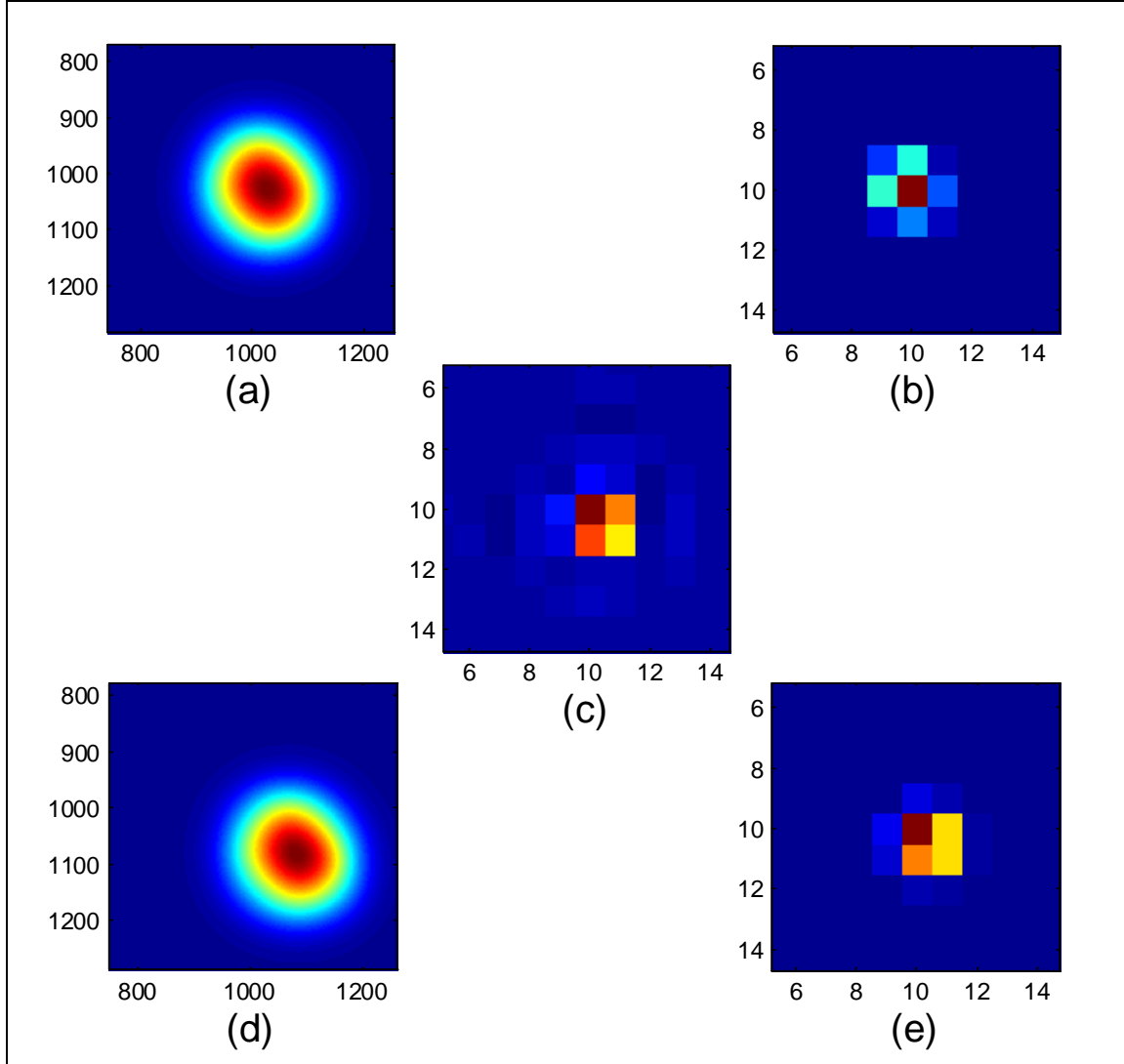


Figure 21. The SST's phase retrieved PSF on 2012 March 14. (a) Centered Nyquist sampled PSF, $a = 2.75 \times 10^{-7}$ m, on a 2048 by 2048 grid (b) Centered down-sampled PSF, $a = 30 \mu\text{m}$, on a 19 by 19 grid (c) Model PSF, $a = 30 \mu\text{m}$, shifted to the lower right hand corner of pixel (10,10) with aliasing artifacts. (d) Nyquist sampled model PSF shifted without aliasing artifacts. (e) Sampled model PSF, $a = 30 \mu\text{m}$, up sampled from Nyquist sampled model PSF shifted to the lower right hand corner of pixel (10,10) without aliasing artifacts.

The accuracy of the sampled irradiance models shifted two different ways can be quantified using the correlation coefficient [56]. The correlation coefficient measures how accurately the modeled irradiance pattern matches the measured irradiance pattern on a scale from zero to one, where a value of one means they are perfectly correlated and

zero means they are uncorrelated. The correlation coefficient between both irradiance models, Eq. (4.6) and Eq. (4.3), and the measured data are computed respectively as

$$\begin{aligned}\rho_{shift}(\Delta x) &= \rho\{d(m), i_{shift}(m, \Delta x)\} \\ &= \frac{\sum_{m=1}^{M_d} \left[(d(m) - B) (\hat{\theta} \cdot h_{shift}(m, \Delta x)) \right]}{\sqrt{\sum_{m=1}^{M_d} (d(m) - B)^2} \sqrt{\sum_{m=1}^{M_d} (\hat{\theta} \cdot h_{shift}(m, \Delta x))^2}}\end{aligned}\quad (4.7)$$

and

$$\begin{aligned}\rho_{samp}(\Delta x) &= \rho\{d(m), i_{samp}(m, \Delta x)\} \\ &= \frac{\sum_{m=1}^{M_d} \left[(d(m) - B) (\hat{\theta} \cdot h_{samp}(m, \Delta x)) \right]}{\sqrt{\sum_{m=1}^{M_d} (d(m) - B)^2} \sqrt{\sum_{m=1}^{M_d} (\hat{\theta} \cdot h_{samp}(m, \Delta x))^2}}.\end{aligned}\quad (4.8)$$

Figure 22 is a plot of the maximum values of $\rho_{shift}(\Delta x)$ and $\rho_{samp}(\Delta x)$ for images of ANIK-F1 on 2012 March 14 as its irradiance is split between pixels. As ANIK-F1's irradiance moves between pixels, even though $i_{shift}(m, \Delta x)$ is shifted to maximize the correlation coefficient, the $\rho_{shift}(\Delta x)$ goes down. In contrast, the maximum value of $\rho_{samp}(\Delta x)$ is relatively constant regardless of where in the pixel the irradiance of ANIK-F1 is located, thus illustrating the importance generating a Nyquist sampled model. In addition, the strong correlation between the modeled PSF and the data indicates that the model is an accurate representation of the SST PSF.

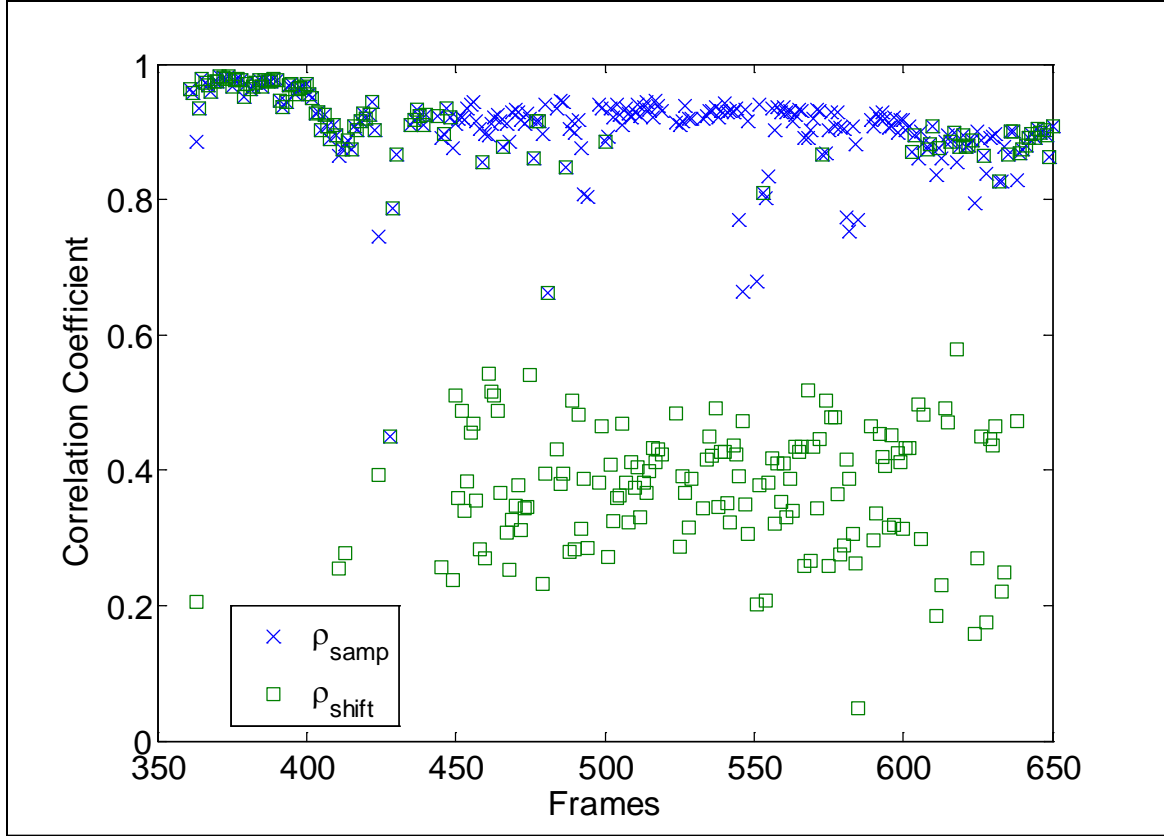


Figure 22. Correlation between two different irradiance models and the images of ANIK-F1 on 2012 March 14 as its irradiance is split between pixels. One model is shifted on the undersampled grid, $\rho_{\text{shift}}(\Delta x)$, and the other on a Nyquist grid and then down sampled, $\rho_{\text{samp}}(\Delta x)$.

4.5 Data Normalization Using Outlier Rejection Techniques

Another feature of the proposed algorithm design is that background noise statistics are computed using a reduced set of data from the window around the pixel to be tested. This new noise power estimation technique has the feature that it rejects any noise sample in the window surrounding the pixel to be tested, whose values do not conform to those predicted by Gaussian statistics. In this way, bad pixels and nearby stars are not used to compute the noise generated by the background light. Current algorithms used by the SST and LINEAR use all the pixels in the window surrounding

the point to be tested to compute the local noise standard deviation, σ [25]. In this process the background B is computed as in Eq. (2.23). The squared deviations, χ , from the background within the window are computed as

$$\chi(m) = (d(m) - B)^2. \quad (4.9)$$

These squared deviations follow a chi-squared distribution based on the assumed Gaussian nature of the data, d . Since samples size is large ($M_d^2 = 361$) the distribution is symmetric. Therefore, the mean of the squared deviations, M , within the window is found

$$M = E[\chi(m)], \quad (4.10)$$

then the standard deviation, S , of χ is computed:

$$S = \sqrt{E[\chi^2(m)] - E[\chi(m)]^2} \approx \sqrt{\frac{\sum_{m=1}^{M_d} \chi^2(m)}{M_d^2} - M^2}. \quad (4.11)$$

A new noise standard deviation, ζ , is computed from the window using Eq. (2.24) by excluding any pixel, m , in the calculation where $\chi(m) \geq (M + 3 \cdot S)$. The new noise standard deviation is included in the following MHT for improved detection performance by normalizing the data as in Eq. (2.34) by replacing σ with ζ .

4.6 Multi-hypothesis testing (MHT)

A multi-hypothesis (M-ary) detector is introduced because the image of a space object does not always fall in the center of the pixel. In addition, simple correlation operations are not desirable because the shape of the sampled PSF changes depending on

where the object is imaged on the array. In order to account for the possibility that the image is in different places within the detector, we introduce a multi-hypothesis test (MHT) strategy. The hypothesis that an image of a space object is not present in the pixel, H_0 , plus the nine different sampled PSF shapes, shown in Figure 23 form the ten hypotheses for the MHT, $\{H_0, H_1, \dots, H_9\}$. This choice of hypotheses captures a great deal of the spatial dependence of the PSF while only introducing one order of magnitude more computations.

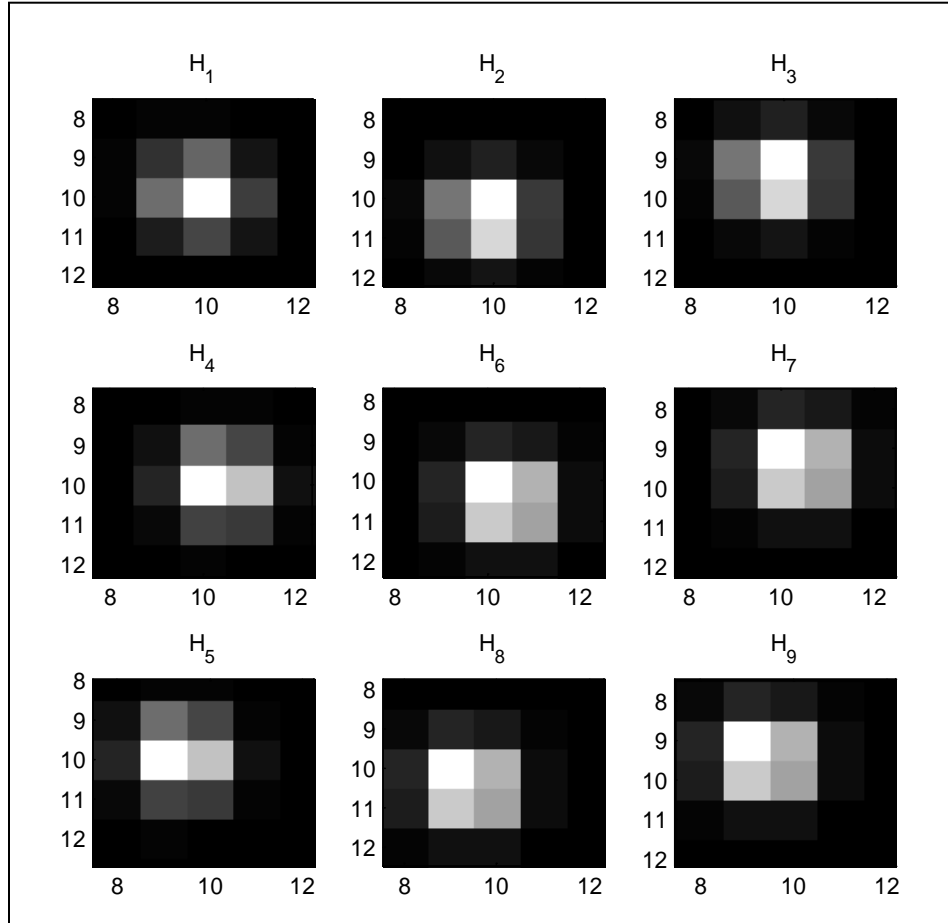


Figure 23. Hypothesis that the point source image is in either the center of the pixel, H_1 , on the sides, H_2 - H_5 , or corner of a pixel, H_6 - H_9 .

According to Kay, the M-ary decision to select one hypothesis, H_k , over another hypothesis, H_i , is the M-ary maximum likelihood (ML) decision rule. Kay derives the ML decision rule using a Bayes risk, R , approach under the assumption of uniform cost and equal priors to decided between the different hypotheses $\{H_0, H_1, \dots, H_9\}$. He assigns cost, C_{ik} to the decision if H_i is selected when H_k is true. The risk is calculated as

$$R = \sum_{i=0}^9 \sum_{j=0}^9 C_{ik} p(H_i | H_k) p(H_k), \quad (4.12)$$

where

$$C_{ik} = \begin{cases} 0 & i = k \\ 1 & i \neq k \end{cases}. \quad (4.13)$$

By assuming uniform cost, each of the hypotheses is given the same priority. With this choice of cost, the information provided on position of the object in the pixel is weighted the same as the binary decision of whether an object is detected or not in the MHT. The position information from the MHT is important for improving the SST's metric accuracy over the BHT. However, detection is more important than position accuracy and this choice of cost could reduce the MHT's detection performance. Even with this penalty in detection performance, the MHT will be shown to still outperform the correlator and the baseline detector in terms of probability of detection. In addition, by making this choice of cost, the derivation of the detector's sufficient statistic is greatly simplified and likely produces a detector that is more computationally efficient to apply.

Kay shows that to minimize R , the hypothesis that minimizes the average cost of deciding H_i if $d(w, z)$ is observed, $C_i(d(w, z))$, should be selected where

$$C_i(d(w, z)) = \sum_{k=0}^9 C_{ik} p(H_k | d(w, z)), \quad (4.14)$$

for $i = 0, 1, \dots, 9$. Inserting Eq. (4.13) into Eq. (4.14)

$$\begin{aligned} C_i(d(w, z)) &= \sum_{\substack{k=0 \\ k \neq i}}^9 p(H_k | d(w, z)) \\ &= \sum_{k=0}^9 p(H_k | d(w, z)) - p(H_i | d(w, z)). \end{aligned} \quad (4.15)$$

Since $p(H_k | d(w, z))$ is not a function of i the risk is minimized by maximizing

$p(H_i | d(w, z))$. Therefore the minimum risk decision rule is choose H_k if,

$$p(H_k | d(w, z)) > p(H_i | d(w, z)) \quad \forall i \neq k. \quad (4.16)$$

Then for equal priors probabilities,

$$\begin{aligned} p(H_i | d(w, z)) &= \frac{p(d(w, z) | H_i) p(H_i)}{p(d(w, z))} \\ &= \frac{p(d(w, z) | H_i) \frac{1}{10}}{p(d(w, z))}, \end{aligned} \quad (4.17)$$

so maximizing $p(d(w, z) | H_i)$ maximizes $p(H_i | d(w, z))$ and the ML decision rule

becomes choose H_k if [38]

$$\Lambda_{G_k} \triangleq \frac{p(d(w, z) | H_k)}{p(d(w, z) | H_0)} > \frac{p(d(w, z) | H_i)}{p(d(w, z) | H_0)} \triangleq \Lambda_{G_i} \quad \forall i \neq k. \quad (4.18)$$

Assuming the prior probability that an object is not in a pixel is equal likely as an object being in the pixel is not a precise choice due to the density of stellar objects. However, the choice of equal priors is chosen because the true probabilities are unknown.

Furthermore, the baseline detector and correlator make this same assumption so the comparison of the MHT to these detectors is a like comparison. As with cost selection, a

better choice in priors could result in a better performing detector, but choices of uniform cost and equal priors are shown to produce a MHT that outperforms the existing BHT.

Since Eq. (4.18) has the same forms as the LRT given in Eq. (2.25), the sufficient statistic for BHT given in Eq. (2.34) can be applied to the MHT accounting for the additional hypotheses based on sub-pixel position shifts listed in Table 1, α_i & β_i .

Therefore, the ML decision rule can be determined as a function of SNR for each location, $f(SNR_i)$, so that Eq. (4.18) becomes chose H_k if

$$\Lambda_{G_k} = f(SNR_k) > f(SNR_i) = \Lambda_{G_i} \quad \forall i \neq k. \quad (4.19)$$

where MHT sufficient statistic is

$$SNR_i = \frac{\sum_w \sum_z^{M_d} (d(w, z) - B) h_{smp}(w + c_x - \alpha_i, z + c_y - \beta_i)}{\zeta \cdot \sqrt{\sum_w \sum_z^{M_d} h_{smp}^2(w, z)}} \underset{H_0}{\overset{H_i}{>}} \gamma_{M-ary} \quad (4.20)$$

- H_0 : Hypothesis that no satellite is present.
- H_i : Hypothesis that a satellite is present (see Table 2)

Table 2. Alternative Hypothesis Sub-pixel Shifts (corresponding to Figure 23)

Alternative (i)	Horizontal Shift (α_i)	Vertical Shift(β_i)
1	0	0
2	0	-15 μ m
3	0	15 μ m
4	15 μ m	0
5	-15 μ m	0
6	15 μ m	-15 μ m
7	15 μ m	15 μ m
8	-15 μ m	-15 μ m
9	-15 μ m	15 μ m

Applying a generalized likelihood ratio test (GLRT), PSF shift estimates, $(\hat{\alpha}_i, \hat{\beta}_i)$, are used to determine if there is a detection in the ML location [38]

$$\begin{aligned} \frac{p(d(w, z) | \{H_1, H_2, \dots, H_9\})}{p(d(w, z) | H_0)} &\underset{H_0}{\overset{H_i}{>}} \gamma \\ &= \frac{p(d(w, z) | \{H_i, (\hat{\alpha}_i, \hat{\beta}_i)\})}{p(d(w, z) | H_0)} \underset{H_0}{\overset{H_i}{>}} \gamma, \end{aligned} \quad (4.21)$$

where

$$(\hat{\alpha}_i, \hat{\beta}_i) = \arg \max_{\alpha_i, \beta_i, i=1:9} (d(w, z) | H_i). \quad (4.22)$$

Therefore, the GLRT can be rewritten as

$$\begin{aligned} \max_{i=1:9} \frac{p(d(w, z) | H_i)}{p(d(w, z) | H_0)} &\underset{H_0}{\overset{H_i}{>}} \gamma \\ &= \max_{i=1:9} \left[\frac{p(d(w, z) | H_i)}{p(d(w, z) | H_0)} \right] \underset{H_0}{\overset{H_i}{>}} \gamma. \end{aligned} \quad (4.23)$$

With this approach, the M-ary hypothesis, H_{M-ary} , that satisfies the ML decision rule and exceeds the detection threshold, γ_{M-ary} , is determined by finding

$$\max_{i=1:9} (SNR_i) \underset{H_0}{\overset{H_{M-ary}}{>}} \gamma_{M-ary}, \quad (4.24)$$

which provides sub-pixel image location information and detection simultaneously.

An important goal in deriving the MHT is to improve the probability of detection, P_D , without raising the probability of false alarm, P_{FA} . In this case the probability of false alarm is the chance that a pixel with no space object in it will be classified as having one.

In mathematical terms, this is the probability that the SNR output of the detector with no object present will exceed the detection threshold. Computing the false alarm probability is a challenging task and may prove mathematically intractable. Instead we compute an upper bound on the probability of false alarm and then use that upper bound as our estimate of the false alarm probability. This guarantees that the new MHT test will not raise the probability of false alarm over the existing BHT used by the SST and LINEAR.

Extending the MHT, from testing only one pixel for $H_0 - H_9$ to testing each pixel in the frame, results in repeating the same test four times in the corners and two times on the sides of each pixel as depicted in Figure 24. Therefore, to minimize the number of hypothesis tests each pixel only needs to be tested in the center, on one corner and on two sides and the overlap of the grids forms the 9 hypotheses for each pixels. While this technique reduces the MHT's number of computations, it is a slight departure from testing each pixel 9 times because the window statistics around each pixel varies.

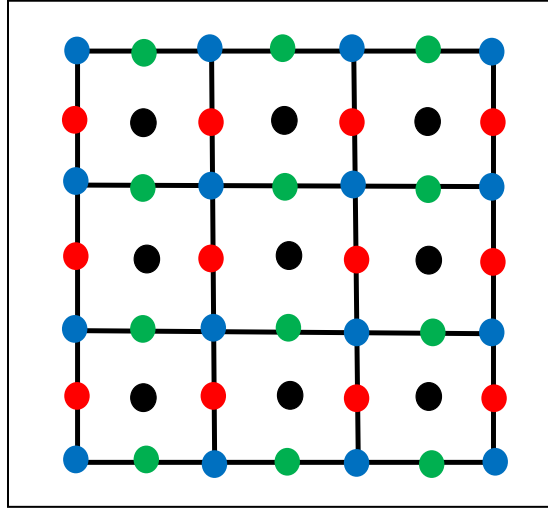


Figure 24. Illustration depicts the overlap of the corners and sides of the pixels on the CCD. (The black dots represent the center of the pixel; the green dot is the corner; blue and red dots are the sides)

Minimizing the number of hypothesis tests, thereby decreasing processing time and P_{FA} .

The MHT computational cost computed in terms of the number of floating point operations (Flops) is ~6 times more than the baseline approach as listed in Table 3.

Table 3. Summary of the Flops required for Each Detector

Parameter	Baseline Flops	Correlator Flops	M-ary Flops
B	M_d^2	M_d^2	$4M_d^2$
σ	$3M_d^2$	$3M_d^2$	$12M_d^2$
SNR	2	$2M_d^2+2$	$8M_d^2+2$
Total Flops	$4M_d^2+2$	$6M_d^2+2$	$24M_d^2+2$

Two simplifying assumptions are made to find the upper bound of the P_{FA} for the M-ary test. The first is considering P_{FA} for each alternative hypothesis of the M-ary test to be mutual exclusive such that $\bigcap_{a=1}^4 H_a = \emptyset$. The second assumption is that the result of each individual alternative in M-ary test is statistically independent of each other. Under those two conditions the P_{FA} can be bounded above by extending Eq. (4.1) to

$$\begin{aligned}
P_{FA} &= P\left(\bigcup_{a=1}^4 H_a \mid H_0\right) - P\left(\bigcap_{a=1}^4 H_a \mid H_0\right) \\
&\leq P\left(\bigcup_{a=1}^4 H_a \mid H_0\right) \\
&= \sum_{a=1}^4 P(H_a \mid H_0) = 4 \cdot P(SNR_{M-ary} \geq 6 \mid H_0) \\
&\approx 4 \times 9.87e-010 = 3.94e-009.
\end{aligned} \tag{4.25}$$

The estimated P_{FA} is higher for the M-ary test than for the BHT, but it can be reduced by raising the M-ary detection threshold to $\gamma_{M-ary} = 6.2212$ so that $P_{FA} \approx 4 \times 2.467e-010 \approx 9.87e-010$.

An example of the detection performance gains from the M-ary test are shown in Figure 25(a-f) using data from the satellite eclipse experiment. To produce the plots, running averages with a 50 frame window for the baseline detector SNR, $\mu_{Baseline}$, the correlator SNR, μ_{corr} , and M-ary test SNR, μ_{M-ary} , were found in the threshold region for all three detectors. The probability of detection for the baseline detector, the correlator, and M-ary test as a function of running average are respectively

$$P_{D_{Baseline}}(\mu_{Baseline}) = \left(\int_6^{\infty} \frac{1}{\sqrt{2\pi}} e^{\frac{-(t-\mu_{Baseline})^2}{2}} dt \right)^3, \quad (4.26)$$

$$P_{D_{corr}}(\mu_{corr}) = \left(\int_6^{\infty} \frac{1}{\sqrt{2\pi}} e^{\frac{-(t-\mu_{corr})^2}{2}} dt \right)^3, \text{ and} \quad (4.27)$$

$$P_{D_{M-ary}}(\mu_{M-ary}) \geq \left(\int_{6.2212}^{\infty} \frac{1}{\sqrt{2\pi}} e^{\frac{-(t-\mu_{M-ary})^2}{2}} dt \right)^3, \quad (4.28)$$

based on the Gaussian noise assumption and the fact that tracklets require three consecutive frames for detection [25]. Note that the threshold in Eq. (4.28) is adjusted to keep the P_{FA} approximately the same for all three detectors.

The probability of detection computed using Eqs. # (4.21), (4.22) and (4.23) are based on the running average SNR output from each detector and represent the average probability of detection that can be expected as the satellites irradiance decreases based on the Gaussian distribution of the noise. In the case of the M-ary test, the running

average is produced using the highest instantaneous SNR output from each of the four alternatives in the M-ary test per pixel, which is selected based on the ML decision rule using Eq. (4.12). In this sense, in terms of detection the results are interpreted as a binary detection solution; either detection occurred in the pixel or it did not. Having a single probability of detection for each CCD pixel tested with the MHT is important so that it can be compared with the BHTs. The other important information resulting from the M-ary test about the sub-pixel location necessary for improving the SST's metric accuracy is not included in the calculation. In addition, the fact four tests are done at each pixel producing SNR values that each may exceed the detection threshold is not factored into the $P_{D_{M-ary}}(\mu_{M-ary})$ calculation. Including the additional test results in the calculation would only serve to raise the probability of detection of the M-ary test because each of the additional hypotheses could also result in the detection of the object. Therefore, Eq. (4.23) only provides the lower bound estimate of probability of detection for the M-ary test.

When ANIK-F1's irradiance is high, all three detectors can detect the satellite, but as the satellite dims as it enters eclipse the detector perform differently. Eventually, the satellite becomes so dim that it is undetectable by any of the detectors. The area of interest then becomes the detection threshold hold region. As seen in Figure 25, on all six nights the M-ary detector detection performance significantly exceeds both the correlator and the baseline detector. This means that the M-ary test detects much dimmer objects than the baseline algorithms. The performance gains seen on 2012 Mar 23 are only due to better calculations of the background noise statistics. On that date there was

a narrow total PSF and a lack of aliasing because the SST tracked the object in the same pixel.

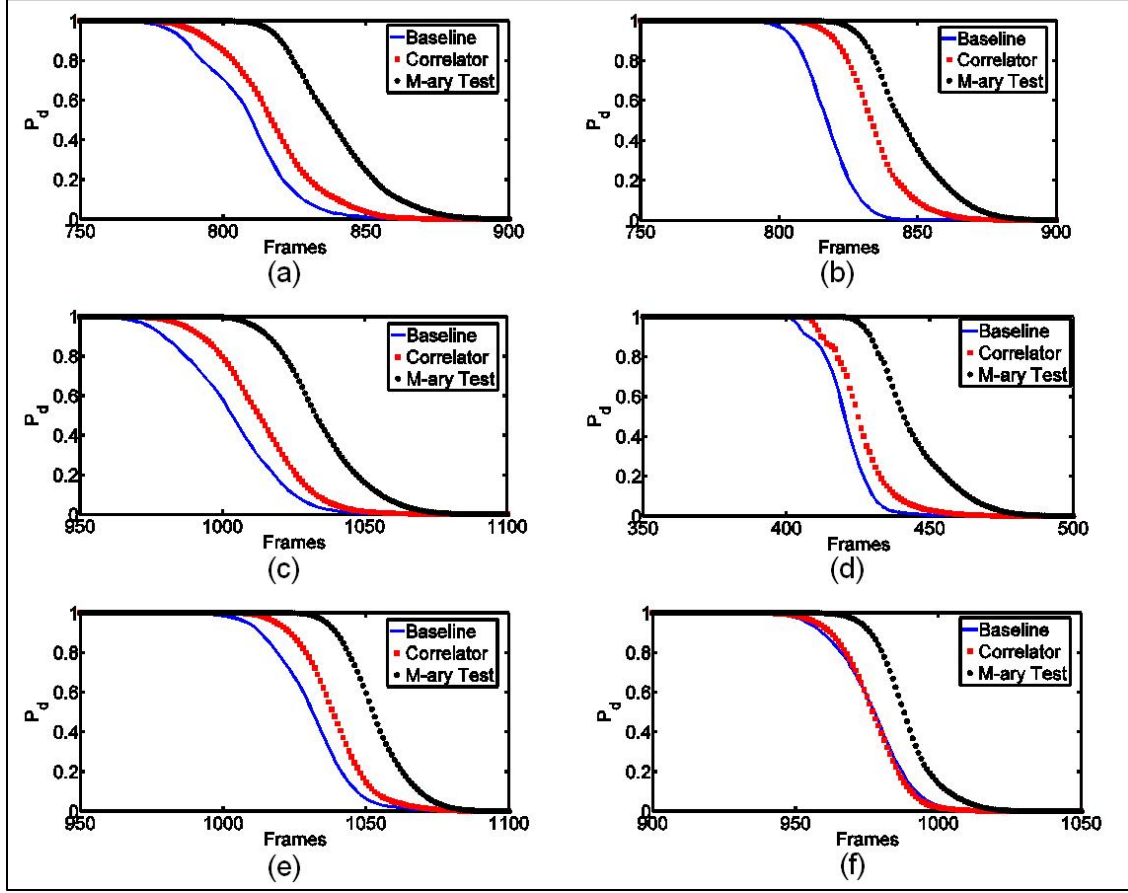


Figure 25. Comparison of the baseline detector, the correlator, and M-ary test probability of detecting (P_d) ANIK-F1 as it enters eclipse on (a) 2012 March 13 (b) 2012 March 14 (c) 2012 March 15 (d) 2012 March 21 (e) 2012 March 22 (f) 2012 March 23 where the P_{FA} is equal for all three detectors.

Using data from six nights of ANIK-F1 eclipse observations, a direct comparison between the baseline detector and both the correlator and M-ary test shows an improved probability of detecting a space object. A plot of $P_{D_{corr}}(\mu_{corr})$ and $P_{D_{M-ary}}(\mu_{M-ary})$ versus $P_{D_{Baseline}}(\mu_{Baseline})$ for the nights of 2012 Mar 13-15 and 2012 March 21-23 is shown in Figure 26. The plot shows that the M-ary test has a higher probability of detection that

the correlator and the baseline detector at the detection threshold. On 2012 March 23, the performance gains were not as dramatic because the objects irradiance was concentrated in one pixel due to excellent tracking of the satellite. However, when the object is not centered on a pixel the M-ary test has a $P_{D_{M-ary}} \approx 1$ when the baseline has only a $P_{D_{Baseline}} = 0.5$. This 30-50% demonstrated improvement in the probability of detection means that significantly more dim objects like small asteroids will be found with the SST using the M-ary detector.

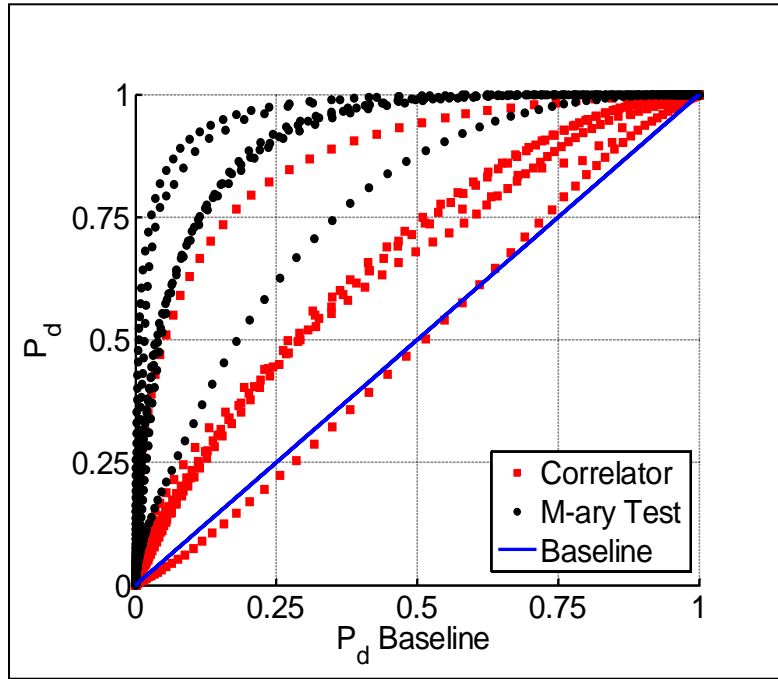


Figure 26. Composite plot of the probability of detecting ANIK-F1 as it enters with either the correlator or M-ary test versus the baseline detector for the nights of 2012 Mar 13-15 and 2012 March 21-23.

In addition to improved detection performance, the M-ary test can also provide better estimates for object irradiance than the baseline detector. The baseline detector estimates are made by adding up the number of digital counts in the pixels where the

object was detected to estimate the object's irradiance, $\hat{\theta}_{Baseline}$. In contrast, the SNR output of the M-ary test is linearly related to the LS estimate of the objects' irradiance, $\hat{\theta}_{M-ary}$, in terms of digital counts of by substituting Eq. (4.20) into Eq. (3.33)

$$\hat{\theta}_{M-ary} = \frac{SNR_{M-ary} \cdot \zeta}{\sqrt{\sum_m^{M_d} h_{smp}^2(m)}}. \quad (4.29)$$

Figure 27 shows that by using the M-ary test results to estimate the object irradiance a much higher digital count is determined because it is counting information across the 19 by 19 window weighted by the PSF rather than only the pixels exceeding threshold. Estimating the digital count more accurately should improve the SST's photometric fit results, which have been shown to have a higher variance for objects with magnitudes fainter than 18 M_v [3].

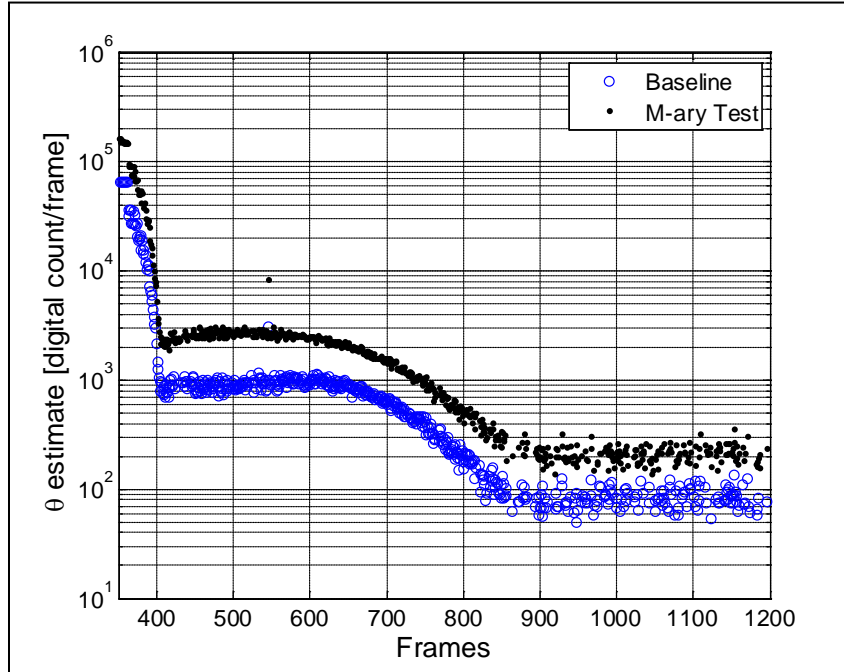


Figure 27. Comparison of the baseline detector and the M-ary test (least squares) estimates of ANIK-F1 irradiance on 2012 March 14 as it enters eclipse.

4.7 Conclusions

A MHT can provide a significant improvement in the SST's detection capability over a BHT when the object is not centered on a single pixel, as shown in Figure 26. Since the SST's mission is to detect unknown space objects, rather than track known objects it is unlikely that any object will repeatedly fall in the center of a pixel during the three consecutive frames used for detection. Recalculating the standard deviation of the background light in the window surrounding the pixel being tested by not including outliers also contributes to the MHT's improved P_d . The gains in detection performance by the MHT are realized by mitigating the aliasing effects of undersampling using phase retrieved PSF model, but come at the cost of a 600% increase in processing power. Simultaneous to detection, the MHT also provides sub-pixel position information and more accurate estimates of object irradiance. These three improvements to the SST's performance by the MHT come with a manageable computational cost that can be afforded with relatively inexpensive modern computers compared to the cost of enhanced optics and therefore give good cause to investigate the implementation of this detector.

V. Phase Retrieval with a Short Exposure Atmosphere

Since the SST is considering a new camera that can do short-exposure imagery, the phase retrieval algorithm described is designed for the primary purpose of diagnostics of an optical system using point source image intensity data (i.e. system impulse response). Two cases are considered first with no atmosphere present and the second with short exposure imagery data. The intended application of this technique is to provide quantitative feedback during the focus and alignment of large three mirror telescopes like the Space Surveillance Telescope (SST), James Webb Space Telescope (JWST), and Large Synoptic Survey Telescope (LSST) [17, 21, 44]. For these telescopes phase aberrations must be recovered using post processing because the focal surface array cannot measure the phase directly.

The primary advantage of this phase retrieval technique over existing phase retrieval techniques is that it converges on the correct set of Zernike coefficients while the telescope is in-focus. For three mirror telescopes this is an important capability since defocusing the telescope requires movement of both the secondary and tertiary mirrors rather than only translating the camera about the focal plane or with the addition of a lens for defocusing [17, 46]. In addition, in-focus phase retrieval would enable optical diagnostics of the telescope using its standard imagery data so the status of alignment could be monitored continually from star data in the field of view (FOV). The new phase retrieval algorithm described in this chapter achieves in-focus phase retrieval by estimating the Zernike coefficients using both an estimated image plane electric field (E-field) and the measured intensity data. Use of the estimated E-field rather than the

estimated phase avoids the problems associated with unwrapping 2-D phase produced by the estimation algorithm.

This chapter is broken up into four sections. The introduction covers the tools used for propagating the field with a Fourier transform of the generalized pupil function, estimating the point spread function (PSF) from point source data, and estimating the electric field with the Gerchberg-Saxton algorithm. Then Section 5.2 demonstrates the advantages of estimating Zernike coefficients with the E-field by comparing the correlation of E-fields and the correlation of intensity patterns produced by different phase aberration. Within this section a new phase retrieval algorithm and its subroutines is described. This section also covers simulations are used to show the performance gains of the new algorithm with a wide variety of phase aberrations compared to the intensity based LS estimation technique used in isolation. Then Section 5.3 covers two laboratory demonstrations that are used to show how the new phase retrieval algorithm performs with measured data. The results support the conclusion that the new algorithm performs well at estimating Zernike coefficients for phase aberration of an optical system in or near focus.

5.1 Introduction

The following background is intended to describe the tools needed for phase retrieval including: how the fields are propagated with a Fourier transform of the generalized pupil function, estimating the point spread function (PSF) from point source data, and estimating the electric field with Gerchberg-Saxton. This summary of techniques provides the fundamental background for understanding how the new phase

retrieval algorithm is implemented. One of the most important techniques is the propagation of the field through a Fourier transform of the generalized pupil function, which is critical for each step in the phase retrieval process. Since the data contains noise, the expectation maximization algorithm described for PSF estimation from the data is a critical input to the new Zernike coefficient estimation technique. The other technique critical for the new in-focus Zernike coefficient phase retrieval algorithm is the estimation of the electric field from the estimated PSF, which is done using Gerchberg-Saxton (GS) phase retrieval.

5.1.1 Generalized Pupil Function

This section is a recap of the description of the generalized pupil function from Chapter II intended to highlight the dependence of the image plane electric field and intensity on the wavefront error, W , in the exit pupil of an optical system. The majority of the wavefront error in an optical system can be decomposed into N -number of Zernike polynomials, $\phi_1 - \phi_N$, represented as

$$W(u_1) = Z_1 \cdot \phi_1(u_1) + \dots + Z_N \cdot \phi_N(u_1), \quad (5.1)$$

where u_1 is a coordinate in the pupil plane and $Z_1 - Z_N$ are the Zernike coefficients [31].

The aberrations can be represented in the generalized pupil function, $\mathcal{P}(u_1)$, as

$$\mathcal{P}(u_1) = A(u_1)e^{jW(u_1)}, \quad (5.2)$$

where $A(u_1)$ is the pupil transmittance function. From the generalized pupil function a model of the electric field as a function of image plane pixel coordinates, m , and wavefront error, $H(m, W)$, is computed using a discrete Fourier transform,

$$H(m, W) = \sum_{u_1} P(u_1) e^{j2\pi m u_1} = \mathcal{F}[P(u_1)] \quad (5.3)$$

and the corresponding PSF, $h(m, W)$, is

$$h(m, W) = |H(m, W)|^2 = H(m, W) H(m, W)^* . \quad (5.4)$$

5.1.2 Intensity Model and PSF Estimation

To conduct Gerchberg-Saxton (GS) phase retrieval, an accurate PSF and intensity model must be estimated from the data. In the case of a true point source, as modeled in the simulated data described in the next section, the object is treated as a Kronecker delta function, δ . A point source is not always available and in those cases the object, O , must be deconvolved from the data to estimate the PSF. In addition, the data contains a flat background that must be estimated.

Estimates of the intensity model and PSF are made from the data using an EM algorithm similar to one developed by Schulz [57]. The difference between the data used in Schulz's blind deconvolution and the data used for the following derivation is that the data includes a flat background. The intensity model, I , as a function of pixel coordinates and wavefront error is

$$I(m, W) = \hat{\theta} \cdot h(m, W) + \hat{B}, \quad (5.5)$$

where the estimate of the background, \hat{B} ,

$$\hat{B} = \text{median}[d(m) \forall m \in [1, M_d]], \quad (5.6)$$

is added to the scaled PSF. Then the scale factor, $\hat{\theta}$, is the number of estimated photons in the measured point source

$$\hat{\theta} = \sum_{m=1}^{M_d} [d(m) - \hat{B}], \quad (5.7)$$

and M_d is the number of pixel coordinates in the PSF window [18]. The EM algorithm used to estimate the PSF begins by hypothesizing the data, $d(m)$, to be

$$d(m) = \tilde{d}_1(m) + \tilde{d}_2(m) \quad (5.8)$$

where $\tilde{d}_1(m)$ and $\tilde{d}_2(m)$ are independent Poisson random variables with mean that are a functions of the object intensity, θ ,

$$E[\tilde{d}_1(m)] = \theta \cdot h(m), \quad (5.9)$$

and of the background, B ,

$$E[\tilde{d}_2(m)] = B. \quad (5.10)$$

Since that the hypothesized data sets are assumed to be independent of one another and Poisson distributed, the joint PDF is

$$P(\tilde{d}_1, \tilde{d}_2 \forall m \in 1 : M_d) = \prod_{m=1}^{M_d} \frac{\theta \cdot h(m)^{\tilde{d}_1(m)} e^{-\theta \cdot h(m)}}{\tilde{d}_1(m)!} \frac{B^{\tilde{d}_2(m)} e^{-B}}{\tilde{d}_2(m)!}, \quad (5.11)$$

and the log-likelihood function is

$$\begin{aligned} L(\theta, h(m), B) &= \sum_{m=1}^{M_d} \tilde{d}_1(m) \ln(\theta \cdot h(m)) \\ &\quad - \theta \cdot h(m) - \tilde{d}_2(m) \ln(B) - B. \end{aligned} \quad (5.12)$$

The E-step in the EM algorithm is found to be

$$\begin{aligned} \Theta &= E \left[L(\hat{\theta}, h(m), \hat{B}) \mid d(m), \hat{\theta}, h^{old}(m), \hat{B} \right] - \lambda \sum_{m=1}^{M_d} h(m) \\ &= \sum_{m=1}^{M_d} \frac{\hat{\theta} \cdot h^{old}(m) \cdot d(m)}{\hat{\theta} \cdot h^{old}(m) + \hat{B}} \ln[\hat{\theta} \cdot h(m)] - \hat{\theta} \cdot h(m) \\ &\quad + \frac{\hat{B} \cdot d(m)}{\hat{\theta} \cdot h^{old}(m) + \hat{B}} \ln(\hat{B}) - \hat{B} - \lambda \sum_{m=1}^{M_d} h(m), \end{aligned} \quad (5.13)$$

where λ is a Lagrange multiplier [58]. The Lagrange multiplier is introduced to constrain the estimation of the PSF to sum to a value of one. Then the M-step for the PSF and Lagrange multiplier are found by first by differentiating Θ with respect to $h(m_0)$:

$$\frac{\partial \Theta}{\partial h(m_0)} = \sum_{m=1}^{M_d} \frac{\hat{\theta} \cdot h^{old}(m) \cdot d(m)}{[\hat{\theta} \cdot h^{old}(m) + \hat{B}]} h(m) - \hat{\theta} - \lambda. \quad (5.14)$$

Therefore the PSF update for each pixel, m_0 , is found to be

$$h^{new}(m_0) = \frac{\hat{\theta} \cdot h^{old}(m_0) \cdot d(m_0)}{[\hat{\theta} \cdot h^{old}(m_0) + \hat{B}](\hat{\theta} + \lambda)} \quad (5.15)$$

and the Lagrange multiplier updates to be

$$\lambda^{new} = \sum_{m=1}^{M_d} \frac{\hat{\theta} \cdot h^{old}(m) \cdot d(m)}{[\hat{\theta} \cdot h^{old}(m) + \hat{B}]} - \hat{\theta}, \quad (5.16)$$

since

$$\sum_{m=1}^{M_d} h(m) = 1. \quad (5.17)$$

The EM algorithm is run until the sum of squared error between d and I equals the estimated local noise variance as the sum of d and at that point the PSF is estimated to be

$$\hat{h}(m) = h^{new}(m_0). \quad (5.18)$$

5.2 Direct Search LS vs. E-Field based Estimation

Zernike coefficient estimation algorithms that rely only on gradient descent techniques for minimizing the sum of squared error (SSE) between the modeled and measured intensity patterns have the problem of getting trapped in local minima [35, 59]. A new Zernike coefficient technique introduced in this chapter that maximizes the

correlation between an estimated electric field and a modeled electric field also has the problem of getting trapped in local maxima. However, by using the two Zernike estimation techniques in conjunction, accurate estimates can be found for low order Zernike coefficients (Z_4 - Z_{11}) that correspond to the aberrations that does not suffer from local minima/maxima.

5.2.1 E-Field versus Intensity Pattern Correlation

The direct search LS phase retrieval technique uses a modeled PSF and the measured intensity of a point source to estimate the Zernike coefficients. However, the modeled electric field described in Eq. (5.3) can also be used to estimate Zernike coefficients from estimates of electric field in the detector plane. The advantage of using the electric field to estimate the Zernike coefficients is better understood by quantifying and comparing examples of the pair wise correlation between the electric field patterns with the pair wise correlation of the intensity patterns produced by the Zernike polynomials and corresponding Zernike coefficient shown in Figure 28. In this comparison, the modeled electric field phase is completely known a priori. However, in the new phase retrieval algorithm presented in Section 5.2.4, the electric field is estimated using GS and may not produce an electric field that is as accurate as if was directly measured from the point source. So this demonstration may not predict how well the proposed estimator will work, but instead motivates the design of an algorithm that attempts to use estimated electric fields in addition to intensity patterns for Zernike coefficient estimation.

Examples of the numerical analysis results displayed as surface plots are produced using the Zernike Polynomials for defocus, ϕ_4 , and spherical aberrations, ϕ_{11} . The electric field associated with each scaled Zernike polynomial is produced using Eqs. (5.1)-(5.3) such that

$$H(m, Z_{i,j}) = \mathcal{F} \left\{ A(u_1) \exp \left[j \cdot Z_{i,j} \cdot \phi_{i,j}(u_1) \right] \right\}, \quad (5.19)$$

where $A(u_1)$ is the circular aperture function shown in Figure 28.

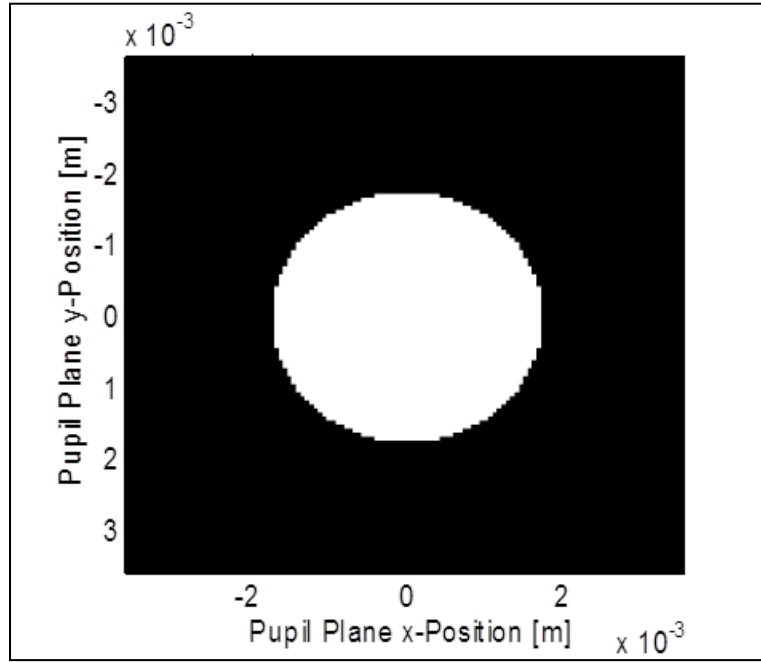


Figure 28. Image of the aperture function, $A(u_1)$, on a 128 by 128 grid for the experimental setup described in this chapter.

Then the pair wise complex correlation coefficient of the electric field pattern in the image plane is computed as

$$\rho_H(Z_i, Z_j) = \frac{RE \left[\sum_{m=1}^{M_d} H(m, Z_i) \cdot H(m, Z_j)^* \right]}{\left(\sum_{m=1}^{M_d} H(m, Z_i) \cdot H(m, Z_i)^* \right)^{1/2} \left(\sum_{m=1}^{M_d} H(m, Z_j) \cdot H(m, Z_j)^* \right)^{1/2}} \quad (5.20)$$

where RE is the real part of the complex value and the pair wise normalized correlation coefficient of the intensity pattern in the image plane as

$$\rho_h(Z_i, Z_j) = \frac{\sum_{m=1}^{M_d} h(m, Z_i) \cdot h(m, Z_j)}{\left(\sum_{m=1}^{M_d} h(m, Z_i)^2 \right)^{1/2} \cdot \left(\sum_{m=1}^{M_d} h(m, Z_j)^2 \right)^{1/2}}. \quad (5.21)$$

The correlation coefficient functions measures the similarity between the patterns on a scale from -1 to 1. A value of 1 indicates perfect correlation, a value of 0 indicates uncorrelated and a value of -1 indicates inverse correlation of the two patterns [56].

Figure 29 (a) illustrates the difficulties in accurately estimating the Zernike coefficient for defocus, Z_4 , in an optical system near focus with only the intensity data due to the high correlation between the intensity patterns produced by different amounts of defocus. In contrast, Figure 29 (b) shows that the E-field pattern produced by defocus is only perfectly correlated with E-field patterns produced by one with equal amount of defocus and the correlation goes down dramatically as a function of the difference in defocus that produces the two E-field patterns. Again in Figure 29 (c) the intensity patterns produced by spherical error and defocus are highly correlated, where as the electric field patterns are significantly less so as shown in Figure 29 (d). The lower correlation between the E-field patterns makes it easier to distinguish between the pattern produced by defocus from the pattern produced by spherical error. The difference in correlation in the E-field space versus the intensity space is considered the reason why the electric field estimates of the Zernike coefficients differ from the intensity based LS phase retrieval estimates. Those differences enable the algorithm described later in this paper that uses both E-field and

intensity estimates of Zernike coefficients iteratively to converge on the correct Zernike coefficients.

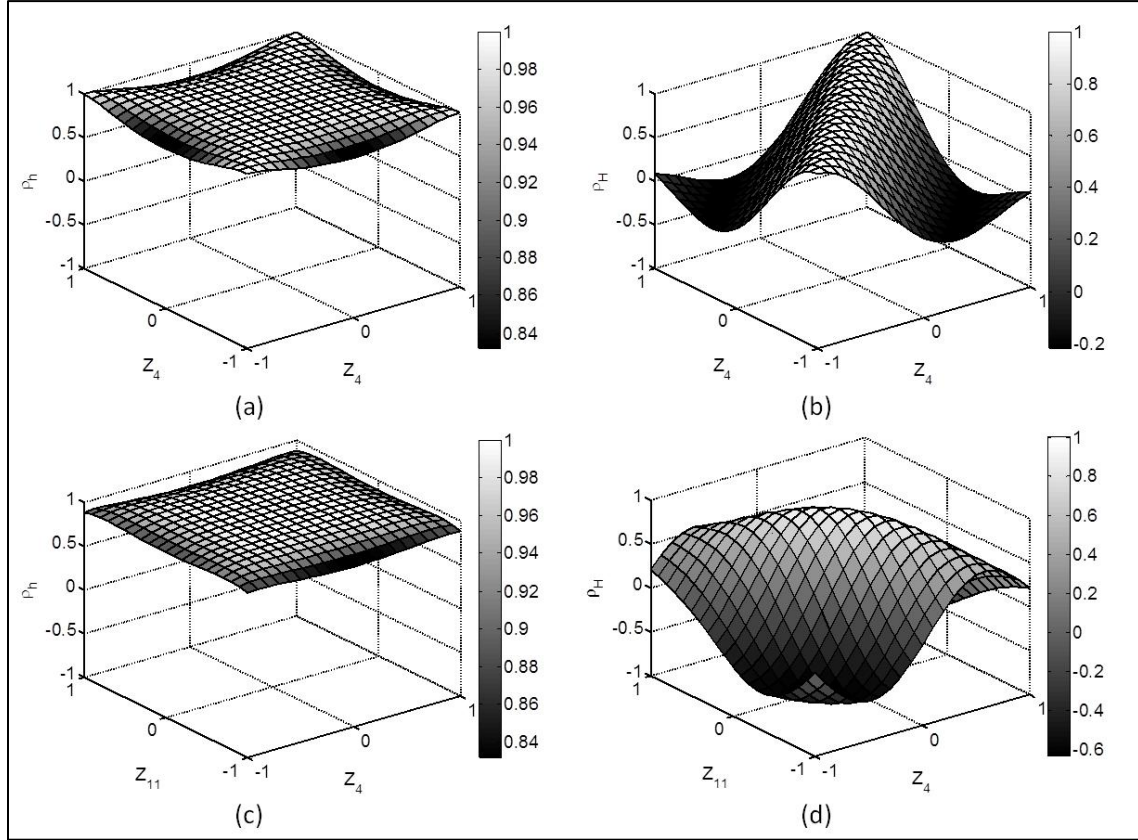


Figure 29. The pair wise correlation between two different (a) intensity patterns, ρ_h , and (b) electric field patterns, ρ_H , produced in the image plane by varying the Zernike coefficients for defocus, Z_4 , independently. The pair wise correlation between two different (c) intensity patterns and (d) electric field patterns produced in the image plane by varying the Zernike coefficient for defocus and spherical error, Z_{11} .

5.2.2 Least Squares Zernike Coefficient Estimation

In theory, intensity LS phase retrieval could be accomplished using a grid search method to estimate the Zernike coefficients, but because of the number of parameters required to form the grid, it becomes computationally challenging [38]. Therefore, direct search or gradient search intensity LS methods are used to estimate the Zernike

coefficients [60]. However, these search methods can become trapped in local minima, but the minima can be escaped by defocusing the optical system [35].

The intensity based LS phase retrieval technique uses the modeled PSF, $h(m, W)$, from Eq. (5.4) and measured intensity data, $d(m)$, of a point source to estimate the Zernike coefficients. The PSF is estimated from the data, $\hat{h}(m)$, using Eq. (5.18) and the model PSF is formed as a function of wavefront error using Eqs. (5.1)-(5.4). Then the sum of squared errors (SSE), Q , between the modeled and the measured intensity is determined by

$$Q[\hat{h}(m), h(m, W)] = \sum_{m=1}^{M_d} [\hat{h}(m) - h(m, W)]^2. \quad (5.22)$$

To minimize the SSE, the intensity LS phase retrieval begins with an initial wavefront, W^{old} , where

$$W^{old}(u_1) = Z_2 \cdot \phi_2(u_1) + \dots + Z_{11} \cdot \phi_{11}(u_1), \quad (5.23)$$

which for the application of focus and alignment of three mirror telescopes can be limited to only Zernike terms 2-11 [17]. The wavefront is adjusted by adding or subtracting scaled Zernike polynomials such that new wavefronts are formed

$$\begin{aligned} W_{2^+}^{New}(u_1) &= W^{old}(u_1) + \Delta_Z \cdot \phi_2(u_1) \\ W_{2^-}^{New}(u_1) &= W^{old}(u_1) - \Delta_Z \cdot \phi_2(u_1) \\ &\vdots \\ W_{11^+}^{New}(u_1) &= W^{old}(u_1) + \Delta_Z \cdot \phi_{11}(u_1) \\ W_{11^-}^{New}(u_1) &= W^{old}(u_1) - \Delta_Z \cdot \phi_{11}(u_1) \end{aligned} \quad (5.24)$$

where Δ_Z is the scale factor that determines how fine of an increment will be searched.

Each new wavefront error results in the following new modeled PSFs

$$\begin{aligned}
h[m, W_{2^+}^{New}(u_1)] &= \left| \mathcal{F} \left\{ A(u_1) \exp[j \cdot W_{2^+}^{New}(u_1)] \right\} \right|^2 \\
h[m, W_{2^-}^{New}(u_1)] &= \left| \mathcal{F} \left\{ A(u_1) \exp[j \cdot W_{2^-}^{New}(u_1)] \right\} \right|^2 \\
&\vdots \\
h[m, W_{11^+}^{New}(u_1)] &= \left| \mathcal{F} \left\{ A(u_1) \exp[j \cdot W_{11^+}^{New}(u_1)] \right\} \right|^2 \\
h[m, W_{11^-}^{New}(u_1)] &= \left| \mathcal{F} \left\{ A(u_1) \exp[j \cdot W_{11^-}^{New}(u_1)] \right\} \right|^2.
\end{aligned} \tag{5.25}$$

The 20 new PSFs in Eqs. (5.25) are each substituted into Eq. (5.22) to form a vector of SSE values

$$\bar{Q} = \begin{bmatrix} Q\{\hat{h}(m), h[m, W_{2^+}^{New}(u_1)]\} \\ Q\{\hat{h}(m), h[m, W_{2^-}^{New}(u_1)]\} \\ \vdots \\ Q\{\hat{h}(m), h[m, W_{11^+}^{New}(u_1)]\} \\ Q\{\hat{h}(m), h[m, W_{11^-}^{New}(u_1)]\} \end{bmatrix}. \tag{5.26}$$

The wavefront error that generates the minimum SSE value in \bar{Q} becomes the initial wavefront error, $W^{old}(u_1)$, for the next iteration and this direct search process continues until the wavefront error reaches local minima [60]. Since the Zernike coefficients are used to form each new wavefront error they are known when the algorithm ends.

5.2.3 E-Field Zernike Coefficient Estimation

The Zernike estimation method using the estimated electric field is very similar to the intensity based least squares method described in the last section. An estimation of the PSF from the data, $\hat{h}(m)$, is input into the GS algorithm to estimate the electric field,

$\hat{H}(m)$, as described in Section 2.2.2. The correlation between $\hat{H}(m)$ and the modeled electric field, $H(m, W)$, is found as

$$\rho(\hat{H}(m), H(m, W)) = \frac{RE \left[\sum_{m=1}^{M_d} \hat{H}(m) \cdot H(m, W)^* \right]}{\left(\sum_{m=1}^{M_d} \hat{H}(m) \cdot \hat{H}(m)^* \right)^{1/2} \left(\sum_{m=1}^{M_d} H(m, W) \cdot H(m, W)^* \right)^{1/2}}. \quad (5.27)$$

Again, the model wavefronts are formed by adding or subtracting scaled Zernike polynomials using Eq. (5.24) and the resulting E-field models are

$$\begin{aligned} H[m, W_{2^+}^{New}(u_1)] &= \mathcal{F} \left\{ A(u_1) \exp[j \cdot W_{2^+}^{New}(u_1)] \right\} \\ H[m, W_{2^-}^{New}(u_1)] &= \mathcal{F} \left\{ A(u_1) \exp[j \cdot W_{2^-}^{New}(u_1)] \right\} \\ &\vdots \\ H[m, W_{11^+}^{New}(u_1)] &= \mathcal{F} \left\{ A(u_1) \exp[j \cdot W_{11^+}^{New}(u_1)] \right\} \\ H[m, W_{11^-}^{New}(u_1)] &= \mathcal{F} \left\{ A(u_1) \exp[j \cdot W_{11^-}^{New}(u_1)] \right\}. \end{aligned} \quad (5.28)$$

The 20 new electric field models from Eqs. (5.28) are each substituted into Eq. (5.27) to form a vector of correlation values

$$\bar{\rho} = \begin{bmatrix} \rho\{\hat{H}(m), H[m, W_{2^+}^{New}(u_1)]\} \\ \rho\{\hat{H}(m), H[m, W_{2^-}^{New}(u_1)]\} \\ \vdots \\ \rho\{\hat{H}(m), H[m, W_{11^+}^{New}(u_1)]\} \\ \rho\{\hat{H}(m), H[m, W_{11^-}^{New}(u_1)]\} \end{bmatrix}. \quad (5.29)$$

The wavefront error that corresponds to the maximum correlation value in $\bar{\rho}$ becomes the initial wavefront error for the next iteration and this direct search process continues until the wavefront error reaches a local maxima. The accuracy of the estimated Zernike coefficients depends on how the algorithm is initialized for two

reasons. The first reason is that the E-field is estimated using GS and not a measured E-field. The second reason is that the method of direct search is used, which can suffer from getting trapped in local maxima. The next section discusses an iterative process that prevents the new E-field based phase retrieval algorithm from estimating the wrong Zernike coefficients by using both the intensity based LS and E-field correlation direct search methods together.

5.2.4 New Phase Retrieval Algorithm

The new phase retrieval algorithm involves an iterative process that includes the E-field estimation from the data, E-field based Zernike coefficient estimation, and direct search LS Zernike coefficient estimation as depicted in Figure 30. The PSF is estimated from a 128 by 128 pixel window of the intensity data using the EM algorithm described in Section 5.1.2 and is input into the GS algorithm to estimate the electric field. The estimated electric field is correlated with the models of the electric field to estimate Zernike coefficient as described in Section 5.2.3. The output coefficients become the initial conditions for the intensity based LS Zernike coefficient estimation detailed in Section 5.2.2. If the SSE value, Q , is not below the set threshold, a new wavefront error is modeled using Eq. (5.1) to reinitialized the GS algorithm. The process is repeated until the SSE is less than 10^{-4} which produces accurate estimates of the Zernike coefficients in simulation and is achieved.

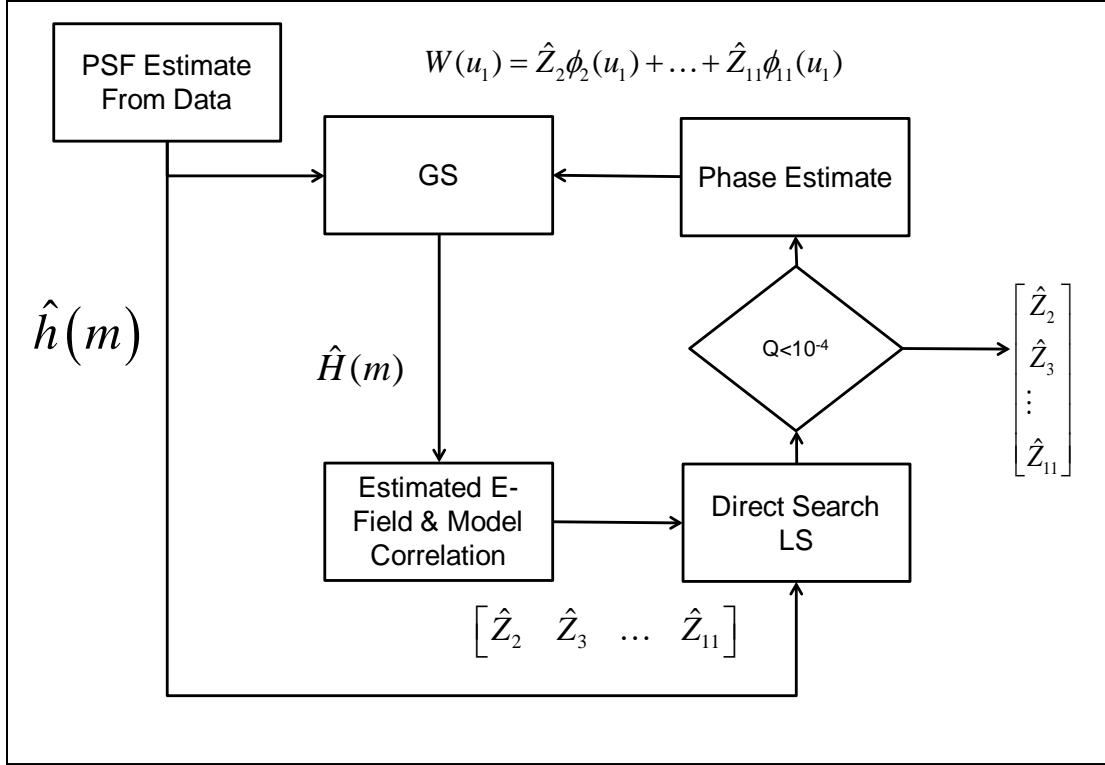


Figure 30. Block diagram new electric field based phase retrieval algorithm for estimating Zernike coefficients.

5.2.5 Phase Retrieval Simulation

A comparison of the performance of the new phase retrieval algorithm and only the intensity based LS subroutine were simulated to illustrate the performance advantages of the new method. The following intensity model is used to simulate data

$$d(m, W) = \theta \cdot h(m, W) + B + n(m), \quad (5.30)$$

where $d(m, W)$ is Poisson distributed, θ is the number of photons in the point source, B is the flat background noise, and $n(m)$ is added noise. From the data, estimates of the point source intensities were made by using Eq. (5.7) and background was found with Eq.(5.6). The EM algorithm then was used to estimate the PSF.

A sample of simulated inputs and outputs of both the new electric field based phase retrieval method and the intensity based LS phase retrieval algorithm are shown in

Figure 31. The input wavefront error, W , shown in Figure 31 (a) was generated setting all the Zernike coefficients Z_4 - Z_{11} equal to one. The simulated data from W is shown in Figure 31 (b) and was generated by adding a 100 photon background, a 10^4 photon source, and shot noise using Eq. (5.30). An image of the phase retrieved model of the electric field, $H(m, W)$ shown in Figure 31 (d), illustrates the how the pattern differs from that of the phase retrieved PSF, $h(m, W)$, shown in Figure 31 (e). A comparison of the phase screens of wavefront error in the pupil in Figure 31 (a), (c), and (f) illustrates the improved accuracy of the new electric field based phase retrieval algorithm over just using the intensity based direct search LS algorithm. Likewise, by comparing the PSF determined with the new electric field based phase retrieval algorithm, Figure 31 (e), and only the intensity based direct search LS algorithm, Figure 31 (g), with the simulated data in Figure 31 (b) it is evident that the new algorithm is performing better by escaping the local minima/maxima.

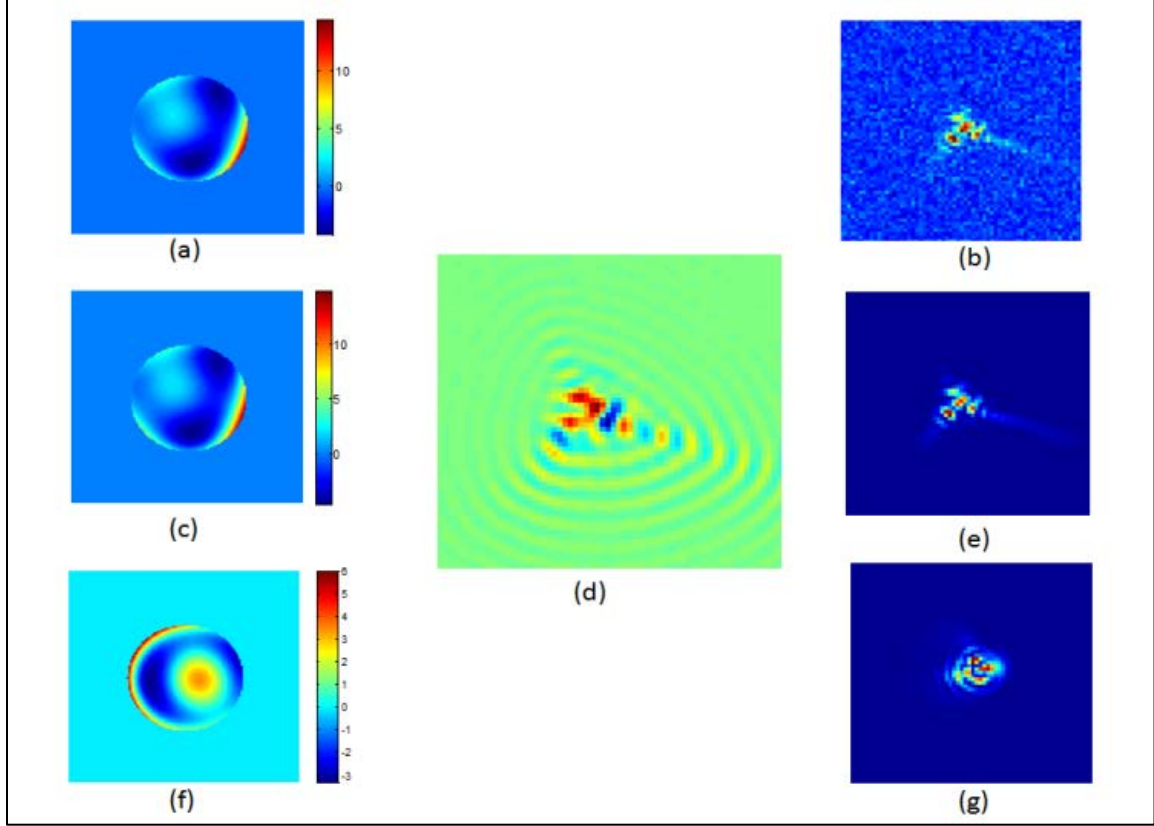


Figure 31. Phase retrieval simulation examples (a) input wavefront in pupil (b) simulated data in image plane (c) estimated wavefront error in pupil using new electric field based phase retrieval algorithm (d) real part of the electric field pattern in image plane determined using new electric field based phase retrieval algorithm (e) PSF in image plane determined using new electric field based phase retrieval algorithm (f) estimated wavefront error in pupil using only the intensity based direct search LS algorithm (g) PSF in image plane determined using only the intensity based direct search LS algorithm.

To evaluate the performance of the phase retrieval algorithm, 100 combinations of random low order Zernike coefficients were used to produce the simulated wavefront error where

$$[Z_2 \quad Z_3 \quad \dots \quad Z_{11}] = \text{unif}(-1,1), \quad (5.31)$$

where the *unif* function is the uniform distribution. Each of the randomly generated wavefront errors has an associated an intensity model that has noise added to produce 100 trials, T , of data using Eq. (5.30). The Zernike coefficients are estimated using both the

intensity based direct search LS algorithm and the new electric field based phase retrieval algorithm starting with the Zernike coefficients initialized to zero. The results of each algorithm's Zernike coefficient estimates, \hat{Z}_i , are plotted in Figure 32 and are in terms of the difference, Δ , between the absolute value input of the known Zernike, Z_i , and the average estimated Zernike coefficients

$$\Delta = \left| Z_i \right| - \left| \frac{\sum_{T=1}^{100} \hat{Z}_i}{100} \right| \text{ where } i \in \{4, \dots, 11\}. \quad (5.32)$$

The mean Δ is computed for all the random combinations, C , of Zernike coefficients used to form the simulated wavefront error

$$\Delta_{Mean} = \frac{\sum_{C=1}^{100} \Delta_C}{100} \quad (5.33)$$

and the standard deviation of Δ is

$$\Delta_{STD} = \left\{ \sum_{C=1}^{100} \left[(\Delta_C - \Delta_{Mean})^2 \right] / 100 \right\}^{1/2}. \quad (5.34)$$

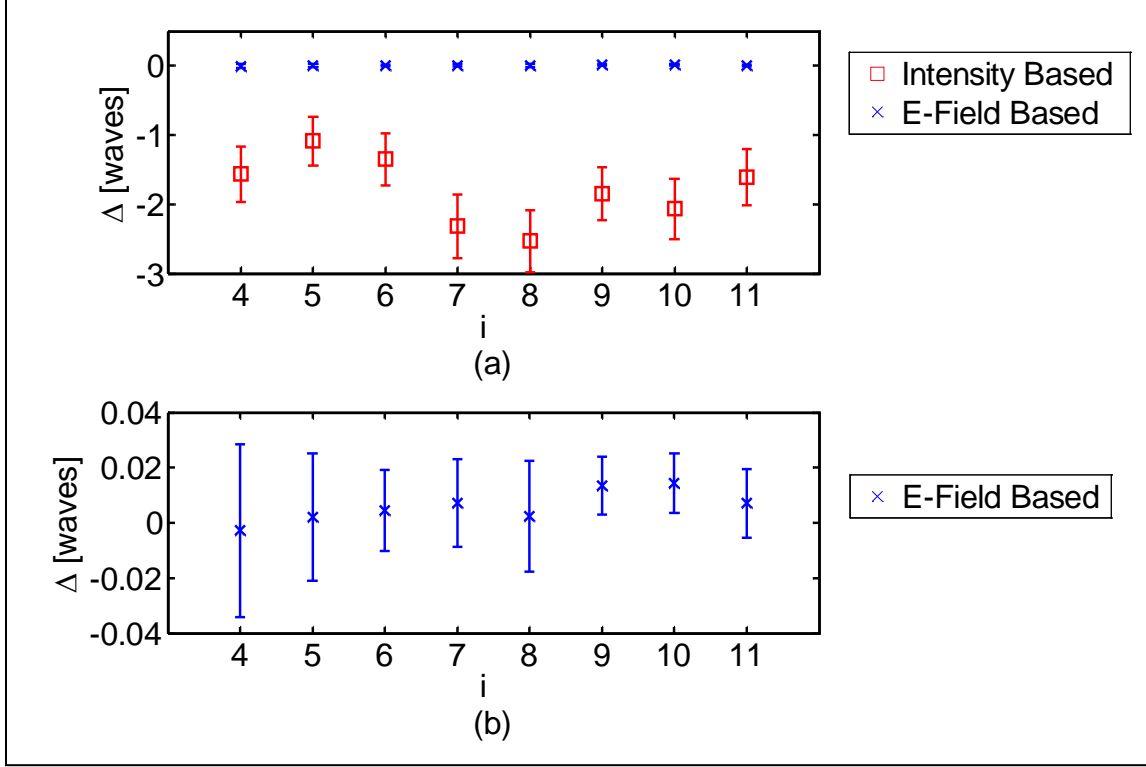


Figure 32. Difference between the Zernike coefficients, Z_i , simulated and phased retrieved using (a) only the intensity based direct search LS algorithm versus new electric field based phase retrieval algorithm and (b) expanded plot of new electric field based phase retrieval algorithm results. The error bars corresponded to the standard deviation of Δ are computed via Eq (5.34).

Using only the intensity based direct search LS algorithm produced the biased estimates of the Zernike coefficients due to the problem of getting trapped in local minima as shown in Figure 32 (a). In contrast, the estimates of the Zernike coefficients using the new electric field based phase retrieval algorithm expanded on the plot in Figure 32 (b) are relatively unbiased because the local minima are avoided due to the iterative process outlined in Section 5.2.4.

5.3 Laboratory Demonstrations

To investigate the performance of the phase retrieval algorithm on measured data two different controlled aberrations were generated in the laboratory. The first was

defocus, which is simple to generate, control and quantify by moving the image plane with respect to the detector. The second was astigmatism generated by tilting the lens with respect to the optic axis which demonstrates performance on another aberration but is more difficult to control.

5.3.1 Defocus

The defocus demonstration used the setup depicted in Figure 33. The object, O , was formed by a LED with a wavelength, λ , of 648 nm illuminating a 200 μm pinhole. The object is imaged by a single lens with a focal length, f , of 17.5 cm. The focused image was formed in image space according to the thin lens equation [5]

$$\frac{1}{f} = \frac{1}{S_i} + \frac{1}{S_o}, \quad (5.35)$$

where S_o is the distance from pin hole to the aperture and S_i is the image location. The aperture is defined by an aperture stop with diameter, D , of 3.62 mm to ensure that the Nyquist sampling was achieved with the 16 μm pixel pitch of the camera's detector.

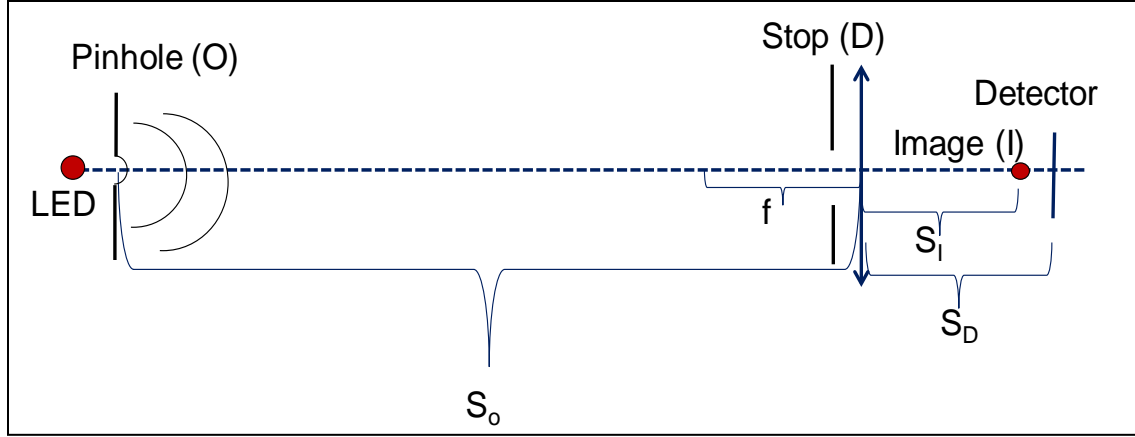


Figure 33. Defocus demonstration setup.

Defocus was generated by shifting the lens mounted on a translation stage in order to defocus the image by creating a distance between the image location and the detector distance, S_D , from the lens

$$\Delta_{Focus} = S_I - S_D, \quad (5.36)$$

according to Table 4.

Table 4. Defocus Demonstration Parameters

S_o (cm)	S_i (cm)	Δ_{Focus} (cm)
188.2	19.8	-0.5
189.2	19.3	0
190.2	18.8	0.5
191.2	18.3	1
192.2	17.8	1.5

The theoretical wavefront error that was generated from these shifts is computed and decomposed into the Zernike coefficients, Z_2 - Z_{11} [31].

Figure 34 summarizes the results of the defocus demonstration. The first column is the measured shift in the lens, which is equal to the focus. The second column is that intensity data that was recorded by the camera corresponding to the lens position. As expected with more defocus, the data becomes spread out. The PSF column shows the data after it is blind deconvolved from the pin hole object to produce the PSF, since the pinhole was not small enough to represent a true point source [16]. The blind deconvolution is achieved through a two-step process. First the blurred image of the pinhole is estimated using the EM algorithm presented in Section 5.1.2. This has the effect of producing a background removed image of the pinhole convolved with the point spread function. Then Schulz's blind deconvolution algorithm (BDA) estimated the pinhole shape and the point spread function. A circular function is used to initialize the image estimate and phase function and two waves of defocus are used to initialize the field in the pupil. The pupil transmittance function is circular with a diameter of 3.62 mm [57]. An initial estimate of the pinhole size is input into the BDA, in terms of the number of pixels in object space, along with the normalized data output from the EM algorithm. The BDA is run for 100 iterations in which it converges on a stable estimate of the size and shape of the pinhole while simultaneously estimating the PSF. Phase retrieval is conducted on the PSF to estimate Zernike coefficients (Z_2 - Z_{11}) and produce the modeled PSF. The estimated coefficient for defocus is listed next to the theoretical value that is computed using the wave optics calculations discussed in the appendix. The small difference between the theoretical value for Z_4 and the estimate are within the

combined error of our lens translation stage accuracy of ~ 1 mm and the estimate error from noise. One important point to note is that only defocus is experimentally generated, but the phase retrieval algorithm attempted to estimate 10 different Zernike coefficients, yet it still correctly attributed the wavefront error to the aberration of defocus.

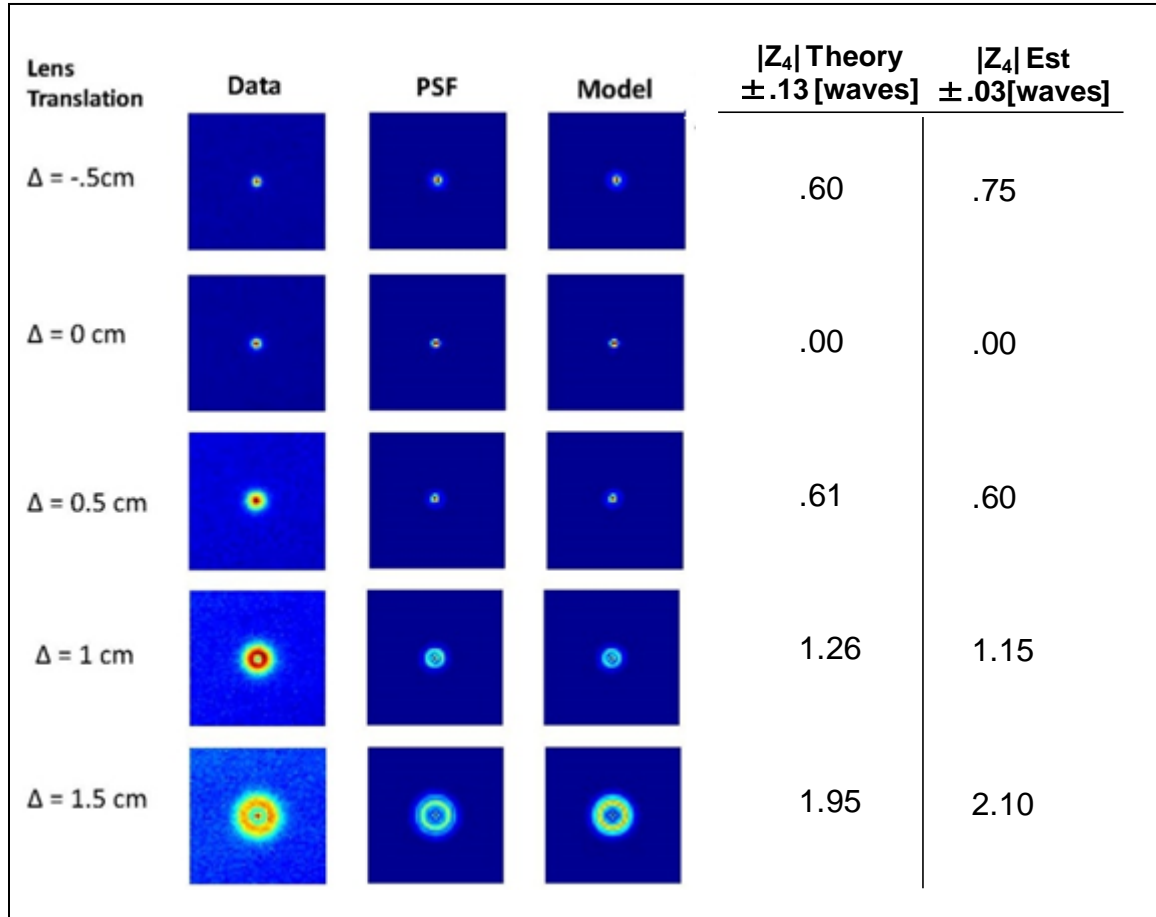


Figure 34. Results of defocus demonstration.

5.3.2 Astigmatism

The Astigmatism demonstration uses the set up depicted in Figure 35. The object, O , is formed with the same pinhole and LED as the defocus demonstration by a lens with

a focal length, f , of 50.0 cm. The camera detector is placed at S_1 and the lens is tilted with respect to the optic axis in order to generate astigmatism.

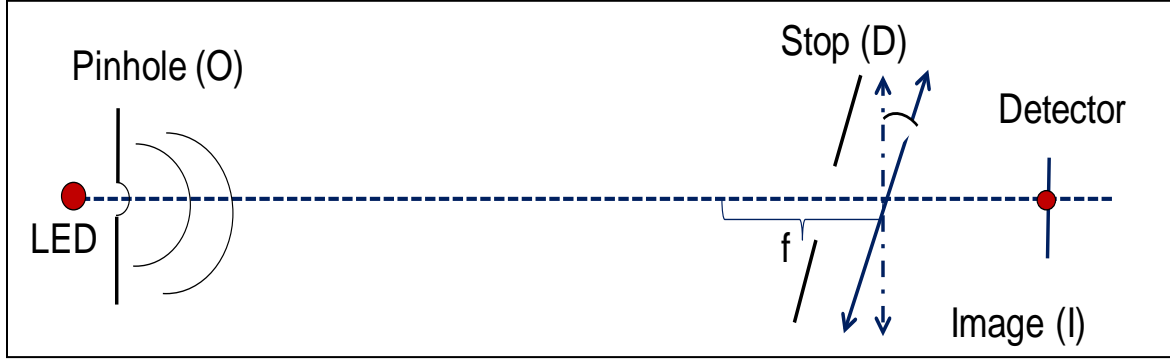


Figure 35. Astigmatism demonstration setup.

Figure 36 shows the results of the astigmatism demonstration. The first column is the camera recorded data taken in and out of focus. The data is processed with the blind deconvolution algorithm to as with the defocus experiment produce the PSF column Figure 36 (b), (e), and (h). Then the Zernike model is phase retrieved from the focused PSF in Figure 36 (b). The Zernike model for the defocus spots in Figure 36 (f) and (i) are formed by using the model terms Z_5 - Z_{11} from the phase retrieval of the focus spot and then fit using Z_2 - Z_4 as free parameters. Comparison of the PSF in Figure 36 (e) and (h) to the modeled PSF in Figure 36 (f) and (i) illustrates that an accurate amount of astigmatism in the optical system is phase retrieved from the focused spot.

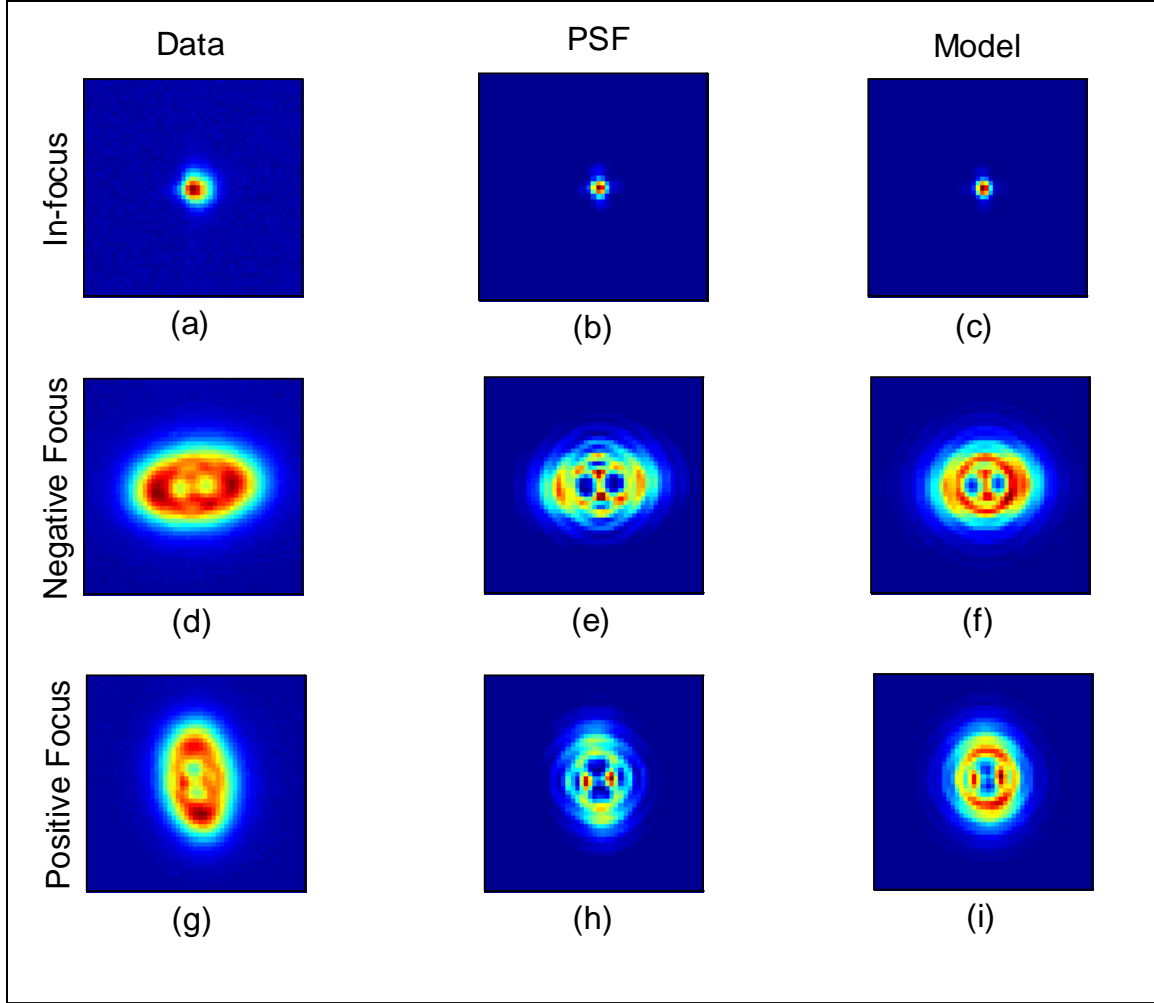


Figure 36. Astigmatism demonstration results.

Table 5 lists the Zernike coefficients (Z_5 - Z_{11}) that are retrieved from the focused PSF shown in Figure 36 (b). The coefficients are used to produce the model displayed as color maps in Figure 36 (c), (f) and (i). Note that the astigmatism term, Z_6 , quantifies the estimated amount of astigmatism generated in the tilted lens demonstration. The in-focus, negative-focus, and positive-focus columns correspond to the position of the CCD relative to focus and the resulting value of the phase retrieved Zernike coefficient for defocus. The theoretical column is computed using the wave optics calculations discussed in the appendix and tilting the lens at an angle of 7.2 deg. As predicted by

theory, tilting the lens generates a measurable amount of astigmatism and the new phase retrieval method is able to quantify that aberration while jointly estimating the other parameters at focus. The small biases of some of the estimated Zernike coefficients from the theoretical values (<0.15 waves) listed in Table 5 are likely due to noise in the data.

Table 5. Astigmatism Demonstration Zernike Coefficient Estimates

Zernike Coefficient	In-Focus	Negative-Focus	Positive-Focus	In-Focus Theory
Z_4	0	-4.6	3.9	0
Z_5	0.15	0.15	0.15	0
Z_6	-0.8	-0.8	-0.8	-0.8
Z_7	-0.05	-0.05	-0.05	0.1
Z_8	-0.1	-0.1	-0.1	0
Z_9	0.05	0.05	0.05	0
Z_{10}	0	0	0	0
Z_{11}	-0.1	-0.1	-0.1	0

5.4 Conclusions

The iterative use of three different phase retrieval techniques: Gerchberg-Saxton, estimated electric field correlation, and intensity LS produces accurate estimates of the magnitude of low order Zernike coefficients of an optical system from focused point source images. Each of these algorithms can estimate the Zernike coefficients alone, but have demonstrated biases that are related to how they are initialized. By using the three methods together, the need to guess the starting wavefront error has not been necessary for the algorithm to accurately estimate the Zernike coefficients. In addition, with this

approach the limitations posed by the wrapped 2-D phase produced by the GS algorithm are avoided. Differences in the electric field pattern and intensity pattern enable the algorithm to escape from local minima/maxima and converge on the correct solution. Simulations and laboratory results demonstrate the performance of the algorithm.

In the future, the new iterative algorithm could potentially be improved. One concept is to use other optical constraints on the GS portion of the algorithm (like in the hybrid input output algorithm) to improve Zernike estimates and decrease convergence time [61]. Another idea is to use a gradient search method (such as the Levine Marquette method) to speed up the LS portion of the algorithm.

The ability to accurately estimate the Zernike coefficients while the optics are near focus should be useful in the alignment of large three mirror telescopes like the SST and LSST because the aberration will not be reintroduced from movements of the secondary and tertiary mirrors required for focusing. Using this phase retrieval method for JWST would simplify their optical design and reduce engineering risk by removing the need for different focal length lenses to generate different defocus values for focus-diverse phase retrieval [45, 47, 48]. In addition, the new phase retrieval algorithm proposed in this chapter has the advantage over NASA's hybrid diversity algorithm (HDA) planned for use on JWST because the HDA uses not only phase diversity but also has to unwrap the pupil phase as its estimates are based on the phase output from GS [47].

VI. Conclusions

Substantial efforts have been made by astronomers to maximize the ability to detect space objects with optical telescopes, but there is a continued need to optimize the process for both military and scientific applications. Improved image processing affords a way to improve space object detection without the need to invest in more costly hardware like space based telescopes or larger aperture ground based telescopes. An evaluation of current image processing techniques was conducted to identify how the SST's image data could be better processed. The two areas uncovered were phase retrieval methods and detection algorithms, which are summarized respectively in Section 2.2 and Section 2.4.

A thorough literature review of existing phase retrieval techniques and detectors available for use on the SST are summarized in Section 2.5. The primary limitation of present phase retrieval techniques is that they require phase diversity that is typically induced by defocusing the telescope as discussed in Section 2.2. Defocusing the telescope is undesirable because of complicated defocusing and alignment procedures of three mirror telescopes. In terms of detection improvement, one possible detection algorithm identified in literature that could be implemented on the SST in place of its baseline point detector is the correlator discussed in Section 2.4. However, previous AFIT research has shown that the correlator suffers from aliasing when the data is undersampled [43].

The image processing techniques that were developed in the pursuit of this research have demonstrated the potential to improve the SST in terms of its system performance metrics described in Section 1.1 including: metric accuracy, photometric

accuracy, and sensitivity. The new phase retrieval techniques that produce low bias estimates of telescope aberrations in terms of Zernike polynomials are illustrated in Figures 18 and 32. Based on the results shown, they could improve the focus and alignment of the SST, which would provide immediate improvement in the telescope's sensitivity by reducing the FWHM of its PSF. Even more noteworthy, the MHT has superior properties that could be used as the kernel of an entirely new image processing scheme that would significantly outperform the baseline algorithm. One of those properties is sub-pixel position information that should improve metric accuracy as described in Section 4.6. Another property of the MHT is the linear relation between its SNR output and estimates of the object's brightness, which has demonstrated improved photometric accuracy over the baseline detector as shown in Figure 27. The most significant improvement in telescope performance accomplished with the MHT over the existing software comes from detection sensitivity gains as illustrated in the GEO eclipse experimental analysis results plotted in Figure 26.

6.1 Long Exposure Phase Retrieval Improvements

Increased understanding of the long exposure phase retrieval problem and better ways to perform it have been developed in this work. One fresh insight is that the presence of a long exposure atmosphere affects the CRLB for Zernike coefficients and that the bound helps predict phase retrieval performance. As shown in Figure 12, the long exposure atmosphere increases the CRLB for Zernike coefficient for defocus. Additionally, Figure 16 shows that the bound predicts the general trend of phase retrieval performance for estimates of the defocus parameter. Another key phase retrieval finding

is that unbiased estimates of Zernike coefficients in the presence of an atmosphere can be made without requiring a defocused spot to generate phase diversity. Chapter III describes a grid search method that can produce unbiased estimates of spherical and defocus coefficients in the presence of a long exposure atmosphere as seen in Figure 18.

In the long exposure atmospheric case, the limitations of differentiating between the contribution of telescope aberrations and atmospheric blurring to the intensity pattern are overcome by jointly estimating the atmospheric seeing parameter and Zernike coefficients using Eq. (3.38). The method works because it uses a grid search method to select from a library of possible PSFs to find the PSF that best matches the measured intensity pattern. The selected PSF corresponds to specific Zernike coefficients and seeing parameter values. This method is useful when there are a small number of coefficients that need to be estimated. This is the case for the SST because Z_5 - Z_{11} were previously estimated using a phase diversity technique and only r_0 and Z_4 need to be estimated near focus in order to build the PSF model used in the MHT (see Section 4.4).

6.2 Telescope Detection Improvements

The implementation of a MHT by the SST will increase its probability of detecting space objects over the baseline detector through three improvements: using multiple pixels to compute SNR, mitigating aliasing effects, and computing more accurate window statistics. The MHT mitigates the combined effects of atmospheric blurring and telescope aberrations that cause point source light to spread across multiple pixels. This is done by including the PSF in the MHT through Eq. (4.13), which computes higher SNR values than the baseline detector because the point detector only

uses one pixel to compute SNR through Eq. (2.32). In addition, since the SST's data is undersampled, the measured PSF changes shape when the light is not centered on a pixel and the MHT is able to mitigate the aliasing effects that degrade the performance of both the correlator and the baseline detector. This is accomplished by shifting position on the Nyquist grid as discussed in Section 4.4. In addition, the computation of the noise statistics in the window surrounding the pixel being tested is skewed by stars crossing, cosmic radiation and bad pixels. However, by removing outlier pixel data, more accurate standard deviations are computed and used in the MHT as discussed in Section 4.5. By combining these improvements into the MHT through Eq. (4.13) and Eq. (4.18), the MHT demonstrates improvement in P_d of over 50% over the baseline detector based on the data collected in the ANIK-F1 GEO eclipse experiment as shown in Figure 26.

6.3 Short Exposure Phase Retrieval Improvements

In future the SST sites, Zernike coefficients may not be estimable with the currently used phase diversity techniques due to poor atmospheric seeing condition or because defocusing the telescope may be undesirable. Unfortunately, the long exposure phase retrieval method is too computationally burdensome for estimating large numbers of Zernike coefficients. However, if the SST upgrades to a frame transfer camera, the phase retrieval algorithm described in chapter V can produce unbiased estimates of Zernike coefficients (Z_4 - Z_{11}) in the presence of the short exposure atmosphere as shown in Figure 32.

The primary improvement of the short exposure phase retrieval for Zernike coefficients over existing methods is that it does not require defocusing of the telescope

in order to estimate coefficients thus making it a useful new tool for optical diagnostics. The short exposure phase retrieval of Zernike coefficients from a focused telescope point source intensity pattern using only an intensity based least squares direct search approach is challenging because of the correlation between intensity patterns produced by different aberrations as illustrated in Figures 29 (a) and (c). In contrast, the electric field patterns produced by the same aberrations are much less correlated as shown in Figures 29 (b) and (d). Therefore, by using an estimated electric field in conjunction with the intensity pattern, the new short exposure phase retrieval algorithm is able to produce nearly unbiased estimates of the Zernike coefficients from both simulated and experimental data as discussed in Sections 5.2-5.3.

6.4 Future Work

While significant strides have been made to enhance the performance of the SST and other astronomical telescopes, many other interesting and relevant questions that could be answered in future research have been uncovered including: Is it better to use the long or short exposure atmospheric model for phase retrieval of Zernike coefficients? How does the MHT perform as a function of atmospheric seeing? How often should phase retrieval be conducted to mitigate seeing effects on the detection performance of the MHT? How much degradation in MHT performance results from the changes in PSF shape? What is the range of PSF shapes that can be tolerated? How much does the performance of the correlation based BHT depend on the PSF shape? How is the performance of the MHT affected by variations in the PSF across the FOV? Will multiple PSF shapes be used for different positions on the field? If not, what is the

degradation in performance if a single PSF is used for the field? By addressing these questions even better detection performance may be achieved with SST.

6.5 Final Observations

Investigating how to improve image processing for space object detection has been a fruitful area of research and a productive means of enhancing ground based telescope performance. While better ways for phase retrieval and detection have been identified in this dissertation, it has also opened up an entire new area for future research as outlined with the questions in the previous section. Continued pursuit to answer these questions and the new ones that are certain to arise should be productive both from academic and DoD points of view. This is because further enhancement to image processing of the SST and other telescopes contributing to the space surveillance network has the potential to enhance the United States' SSA capabilities.

VII. Appendices

The following three sections provide additional supporting evidence for the validity of the phase retrieval performance described in Chapters III and IV. The first two sections provide empirical evidence that the SST star data used for phase retrieval is modeled with an appropriate cumulative distribution function (CDF) and that the pixels can be considered statistically independent. The last section covers the method by which the theoretical Zernike coefficients for the aberrations produced in the lens experiment described in Chapter IV were computed.

A.1 The SST's CCD Noise Statistics

Raw measurements of digital counts were recorded from a star observed with the SST over multiple frames. An empirical quantile-quantile (Q-Q) plot of the data from the pixel the star was centered on versus a Poisson probability mass function (PMF) with the same mean as the star intensity is shown in Figure 37 (a) [62]. By inspecting the plot it appears that the Poisson PMF is not an ideal match for the data because an excellent fit would have the blue data marker on the red line formed by the ideal distribution. One possibility for the disparity between the data distribution and the Poisson PMF is that the data is quantized.

Quantization noise occurs in the analog-to-digital conversion process from photons received to digital counts if it is not a one-to-one conversion. The gain, G , that converts between the total number photons received in a pixel and expected digital count is represented by

$$E[d(m)] = G \left[\sum_x \theta_1 h(m-x) + B \right], \quad (7.1)$$

where, $E[d(m)]$ is the mean number of digital counts in the pixel of interest, m ; θ_1 is the intensity of the space object, x is the pixel coordinates in the window of interest; $h(m-x)$ is the PSF and B is the background. The mean number of photons incident on a pixel

$$E[d'(m)] = \sum_x \theta_1 h(m-x) + B. \quad (7.2)$$

Since gain is a constant, the relation between the digital counts and the photon incident on a pixel, $d'(m)$, is

$$d(m) = G d'(m). \quad (7.3)$$

Shot noise is caused by the fact the independent photon arrival times on the CCD for each pixel in the image can be considered a collection of Poisson random variables (RV), therefore $d'(m)$ has a Poisson PMF [2]. If quantization noise and shot noise are the dominate noises in $d(m)$, then $d(m)/G$ will also have a closer match to Poisson statistics.

To characterize the CCD and determine G from the imagery data, the following derivation is used. For a given pixel the mean number of digital counts is

$$\bar{d} = E[d(m)] = G E[d'(m)], \quad (7.4)$$

and the second moment is

$$\begin{aligned}
E\left[\left(d(m) - \bar{d}\right)^2\right] &= E\left[d^2(m) - 2d(m)\bar{d} + \bar{d}^2\right] \\
&= E\left[d^2(m)\right] - 2\bar{d}^2 + \bar{d}^2 \\
&= E\left[d^2(m)\right] - \bar{d}^2(m).
\end{aligned} \tag{7.5}$$

In addition,

$$E\left[d^2(m)\right] = E\left[\left(Gd'(m)\right)^2\right] = G^2 E\left[d'^2(m)\right]. \tag{7.6}$$

Substituting Eq. (7.6) and Eq. (7.4) into Eq. (7.5)

$$\begin{aligned}
E\left[d^2(m)\right] - \bar{d}^2 &= G^2 E\left[d'^2(m)\right] - G^2 E^2\left[d'(m)\right] \\
&= G^2 \left\{ E\left[d'^2(m)\right] - E^2\left[d'(m)\right] \right\} \\
&= G^2 E\left[d'(m)\right].
\end{aligned} \tag{7.7}$$

because for a Poisson random variable (RV) the mean is equal to the variance.

Therefore, G can be estimated from the data by dividing Eq. (7.7) by Eq. (7.4)

$$\frac{E\left[d^2(m)\right] - \bar{d}^2}{E\left[d(m)\right]} = \frac{G^2 E\left[d'(m)\right]}{GE\left[d'(m)\right]} = G. \tag{7.8}$$

Using star data from the SST the gain was estimated to be $G = 3$.

The gain estimate was used to remove the quantization effect from the raw data shown in Figure 37 (a) to produce the adjusted Q-Q plot in Figure 37 (b). The plot shows that the data with quantization noise removed is better modeled with the Poisson PMF, because the magnitude of the offsets of the blue data points from the ideal distribution indicated by the red line are significantly reduced. This analysis provides a measure of confidence that the Poisson PMF should be used for the derivation of the LRT detectors and CRLB for estimates of Zernike polynomial coefficients.

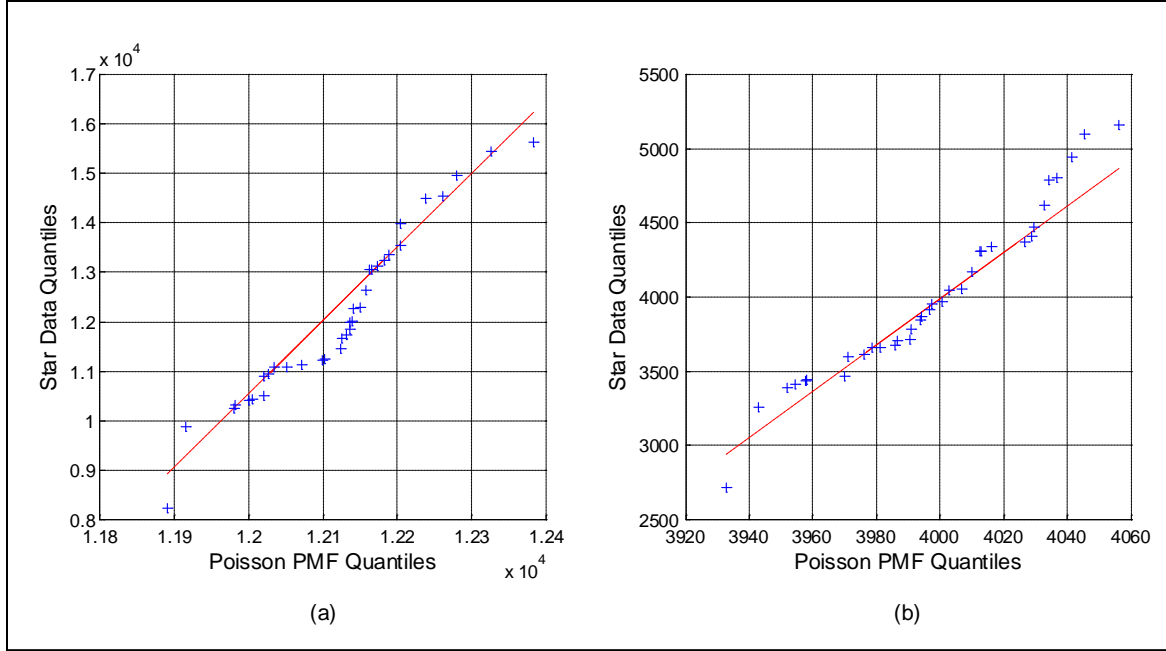


Figure 37. Q-Q Plot of star data from the SST images versus a Poisson distribution (a) raw data (b) Corrected for quantization

A.2 The SST's CCD Pixel Independence

The same star data used to characterize the SST's CCD noise statistics is used to evaluate the independence of the data in each pixel. The Spearman coefficient of rank correlation, ρ , was used to find the correlation between the pixel that the star was centered on and the adjacent pixels as shown in Figure 38 [62]. For the pixels evaluated, ρ was much closer to 0 than to 1 or -1 indicating that the pixels are independent. Furthermore, the p-value is larger than 0.1 in all four cases indicating that the correlation is significantly different from 1.

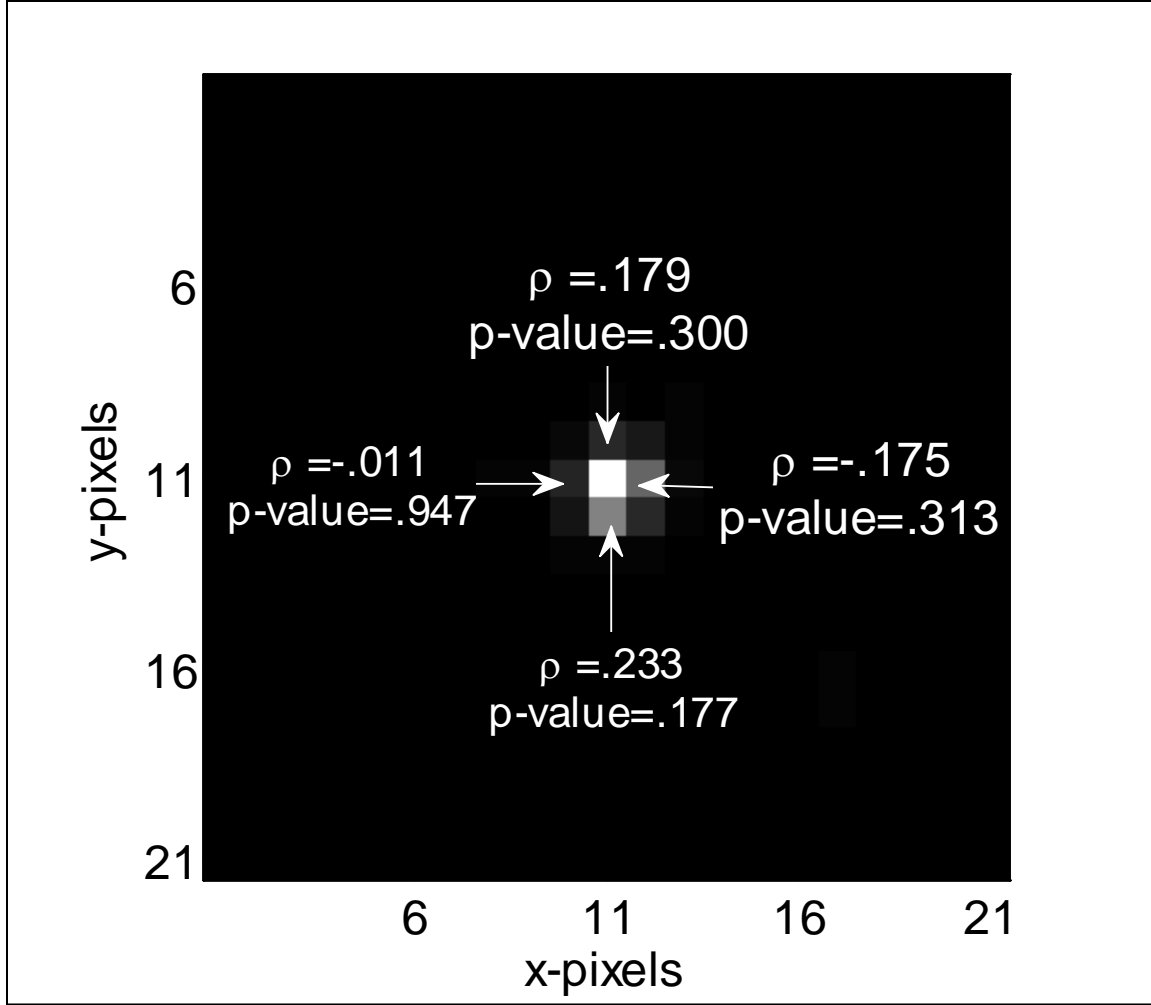


Figure 38. Correlation between a star's center pixel and adjacent pixels

A.3 Aberration Calculations for a Single Lens

The aberrations produced by a single lens are calculated using a wave optics approach to verify the accuracy of the phase retrieval results in the laboratory demonstrations presented in this paper. The point source is assumed to generate a spherical wavefront that is propagated to the lens. The lens introduces a quadratic phase transformation and then the spherical wavefront is propagated to the image plane [31]. The combined wavefront error from the two propagations and the lens transformation are

summed up in the pupil and then decomposed into scaled Zernike polynomials to determine the theoretical Zernike coefficients.

The wave optics simulation input values are the object and image plane distances from the lens, S_I and S_O , the focal length of the lens, f , the wavelength of light, λ , and the diameter of the entrance pupil, D . Then the magnification by the lens, M , is computed as [30]

$$M = -\frac{S_I}{S_O}. \quad (7.9)$$

Two variables are used, one is the amount of displacement the object from the optic axis, Δy , and the other the distance the camera is from image plane, Δz .

The wave optics simulation begins with the generation of a 1024 by 1024 phase screen, such that the pixel size in the pupil, dx , is

$$dx = \frac{D}{1024}. \quad (7.10)$$

Two 1024 by 1024 matrices of the x and y coordinates are generated, \underline{x} and \underline{y} , and are set such that the center pixel in the grid has coordinate (0,0) and have the pupil spacing of dx . With the phase screens set up, the object is modeled as a spherical wave, \underline{W}_1 , propagated from the object plane to the lens using the following distance formula [3]

$$\underline{W}_1 = 2 \cdot \pi \cdot \left(\left(\underline{y} - \Delta y \right)^2 + S_O^2 \right)^{\frac{1}{2}} / \lambda. \quad (7.11)$$

To compute the lens transformation, the radius of the pupil, \underline{r} , is computed as a function of pixel coordinates

$$\underline{r} = \left(\underline{x}^2 + \underline{y}^2 \right)^{\frac{1}{2}}, \quad (7.12)$$

and the quadratic phase factor for the lens, $\underline{\underline{\Lambda}}$, is computed as

$$\underline{\underline{\Lambda}} = \frac{-\pi \cdot \underline{\underline{r}}^2}{\lambda \cdot f}. \quad (7.13)$$

Next the wavefront error caused by propagation from the lens to image location in image plane, $\underline{\underline{W}}_2$, is computed using the distance formula

$$\underline{\underline{W}}_2 = 2 \cdot \pi \cdot \left(\left(\underline{\underline{y}} - M \cdot \Delta y \right)^2 + \left(S_I - \Delta z \right)^2 \right)^{1/2} / \lambda. \quad (7.14)$$

The total wavefront in the pupil, $\underline{\underline{W}}_T$, is the linear combination of the wavefront error from each of the propagations and the lens transformation

$$\underline{\underline{W}}_T = \underline{\underline{W}}_1 + \underline{\underline{\Lambda}} + \underline{\underline{W}}_2. \quad (7.15)$$

Finally, the total wavefront is decomposed to determine the each of the Zernike coefficients, $\underline{\underline{Z}}_i$, the using the orthogonality of the each Zernike polynomials, $\underline{\underline{\phi}}_i$, such that

$$\underline{\underline{Z}}_i = \sum \sum \left(\underline{\underline{\phi}}_i \cdot \underline{\underline{W}}_T \right). \quad (7.16)$$

Bibliography

- [1] T. Blake, "DARPA Web Site," Tactical Technology Office, 26 Jun 2013. [Online]. Available: [http://www.darpa.mil/Our_Work/TTO/Programs/Space_Surveillance_Telescope_\(SST\).aspx](http://www.darpa.mil/Our_Work/TTO/Programs/Space_Surveillance_Telescope_(SST).aspx). [Accessed 26 Jun 2013].
- [2] BAE Systems, "Unique search and track procedures utilizing the Ground-based Electro-Optical Deep Space Surveillance (GEODSS) worldwide sites," in Advanced Maui Optical and Space Surveillance Technologies Conference, Maui, 2012.
- [3] D. Monet, T. Axelrod, C. Claver, T. Blake, R. Lupton, E. Pearce, R. Shaw and D. Woods, "Rapid Cadence Collections with the Space Surveillance Telescope," in AMOS, Maui, 2012.
- [4] Office of the President of the United States of America, "NATIONAL SPACE POLICY of the UNITED STATES of AMERICA," United States Government, Washington DC, 2010.
- [5] R. Sridharan and A. F. Pensa, "U.S. Space Surveillance Network capabilities," in Proc. SPIE 3434, Image Intensifiers and Applications; and Characteristics and Consequences of Space Debris and Near-Earth Objects, San Diego, 1998.
- [6] M. M. Morton and T. Roberts, "Joint Space Operations Center (JSpOC) Mission System (JMS)," in Advanced Maui Optical and Space Surveillance Technologies Conference, Maui, 2011.
- [7] R. F. Colarco, "Space Surveillance Network Sensor Development, Modification, and Sustainment," in Advance Maui Optical and Space Surveillance Technologies Conference, Maui, 2009.
- [8] United Nations Committee on the Peaceful uses of Outer Space, "Technical Report on Space Debris," United Nations, New York, 1999.
- [9] U. S. 1. Congress, "Public Law 109–155," United States Government, 2005.
- [10] National Aeronautics and Space Administration, "NEO Discovery Statistics," [Online]. Available: <http://neo.jpl.nasa.gov/stats/>. [Accessed 26 July 2011].
- [11] R. Grant, "Vulnerability in Space," Air Force Magazine, vol. 91, no. 6, 2008.
- [12] E. Stansbery, "Orbital Debris Program Office," NASA, 02 October 2012. [Online]. Available: <http://orbitaldebris.jsc.nasa.gov/photogallery/beehives.html#geo>. [Accessed 26 June 2013].
- [13] R. V. Willstrop, "The Mersenne--Schmidt: a three-mirror survey telescope," Royal Astronomical Society, vol. 210, pp. 597-609, 1984.
- [14] G. Stokes, Interviewee, Requirements Trace for the SST. [Interview]. 12 Sept 2012.

- [15] DARPA, "Space Surveillance Telescope (SST) Phase I System Test Procedures," US Government, Washington DC, 2011.
- [16] S. Maksim, J. Zingarelli and S. Cain, "A Comparison Between a Non-linear, Poisson-based Statistical Detector and a Linear, Gaussian Statistical Detector for Detecting Dim Satellites," in Advanced Maui Optical and Space Surveillance Technologies Conference, Maui, 2012.
- [17] D. Woods, "The Space Surveillance Telescope: Focus and Alignment of a Three Mirror Telescope," in Advanced Maui Optical and Space Surveillance Technologies Conference, Maui, 2012.
- [18] J. C. Zingarelli, T. Blake and S. Cain, "Improving Ground Based Telescope Focus through Joint Parameter Estimation," in Advanced Maui Optical and Space Surveillance Technologies Conference, Maui, 2012.
- [19] T. J. Schulz, W. Sun and M. C. Roggemann, "Cramer-Rao Bounds for estimation of turbulence-induced wavefront aberrations," in SPIE Conference on Propagation and Imaging through Atmosphere III, Denver, 1999.
- [20] J. W. Goodman, Statistical Optics, New York: Wiley Interscience, 1985.
- [21] LSST Corporation, "Large Synoptic Survey Telescope," 04 06 2011. [Online]. Available: <http://www.lsst.org/files/docs/overviewV2.0.pdf>. [Accessed 03 06 2013].
- [22] G. Molesoni, "Galileo's telescope and the birth of instrumental optics: a review note," Applied Optics, vol. 49, no. 16, pp. D1-D5, 2010.
- [23] N. Miura and K. Itagaki, "Likelihood-base Method for Detecting Faint Moving Objects," The Astronomical Journal, pp. 1278-1285, 2005.
- [24] P. S. Gural, J. A. Larsen and A. E. Gleason, "Matched Filter Processing for Asteroid Detection," The Astronomical Journal, pp. 1951-1960, 2005.
- [25] H. Viggh, G. Stokes, F. Shelly, M. Blythe and J. Stuart, "Applying Electro-Optical Space Surveillance Technology to Asteroid Search and Detection: The Linear Program Results," in Proceedings of the 1998 Space Control Conference, Lexington, 1998.
- [26] E. C. Pearce, F. Shelly and J. A. Johnson, "High Precision Real Time Processing for the MOSS and LINEAR Systems," in Space Control Conference, Boston , 2003.
- [27] N. A. Roddier, "Atmospheric wavefront simulation using Zernike polynomials," Optical Engineering, vol. 29, no. 10, pp. 1174-1180, 1990.
- [28] M. C. Roggemann, Imaging Through Turbulence, CRC Press, 1996.
- [29] R. Noll, "Zernike polynomials and atmospheric turbulence," J. Opt. Soc. Am., vol. 66, pp. 207-211, 1976, Oct..

- [30] E. Hecht, Optics, Addison Wesley, 1997.
- [31] J. W. Goodman, Fourier Optics, Greenwood Village, CO: Roberts & Company, 2005.
- [32] J. Fienup, J. Marron, T. Schulz and J. and Seldin, "Hubble Space Telescope characterized by using phase-retrieval algorithms," Applied Optics, vol. 32, no. 10, p. 1747-1767, 1993.
- [33] F. Roddier, "Curvature sensing and compensation: a new concept in adaptive optics," APPLIED OPTICS, vol. 27, no. 7, pp. 1223-1225, 1988.
- [34] R. W. Gerchberg and W. O. Saxton, "A Practical Algorithm for the Determination of Phase from Image and Diffraction Plane Pictures," OPTIK, vol. 35, no. 2, pp. 237-246, 1972.
- [35] J. E. Krist and C. J. Burrows, "Phase-retrieval analysis of pre- and post-repair Hubble Space Telescope images," APPLIED OPTICS, vol. 34, no. 22, pp. 4951-4964, 1995.
- [36] D. C. Ghiglia and M. D. Pritt, Two-dimensional phase unwrapping theory, algorithms and software, Hoboken: Wiley-Interscience, 1998.
- [37] C. J. Pellizzari and J. D. Schmidt, "Phase unwrapping in the presence of strong turbulence," in Aerospace Conference, 2010 IEEE, Big Sky, 2010.
- [38] S. M. Kay, Fundamentals of Statistical Signal Processing, Upper Saddle River, NJ: Prentice-Hall, 2011.
- [39] P. Hickson, "Wave-front curvature sensing from a single defocused image," Journal of the Optical Society of America, vol. 11, no. 5, pp. 1667-1673, 1994.
- [40] I. Putnam and S. Cain, "Modeling a Temporally Evolving Atmosphere with Zernike Polynomials," in Advanced Maui Optical and Space Surveillance Technologies Conference, Maui, 2012.
- [41] "Pan-Starrs," 2005. [Online]. Available: <http://pan-starrs.ifa.hawaii.edu/public/>. [Accessed 02 03 2011].
- [42] S. C. Pohlig, "An Algorithm for Detection of Moving Optical Targets," IEEE Transactions on Aerospace and Electronic Systems, vol. 25, no. 1, pp. 56-63, 1989.
- [43] A. O'Dell and S. Cain, "Investigating the Effects of Atmospheric Seeing on the Detection of near Earth Orbiting Asteroids," in IEEE Aerospace Conference, 2009.
- [44] K. P. Thompson, S. Tobias and J. P. Rolland, "The misalignment induced aberrations of TMA telescopes," Optics Express, vol. 16, no. 25, pp. 20345-20353, 2008.
- [45] B. Dean, "Hybrid diversity method utilizing adaptive diversity function". US Patent 20080040077 A1, 14 Feb 2008.
- [46] National Air and Space Administration, "James Webb Space Telescope," National Air and Space Administration, 12 08 2013. [Online]. Available:

- <http://www.jwst.nasa.gov/index.html>. [Accessed 13 08 2013].
- [47] Space Telescope Institute, "James Webb Space Telescope Wavefront Sensing and Control," Space Telescope Institute, [Online]. Available: <http://www.stsci.edu/jwst/ote/wavefront-sensing-and-control>.
 - [48] D. Scott Acton, J. Scott Knight, A. Contos, S. Grimaldi, J. Terry, P. Lightsey and A. Barto, "Wavefront Sensing and Controls for the James Webb Space Telescope," in Proceedings of SPIE, Amsterdam, 2012.
 - [49] M. Vollmer and S. D. Gedzelman, "Simulating irradiance during lunar eclipse: the spherically symmetric case," Applied Optics, vol. 47, pp. 52-61, 2008.
 - [50] F. J. Verba and e. al, "A Survey of Geosynchronous Satellite Glints," DTIC, Flagstaff, 2009.
 - [51] J. Anderson and I. R. King, Space Telescope Science Institute, NASA, 2006.
 - [52] R. Schödel, "Accurate photometry with adaptive optics in the presence of anisoplanatic effects with a sparsely sampled PSF," Astronomy & Astrophysics, pp. 1-16, 2010.
 - [53] S. T. Thurman and J. R. Fienup, "Complex pupil retrieval with undersampled data," Journal Optical Society of America, pp. 2640-2647, 2009.
 - [54] L. Pinheiro da Silva, M. Auvergne, D. Toubanc, J. Rowe, R. Kuschnig and J. Matthews, "Estimation of a super-resolved PSF for the data reduction of undersampled stellar observations," Astronomy & Astrophysics, pp. 363-369, 2006.
 - [55] T. R. Lauer, "Combining Undersampled Dithered Images," Astronomical Society of the Pacific, pp. 227-237, 1999.
 - [56] M. Kutner, C. Nachtsheim, J. Neter and W. Li, Applied Linear Statistical Models, 2005.
 - [57] T. J. Schulz, "Multiframe blind deconvolution of astronomical images," J. Optical Society of America, vol. 10, no. 5, pp. 1064-1073, 1993.
 - [58] L. Shepp and Y. Vardi, "Maximum Likelihood Reconstruction for Emission Tomography," IEEE Transactions on Medical Imaging, Vol. 1, no. 2, pp. 113-122, 1982.
 - [59] A. Tokovinin and S. Heathcote, "Donut: Measuring Optical Aberrations from a Single Extrafocal Image," The Astronomical Society of the Pacific, vol. 118, no. 846, pp. 1165-1175, 2006.
 - [60] T. G. Kolda, R. M. Lewis and V. Torczon, "Optimization by Direct Search: New Perspectives on Some Classical and Modern Methods," Society for Industrial and Applied Mathematics, vol. 45, no. 3, pp. 385-482, 2003.

- [61] J. R. Fienup, "Phase retrieval algorithms: a personal tour [Invited]," *Applied Optics*, vol. 52, no. 1, pp. 45-56, 2013.
- [62] P. H. Kvam and B. Vidakovis, *Nonparametric Statistics with Applications to Science and Engineering*, Hoboken: John Wiley & Sons, Inc, 2007.

REPORT DOCUMENTATION PAGE			<i>Form Approved</i> <i>OMB No. 0704-0188</i>	
<p>The public reporting burden for this collection of information is estimated to average 1 hour per response, including the time for reviewing instructions, searching existing data sources, gathering and maintaining the data needed, and completing and reviewing the collection of information. Send comments regarding this burden estimate or any other aspect of this collection of information, including suggestions for reducing this burden to Department of Defense, Washington Headquarters Services, Directorate for Information Operations and Reports (0704-0188), 1215 Jefferson Davis Highway, Suite 1204, Arlington, VA 22202-4302. Respondents should be aware that notwithstanding any other provision of law, no person shall be subject to any penalty for failing to comply with a collection of information if it does not display a currently valid OMB control number. PLEASE DO NOT RETURN YOUR FORM TO THE ABOVE ADDRESS.</p>				
1. REPORT DATE (DD-MM-YYYY) 13-Nov-2013		2. REPORT TYPE Dissertation		3. DATES COVERED (From — To) Sep 2011 – Dec 2013
4. TITLE AND SUBTITLE ENHANCING GROUND BASED TELESCOPE PERFORMANCE WITH IMAGE PROCESSING			5a. CONTRACT NUMBER	
			5b. GRANT NUMBER	
			5c. PROGRAM ELEMENT NUMBER	
6. AUTHOR(S) Zingarelli, John C., Major, USAF			5d. PROJECT NUMBER	
			5e. TASK NUMBER	
			5f. WORK UNIT NUMBER	
7. PERFORMING ORGANIZATION NAME(S) AND ADDRESS(ES) Air Force Institute of Technology Graduate School of Engineering and Management (AFIT/ENY) 2950 Hobson Way WPAFB OH 45433-7765			8. PERFORMING ORGANIZATION REPORT NUMBER	
9. SPONSORING / MONITORING AGENCY NAME(S) AND ADDRESS(ES) Defense Advance Project Research Agency			10. SPONSOR/MONITOR'S ACRONYM(S) DARPA	
			11. SPONSOR/MONITOR'S REPORT NUMBER(S)	
12. DISTRIBUTION / AVAILABILITY STATEMENT APPROVED FOR PUBLIC RELEASE; DISTRIBUTION UNLIMITED				
13. SUPPLEMENTARY NOTES This material is declared a work of the U.S. Government and is not subject to copyright protection in the United States.				
14. ABSTRACT The Space Surveillance Telescope (SST) is a Defense Advanced Research Projects Agency (DARPA) program designed to detect objects in space like Near Earth Asteroids (NEAs) and space debris in the Geosynchronous Earth Orbit (GEO) belt. Binary hypothesis tests (BHTs) have historically been used to facilitate the detection of new objects in space. In this dissertation, a multi-hypothesis test (MHT) detection strategy is introduced to improve the detection performance of the SST. In this context, the MHT determines if an unresolvable point source is in the center, corner or side of a pixel in contrast to a BHT, which only tests whether an object is in the pixel or not. An experiment, recording observations of a known GEO satellite as it enters eclipse, is used to demonstrate improved probability of detection with the MHT by as much as 50% over existing BHT methods. In order to achieve optimal performance of the SST, alignment of the telescope is conducted by retrieving phase information from defocused point sources to determine the telescope's aberrations and then the mirrors are moved for optical correction. A new direct search phase retrieval technique for determining the optical prescription of an imaging system in terms of Zernike coefficients is described. The technique provides coefficient estimates without the need to defocus point source images to generate phase diversity by using electric field estimates in addition to intensity data. Simulated point source data shows the new phase retrieval algorithm avoids getting trapped in local minima over a wide range of random aberrations. Experimental point source data are used to demonstrate the phase retrieval effectiveness.				
15. SUBJECT TERMS Atmospheric effects — Methods: data analysis — Methods: statistical — Methods: numerical — Techniques: image processing				
16. SECURITY CLASSIFICATION OF:			17. LIMITATION OF ABSTRACT	18. NUMBER OF PAGES
a. REPORT	b. ABSTRACT	c. THIS PAGE	UU	142
U	U	U		
			19a. NAME OF RESPONSIBLE PERSON Dr. Stephen Cain	
			19b. TELEPHONE NUMBER (Include Area Code) (937)255-3636, ext 4716 stephen.cain@afit.edu	

Standard Form 298 (Rev. 8-98)
Prescribed by ANSI Std. Z39.18